Development of Compact UWB Transmit Receive Modules and Filters on Liquid Crystal Polymer for Radar

By

Calen Carabajal

Submitted to the graduate degree program in Department of Electrical Engineering and Computer Science and the Graduate Faculty of the University of Kansas in partial fulfillment of the requirements for the degree of Master of Science.

Dr. Carl Leuschen, Chair

Dr. Fernando Rodriguez-Morales, Co-chair

Dr. Christopher Allen

Date Defended: 8 October 2020

The Thesis Committee for Calen Carabajal certifies that this is the
approved version of the following thesis:

Development of Compact UWB Transmit Receive Modules and Filters on Liquid Crystal Polymer for Radar

Dr. Carl Leuschen, Chair

Date Approved: 23 November 2020

Abstract

This thesis presents the design and development of various microwave components for an airborne snow-probing radar with multi-gigahertz bandwidth and cm-scale vertical resolution.

First, a set of ultra-wideband, modular transmit and receive modules with custom power sequencing circuits is presented. These modules were rapid-prototyped as an initial step toward the miniaturization of the radar's front-end, using a combination of custom and COTS circuits. The transmitter and receiver modules operate in the 2–18 GHz range. Laboratory and field tests are discussed, demonstrating performance that is comparable to previous, connectorized implementations, while accomplishing a 5:1 size reduction.

Next, a set of miniaturized band-pass and low-pass filters is developed and demonstrated. This work addressed the lack of COTS circuits with adequate performance in a sufficiently small form factor that is compatible with the planar integration required in a multi-chip module.

The filters presented here were designed for manufacture on a multi-layer liquid crystal polymer (LCP) substrate. A detailed trade study to assess the effects of potential manufacturing tolerances is presented. A framework for the automated creation of panelized design variations was developed using CAD tools. Thirty-two design variations with two different types of launches (microstrip and grounded co-planar waveguide) were successfully simulated, fabricated and tested, showing good electrical performance both as individual filters and cascaded to offer outstanding out-of-band rejection. The size of the new filters is 1 cm x 1 cm x 150 µm, a vertical reduction of over 90% and reducing the total cascaded length by over 50%.

Acknowledgments

This work was funded by the Department of Energy's Kansas City National Security Campus, operated by Honeywell Federal Manufacturing and Technologies, LLC, under contract number DE-NA0002839.

Dr. Fernando Rodriguez-Morales has been my advisor since I first joined CReSIS in 2013 and later rejoined in 2017, and his advice, support, and wisdom have been of untold importance in my development as a student of science and an engineer, for which I cannot express my gratitude enough. I would like to thank both him and Dr. Carl Leuschen for opportunity to work on this project and others throughout my time at the Center.

Thank you to Dr. James Stiles and Dr. Christopher Allen for providing me a strong knowledge of high-speed electronics, RF engineering, and radar systems through their courses.

Thank you to Dr. Daniel Gomez-Garcia, Dr. Jay McDaniel, and Bryan Townley for answering questions and talking through design problems. Thank you to the CReSIS staff for maintaining a great research center, especially Paulette Place for her diligence in teaching others, Aaron Paden for his rapid work in the machining lab, and Jennifer Laverentz for prioritizing students' administrative problems and questions, especially in complicated situations.

Thank you to Dr. Ambrose Wolf for his leadership in the consortium during this uncertain period. Thank you to Tim Carlson and Dr. Yongfeng Lu at UNL for laser routing, and Dr. John Papapolymerou and Brian Wright at MSU for their concurrent fabrication work on the LCP filters.

I would like to thank my parents, Jim and Lee Carabajal, for their unceasing support.

Finally, I would like to dedicate this thesis research to my wife, Mary Krape, whose loving patience and ability to make me laugh are wholly unmatched.

Table of Contents

List of Figures

List of Tables

1: Introduction

1.1 Scientific Motivation and Background

Microwave and mm-wave radars have been used extensively for remote sensing applications, including the monitoring of snow cover thickness on sea ice [1], snow/firn stratigraphy studies on ice sheets [2] [3] and land [4], profiling of lake ice [5], asphalt measurements [6], agricultural monitoring [7], and others. Ultra-wideband (UWB) microwave radars are especially useful in remote sensing applications, as their broad bandwidth allows for resolving narrowly-spaced targets or media interface levels, giving them particular utility in geophysical research and measurements of snow cover in the Arctic and Antarctic [8].

Although microwave radars for geophysical research have been in use since the 1960s [9], systems optimized for snow research have been continuously developed with incremental improvements to present day [10]. Researchers at the University of Kansas have played a key role in these development efforts, including a 2-8 GHz FMCW for snow cover thickness measurements. [11]. The initial proof-of-function demonstrations of this radar, referred to as the “Snow Radar”, in the early 2000s were largely successful[12-15], but early implementations had limitations in the generation of ultra-linear, fast chirp signals with repetition frequencies compatible with airborne operation [16].

By levering advances in solid-state devices and circuits, this initial system was eventually improved to function from low-altitude (<5,000 ft above ground level) aircraft, providing sufficient frequency linearity to support operation with bandwidths ranging from 2 GHz to 4.5 GHz [1]. This version of the snow radar relied on down-converting a Ku-band Chirp signal with sub-millisecond duration and 2-kHz PRF to produce its transmitted waveform. The Ku-band chirp generator was the basis of a separate system for altimetry measurements on ice sheets and sea ice [17]. Subsequent improvements to the linearity of the chirp generator resulted in operation over the full 2-8 and 12-18 GHz bandwidths[8,18,19].

These systems operated successfully from 2009-2015 [8], providing large amounts of valuable data for the snow and ice science community[20-22]. However, they had vertical resolution limitations in areas where snow cover is thinner than ~8 cm[21-23]. Accurate mapping of snow cover is vital, as snow covers as much as 9% of the Earth's surface and directly affects melt rates of the ice cover and circulation of ocean water, ultimately impacting global weather patterns [8]. Snow cover on sea ice causes undesired biases in estimates of sea ice thickness and freeboard measurements in data taken by satellite due to the their relatively narrow-band operation [24].

In 2015-2016, the 2-8 GHz and 12-18 GHz radars were combined into a single system operating across a 2-18 GHz bandwidth[1], thereby providing sub-inch vertical resolution while offering additional data across X band. Initial field tests of the UWB 2-18 GHz Snow Radar were completed onboard a Twin Otter [25-27] and Basler aircraft [28], and more recently as a proof-of-concept for agricultural monitoring [7] and soil moisture measurements from short and medium range [29]. These led to the most recent development of a dual-mode microwave system for very long range measurements, which was first deployed in 2017 [30]. This newest system is capable of operating in the conventional FMCW mode with 2-18 GHz bandwidth to altitudes up to 3,600 ft AGL and is also capable of operating as a 2-14 GHz heterodyne FMCW radar. In this system, the 240-µs transmission pulse duration was reduced to 200 µs, time-delaying the local oscillator

---

[1] This system is generally referred to as the "UWB Snow Radar".

(LO) signal to retain the desired intermediate frequency. This heterodyne time-delayed stretch processing mode permitted the measurement of snow thickness at high altitudes and was tested over sea ice during a NASA Operation IceBridge mission transit flight from the United States to Northern Greenland, at a nominal flight altitude of ~19,000 ft AGL. As such, the Snow Radar became the first to take wide-area snow thickness measurements above 1.5 km AGL with cm-scale vertical resolution.

The Snow Radar's development has therefore been long, with numerous design iterations and updates. With the increased availability of unmanned aerial vehicles and systems (UAS), CubeSat platforms, and expanded application of microwave radars into other realms that require more portability, it became highly desirable to integrate the system into a much smaller form factor while retaining its outstanding electrical performance. Initial demonstrations by other groups show the advantages of miniaturized systems in the context of snow studies and other applications[31-35]. The radio frequency (RF) front end of the Snow Radar has been reduced from fully-connectorized systems to singular, compact modules, already providing a major reduction in size [36].

Due to its ultra-wide bandwidth, proven cm-scale range resolution, and varied application potential, the system is well-suited as a test bed for advancing packaging technologies and component development for radar. The RF front-end subsystem – the transmitter (Tx) and receiver (Rx) – are investigated for transitioning into multi-chip modules (MCMs), reducing the once-connectorized and now-compact system further. Two major bottlenecks for full RF miniaturization are present: first, the lack of availability of small bandpass filters compatible with tightly integrated MCMs; second, the need for a fully integrated digital back end. The latter of these bottlenecks started being addressed by exploiting recent advances in high speed data converters with multi-gigahertz bandwidths integrated with RF circuitry [37].

Until now, however, the challenge of developing suitable frequency-selective structures for the Snow Radar remained. Although numerous efforts have been directed toward the miniaturization of these filters[38-40], they are not ideal for a multi-chip configuration due to significant substrate heights and overall large sizes. Recently, advances in organic substrate materials, 3D printed interconnects [41] [42], and computer-aided design (CAD) tools have paved the way for the implementation of low-cost filters on these substrates, fully compatible with advanced packaging techniques.

Liquid Crystal Polymer (LCP) filters have seen many recent implementations due to their attractiveness as a compact, flexible solution [43-51], however, the full 2-18 GHz range has been largely lacking LCP filter implementations. A parallel-coupled stub-loaded resonator (PC-SLR) was designed and detailed in [50,52], and the promising results provide a path forward in continued miniaturization of the Snow Radar RF front end. A review of LCP filter literature and reported results are presented in Table 1.

Table 1: Summary of several LCP filter implementations and reported capabilities

Reported LCP filter	**Filter topology and technology**	**Operating bandwidth**	**Center frequency**	**Insertion loss near center frequency [dB]**	**In-band group delay/variation [ns]**
Multilayer BPF [43]	Capacitive-loaded transmission line resonators; 3-layer	3.9-10.1 GHz (3-dB)	7.0 GHz	0.58 @ 7 GHz	0.32/0.2 from 4.0-9.3 GHz
UWB SIR BPF [44]	Stepped-impedance resonator; 3-layer	2.2-9.9 GHz	6.05 GHz	0.18 @ 6.05 GHz	0.45/0.35 from 2.2-9.9 GHz
UWB Cascaded BPF [45]	HPF/LPF Cascaded single stage; 3-layer	3.5-10.0 GHz (3-dB)	5.75 GHz	0.35 @ 5.85 GHz	0.18/0.15 from 4.2-10 GHz
Flexible LPF [46]	Stepped-impedance resonator; 1- layer	0-10.0 GHz (3-dB)	5.00 GHz	1 for 0-8.5 GHz	Not reported
Pseudo-Elliptical BPF [47]	Fully-canonical modular via coupling analysis; multilayer	9.75-10.25 GHz	10.0 GHz	4 dB @ 10 GHz	Not reported

Broadside-coupled BPF [49]	Quasi-lumped BPF with broadside-coupled structures; 3-layer	2.6-10.2 GHz	6.4 GHz	0.25 dB @ 6.4 GHz	0.41/0.35 from 2.6-10.2 GHz
Multimode multilayer BPF [43]	Eight-pole radial capacitor quasi-lumped; 3-layer	1.8-10.05 GHz	5.925 GHz	0.32 dB @ 7.5 GHz	0.4/0.2 from 3-9 GHz
PC-SLR BPF [50]	Broadside coupled PCs with stub-loaded resonator; 3 layer	2-18 GHz	10 GHz	Not reported (est 0.1 dB)	Not reported

1.2 This Work

As mentioned in Section 1.1, the Snow Radar has seen numerous updates and iterations since the legacy Snow and Altimeter systems, but as with most electronic systems, miniaturization plays a major role in its continued development. The transmitter and receiver radio frequency (RF) front end of the Snow Radar have been reduced from fully-connectorized systems to singular compact modules, already providing a major reduction in size. The modular RF transmitter is operated with a 30-dBm transmit power and the receiver features 55 dB of gain and a noise figure of ~3.5 dB, and the systems have been field-operated. Voltage sequencing boards were designed to perform bias control for both subsystems, and integrated with the microwave circuitry. The modules, their ancillary sequencing boards, and laboratory and field measurements are presented in this document.

The next step to further reduce the size of these RF subsections is the transition to multi-chip module (MCM) systems, replacing the COTS "building block" based modules with fully integrated boards at the die level. To meet this demand, bare die RF components have been selected, but a major bottleneck was the custom band-pass and low-pass filters used in these systems. To facilitate further miniaturization, planar band-pass and low-pass filters have been developed, manufactured, and tested using an LCP substrate, reducing the (suspended substrate strip-line) BPF and LPF footprints from 4.25 sqcm and 3.62 sqcm respectively to only 1 sqcm each, while only retaining a thickness of 150 µm. With better than 10-dB input return loss across the passband and less than 1.5 dB insertion loss, the new filters will play a major role in the miniaturization of the Snow Radar's RF front end.

1.3 Thesis Outline

This thesis is organized in six chapters, as outlined below.

Chapter 2: Snow Radar Overview

In this chapter, background discussion of the principles of FMCW are detailed, followed by an overview of the Snow Radar and a discussion of the connectorized RF front-end reference system.

Chapter 3: Ultra-Wideband Transmit and Receive Modules

The compact "building block" based Tx and Rx modules are detailed, providing a discussion of their design and limitations, and a description of the designed voltage bias sequence circuitry to facilitate the operation of both the Tx and Rx subsystems. The various revisions of the receiver module are discussed, and measured waveforms and radar data are presented.

Chapter 4: 18 GHz Low Pass Filter

This chapter details the motivation, requirements and design of the new 18 GHz low-pass filter for use with the Snow Radar. Using the previous SSS filters as a benchmark for both performance, size, and cost, the filter design process is detailed from initial Chebyshev prototype to the panelized, manufactured LCP filters, ending with a discussion of the measured results and comparing them to the simulated results.

Chapter 5: 2-18 GHz PC-SLR Band Pass Filter

This chapter discusses the requirements for the new 2-18 GHz band-pass filters, designed to replace the in-use SSS high-pass filters for the Snow Radar. It features a detailed investigation of ultra-wideband band-pass filter design techniques, describes an initial value filter and discusses the computer-aided process used to verify their design. Finally, the manufactured panel, individual filters, and their measured performance is compared with simulated results and the performance again the benchmark SSS filters.

Chapter 6: Conclusions and Future Work

Finally, Chapter 6 summarizes the works achieved and presented in previous chapters and discusses the future of the Snow Radar, including next steps for implementing the RF front end as multi-chip modules, ongoing parallel work for planarizing the biasing and RF circuitry onto a single layer on FR408, and potential further miniaturization and improvement of the LCP filters presented in this thesis, and possible extension of the radar bandwidth to improve the system’s vertical resolution further.

2: Snow Radar Overview

2.1 Foundation of FMCW Radar Operation

As mentioned in Section 1.1, the Snow Radar is dual-mode but primarily operates as a frequency-modulated continuous wave radar system. While continuous wave (CW) radars operate by continually transmitting power at a target and detecting a frequency shift Δf in the received signal, frequency-modulated (FM) CW radars provide the distinct advantage of being capable of operating over a wide bandwidth without requiring a very high bandwidth data acquisition system. A generalized view of an FMCW radar is shown in Figure 1. The method of operation is shown in Figure 2.

The waveform generator creates a frequency-modulated waveform, often linearly modulated, such that the waveform sweeps between frequencies f_1 and f_2 over a pulse duration τ, and then repeats. The waveform is then power-split and input both to the local oscillator (LO) port of the mixer and the transmitter (Tx) amplifier. After amplification, the signal is broadcast at a target via the transmitter antenna; the signal travels distance D, is scattered by the target, and the reflected signal again travels distance D to the receive (Rx) antenna. The received signal is amplified and input to the RF port of the mixer, whereupon the two signals are multiplied together. For a single target, the multiplication of the Rx and LO signals results in a signal whose frequency is equal to

$$f_b = f_{RF} - f_{LO} \tag{1}$$

This output f_b is known as the Intermediate Frequency (IF), or the beat frequency and is obtained by performing spectral analysis on the output of the mixer. The output signal is then digitized in the time domain, stored, and displayed (typically in the frequency domain) for operator feedback.

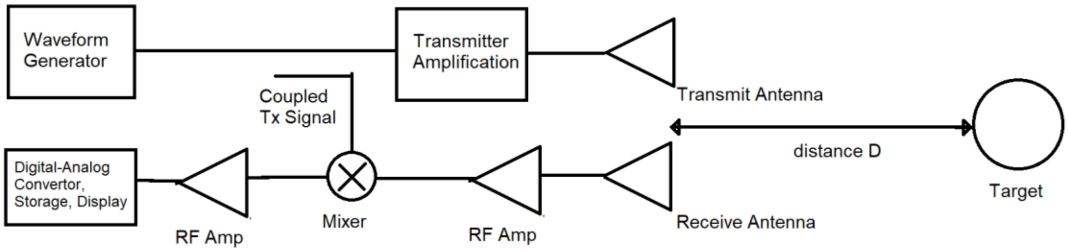

Figure 1: FMCW Block diagram and operation

Figure 2 is a frequency-time representation of the Rx and Tx/LO signals, illustrating the theory of operation enabling FMCW radar use; the blue signal is the waveform generator output, as coupled into the LO port of the mixer. The red line represents the signal received by the Rx antenna. With a single target, the received signal is a time-shifted copy of the transmitted signal, as it has experienced the travel distance $2D$ before being received. The difference in instantaneous frequency between the transmitted and received signals, the beat frequency, can be used to determine the time difference between the two waveforms, and therefore ascertain the distance to the target. Specifically, the beat frequency is related to the distance to the target and characteristics of the waveform itself.

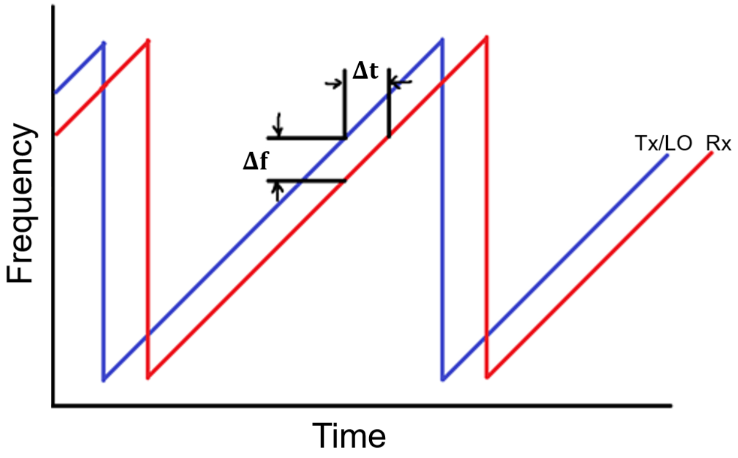

Figure 2: Illustration of the FMCW operation principle

The difference in time between the two signals Δt is proportional to the distance traveled and the velocity of the signal v_p.

$$\Delta t = \frac{2 * R}{v_p} \tag{2}$$

The instantaneous derivative of the frequency modulated chirp signal is

$$k = \frac{d(f)}{d(t)} = \frac{\Delta f}{\Delta t} \tag{3}$$

Thus, the beat frequency Δf is related to the change in time Δt, and therefore also related to the propagation speed of the signal within the medium, the chirp rate k of the waveform, and the range D to the target. If signal is propagating in the air, a close approximation to a vacuum for travelling electromagnetic waves (air has a refractive index of 1.0003), the speed of light c can be substituted for v_p. Hence, we can rearrange Equation 2 and substitute Equation 3 to achieve

$$\Delta f = f_b = \frac{2 * D * k}{v_p} \tag{4}$$

Additionally, a linear repeating chirp will have a chirp rate equal to the bandwidth of the signal divided by the duration of one sweep (pulse) of the signal. Hence,

$$k = \frac{BW}{\tau} = \frac{f_{max} - f_{min}}{\tau} \tag{5}$$

For a single target at a constant distance, the output beat frequency will be a constant value, as the range to the target is not changing. However, with multiple targets, or a target that produces multiple reflections, such as media with multiple layers (*e.g.*, snow cover), the spectral content of the received signal will include peaks associated with frequencies (and therefore time shifts) corresponding to the distances to targets or points of sufficiently strong reflection. To properly distinguish two distinct specular targets, they must be separated by enough distance such that the spectral components of each (after receiving the signal and performing a Fourier Transform) are distinguishable. Figure 3 displays this concept; two specular targets, even if perfectly and singularly reflective, will be difficult to distinguish around the ideal beat frequency due to the non-infinite observation time. If these two signals are not separated by enough time (*i.e.*, if the targets are not distinct enough in range), it can become difficult to distinguish the two signals from one another.

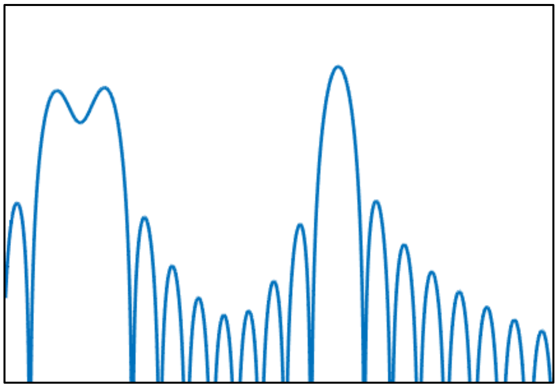

Figure 3: Example spectrum of multiple targets overlapping

Considering a single target at a constant observed for T seconds, the received signal is a windowed tone with a length of T seconds, and thus the Fourier Transform of this signal is the convolved transformed waveform: a single-valued frequency peak, “smeared” by a $sinc(x)$ function with nulls at $\pm\frac{1}{T}$. Thus, since distinguished two objects at varied range is equivalent to the determining the temporal resolution, Δt, of the two signals, the range resolution, Δr, can be determined from the temporal resolution, and the frequency components will be distinguishable with the inverse of observation time $1/T$. The chirp rate, $k = BW/T$, informs that the range resolution of a chirped FMCW radar system is

$$\Delta r = \frac{A * c}{2 * BW * \sqrt{\epsilon_r}} \tag{6}$$

The value A is a windowing factor; the rectangular window can be modified using a variety of window functions, such as the well-known Hanning or Hamming windows, which employ a raised cosine weighting function across the rectangular window. The windowing function can reduce sidelobes from -13 dB to -31.5 dB or lower [53], and thus lead to an increased value of A and improved detection capabilities at the expense of a slight broadening of the main lobe.

The range resolution of an FMCW radar is thus dictated by the chirp bandwidth. However, the range resolution of a radar will also be degraded by hardware and operational limitations – specifically, the transmitted waveform will not have perfect linearity, due to either the waveform generator itself or non-linear effects of the Tx amplifiers used to increase power of the transmitted signal. Due to this non-linear behavior, the mixer’s IF output will differ from a constant frequency value even with a single target at a fixed distance. Careful conditioning of the analog signal, minimizing internal matching reflections, limiting negative effects due to cabling and impedance discontinuities, and reduction of non-linear effects assist in approaching the ideal range resolution of the radar.

2.2 UWB Snow Radar System

The newest version of the ultra-wideband (UWB) Snow Radar is a 2-18 GHz system with heterodyne and homodyne operating modes[2]. It was built upon earlier versions of the same radar, to serve as a performance baseline to guide future miniaturization efforts. A simplified block diagram of the radar system is shown in Figure 4. The homodyne mode operates as conventional FMCW, employing a 2–18 GHz bandwidth, with a 240-µs sweep time, generating the signal using the Keysight M8195 arbitrary waveform generator (AWG). The heterodyne mode also uses a chirp, with a reduced frequency range of 2–14 GHz (due to AWG memory constraints), with a 200-µs pulse length, generating the transmitted signal and the LO signal using two separate channels from the AWG. Both modes employ a 250-µs pulse repetition interval (PRI), or equivalently a 4-kHz pulse repetition frequency (PRF). The conditioned received IF data is digitized and stored with the radar's data acquisition subsystem, consisting of a 4-channel 500-MHz analog bandwidth digitizer operating at 250 MSPS, Virtex-5 SX95T field-programmable gate array (FPGA), an embedded control computer and solid-state hard drives.

---

[2] Earlier versions operated in the 2-8 GHz frequency range in surface [14] [84] and airborne configurations [1] [85]; and in the 2-18 GHz frequency range in homodyne FMCW mode for low-altitude airborne operation [25]. For a detailed timeline of the earlier versions of this system, the reader is referred to [8].

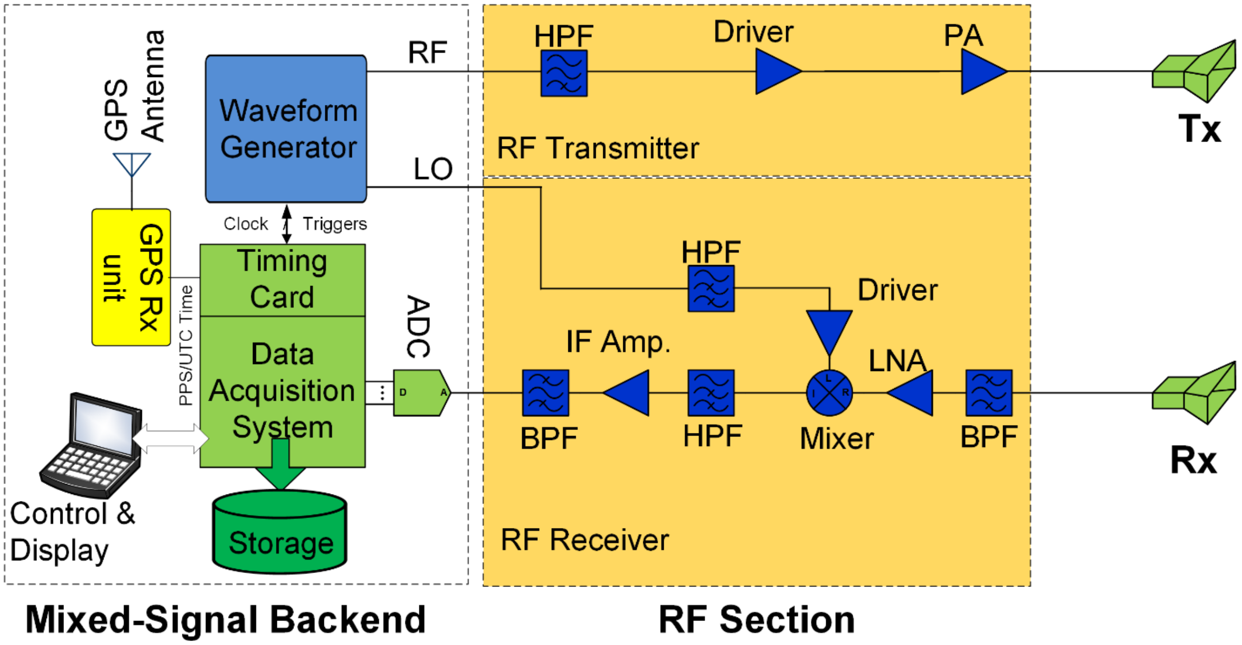

Figure 4: Radar block diagram [30]

The RF front end consists of both transmit and receiver modules. The Tx subsystem features two stages of gain and a high-pass filter to remove out-of-band, low frequency spectral content generated by the RF waveform generator module. The Tx has a maximum nominal transmit power of 1 W. The Rx subsystem features the same high-pass filter for removal of spurious content on the LO signal from the AWG, which is fed into the LO port of a high-isolation mixer. The mixer is also fed the amplified received (and time-delayed) signal on its RF port. The radar's mixer output is input to the radar's IF subsystem, consisting of an IF amplifier and 4-band filter bank for anti-aliasing, each with a 125-MHz bandwidth. The four bands are associated with four distinct range windows, corresponding to the IF frequencies—and therefore ranges to target—that fall within those bands. The Tx and Rx subsystems are discussed in more detail in Sections 1.2.2 and 1.2.3, respectively.

The radar's theory of operation and timing diagram is shown in Figure 5. Fig. 5.a shows the conventional, homodyne operation, while Fig. 5.b shows the heterodyne (or time-delayed stretch processing) mode. For conventional, low-altitude operation, the transmit and LO signals are identical, and when the received signal is mixed with the LO signal, the resultant IF data corresponds with the round-trip travel time of the signal (as well as the delays induced by the subsystems and cable run to the antennas). For time-delayed stretch processing mode, the signals are generated with an induced, pre-calculated time delay. Thus, the LO signal is delayed by τ_d, and resultant IF frequency is reduced. Instead of corresponding to a "true" travel-time delay, which would result in IF data outside of the operating band of the digitizer, since the LO is pre-modified with this known, induced delay, and the IF signal falls within the radar's IF bandwidth.

To accommodate for additional signal intensity loss over the greater distance, the radar is equipped with two Tx modules; one module has ~20 dB of gain and 20 dBm of output power, for low-altitude operation, and the other has ~30 dB of gain and 30 dBm of output power. Figure 5(c) shows the timing of PRI triggers, generated by the AWG, relative to the pulses. As the Tx/LO chirp begins, the PRI signal is sent to the FPGA, which waits for 8 total signals, indicating pre-sum timing; during this time, each of the 8 sets of IF data is pre-summed onboard, prior to data storage. The FPGA then generates an extended PRI (EPRI) signal, which triggers storage of the pre-summed data and provides the spectral data to the operator display. The UWB Snow Radar has been field-operated multiple times over the course of multiple field seasons between 2017 and 2019, replacing the legacy 2-8 GHz and 12-18 GHz systems [30]. It has been proven at both nominal and high altitude, achieving ~1.4-cm and ~1.13-cm range resolution in air and snow, respectively, during conventional operation (*i.e.*, ~1,500 ft AGL, corresponding to a round-trip signal travel time of ~3 μs). Its most recent iterations have accumulated more than 1,200 flight hours.

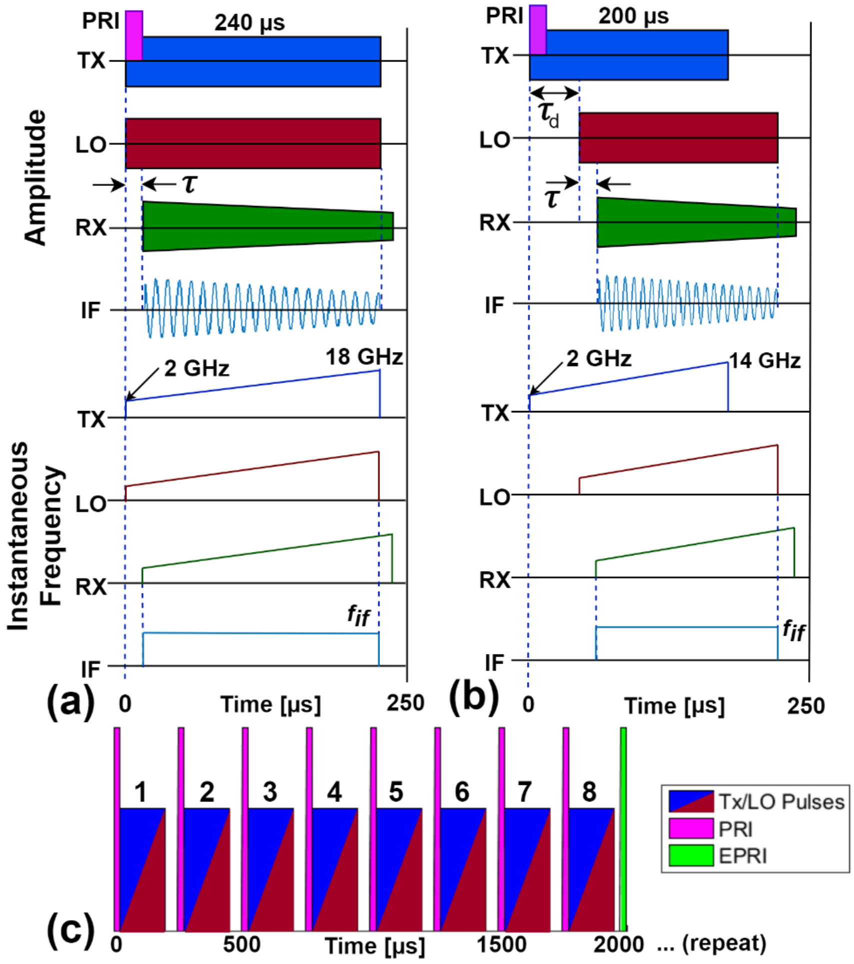

Figure 5: Snow Radar timing diagram

2.3 Connectorized Radar RF Front End

A connectorized RF front end was developed and flown onboard the NASA P-3 Airborne Science Laboratory for the Operation IceBridge project in spring, 2017 [54]. The connectorized system served to replace to 2-8 GHz legacy Snow Radar system and the 2—18 GHz Ku-band altimeter system while providing an initial performance benchmark for miniaturization. This system was outfitted in a 19” module for rack mounting, and an image of the system is shown in Figure 6. Data collected and processed using the reference system during a transect flight to the North Pole is shown in Figure 7, showing the capabilities of the system to measure snow cover thickness on sea ice with cm-scale vertical resolution. The compact systems that replaced this connectorized RF front-end and their block diagrams, biasing circuitry, and various revisions are discussed in detail in Chapter 3.

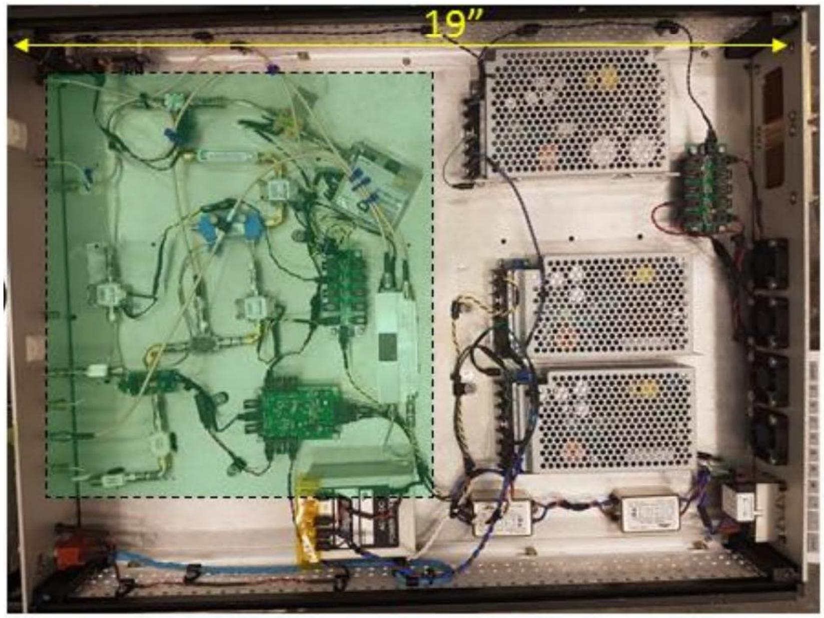

Figure 6: Connectorized reference system RF front end (green highlight: Tx and Rx systems)

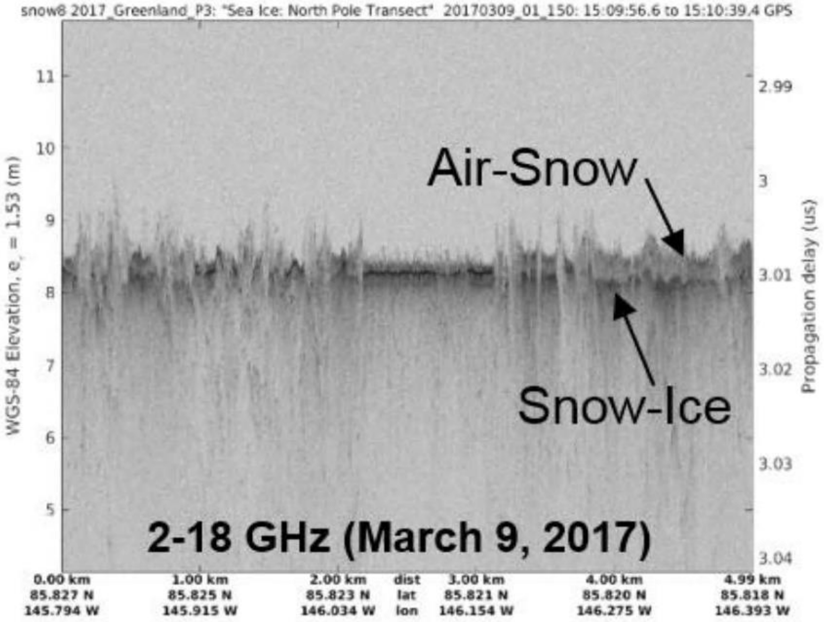

Figure 7: Processed radar image from measurements taken in 2017 Arctic OIB field season using reference system

Chapter 3: Compact Ultra-wideband Transmit and Receive Modules

After successful validation of the reference system, subsequent miniaturization efforts of the RF front end required the definition of a common chipset compatible with planar integration. A set of transmit/receive modules based on packaged chips was developed and tested. The goal of this effort was to evaluate the performance of various devices (active and passive) to define a base configuration that could be further packaged in the future. All the chips – except for the filters – have unpackaged die equivalents. These modules and their performance are described in this chapter.

3.1 Ultra-wideband Tx Module

3.1.1 Transmitter Overview

The transmitter block diagram is shown in Figure 8. The transmitter can be simplified into three primary sections: filter, driver amplifier, and high-power amplifier. The filters are custom-made high-pass filters with a 2-GHz lower-band cutoff frequency; they are designed as suspended-substrate stripline (SSS), utilizing a custom enclosure [38]. The filters were made into drop-on components by removing the field-replaceable connectors and creating a coaxial-to-CPW transition, built into the housing. The driver amplifier is the Qorvo TGA2567, featuring 2-20 GHz bandwidth and adjustable, nominal 17 dB gain, requiring a 5-V drain voltage and two gate voltages to adjust output power and gain. The high-power amplifier stage is the Qorvo GaN-on-SiC TGA2214. This amplifier has a 2-18 GHz bandwidth, nominal small-signal gain of 22 dB, and requires a drain voltage of 22 V, drawing a nominal quiescent current of 450 mA, with a gate bias voltage of -2.3 V. The transmitter also features a 3-dB attenuator to reduce internal reflections and two gain equalizers to compensate amplitude roll-off at higher frequencies. Capable of up to 4 W of output power, the transmitter is typically operated with a 1 W (30 dBm) output power to reduce in-band harmonic content. The Tx module is supplied sequenced power by a custom biasing circuit for component safety, described in detail in Section 4.3.1.

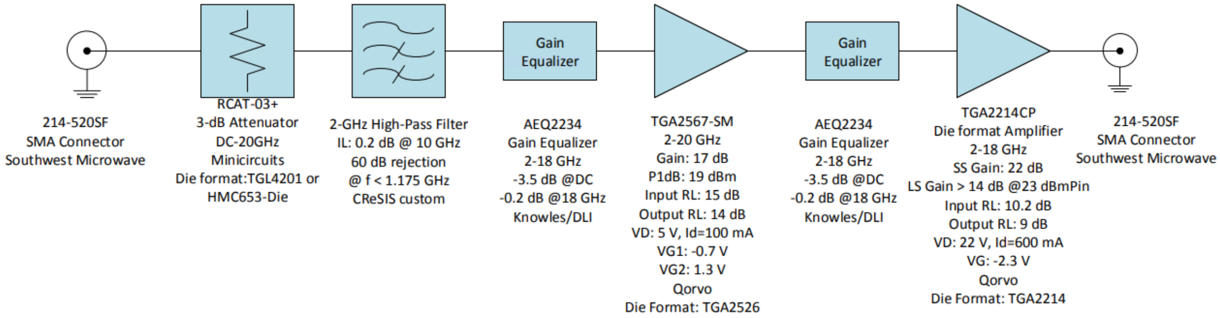

Figure 8: Transmitter detailed block diagram

3.1.2 Compact RF Transmitter Modules

The once-connectorized radar front end was highly compacted using X-microwave "building blocks" [36]. The X-microwave framework [55] allows individual components to be installed in carrier cards and connected within a regular grid pattern using coplanar waveguide "jumpers" as demonstrated in [56], allowing rapid prototyping, evaluation, and implementation of RF networks using a variety of components and configurations [57]. The compact system was since used to collect snow cover data during the 2018 and 2019 NASA Operation IceBridge field seasons. A CAD drawing of the compact Tx module is shown in Figure 9, and Figure 10 is a picture of the realized module. The module is 4" in length and 2.5" in width. To retain separation of the RF/microwave circuitry and the power supply components, DC-power is supplied via a C-Grid connector attached to a biasing board on the back side, the design of which is detailed in the next section. Excluding the filter, all components are X-microwave block components, connected using planar signal jumpers. The RF components from X-microwave are specifically designed to align to a grid of 1-72 screw holes separated by a fixed distance provided by the manufacturer. We created a custom-machined block to accommodate the required grid pattern and serve as a heat sink for the power amplifier, as its efficiency is relatively low at ~10% – it is operated at only 1 W, well below its 1-dB output compression point (P1dB), but good linearity and reduction of in-band harmonics is required.

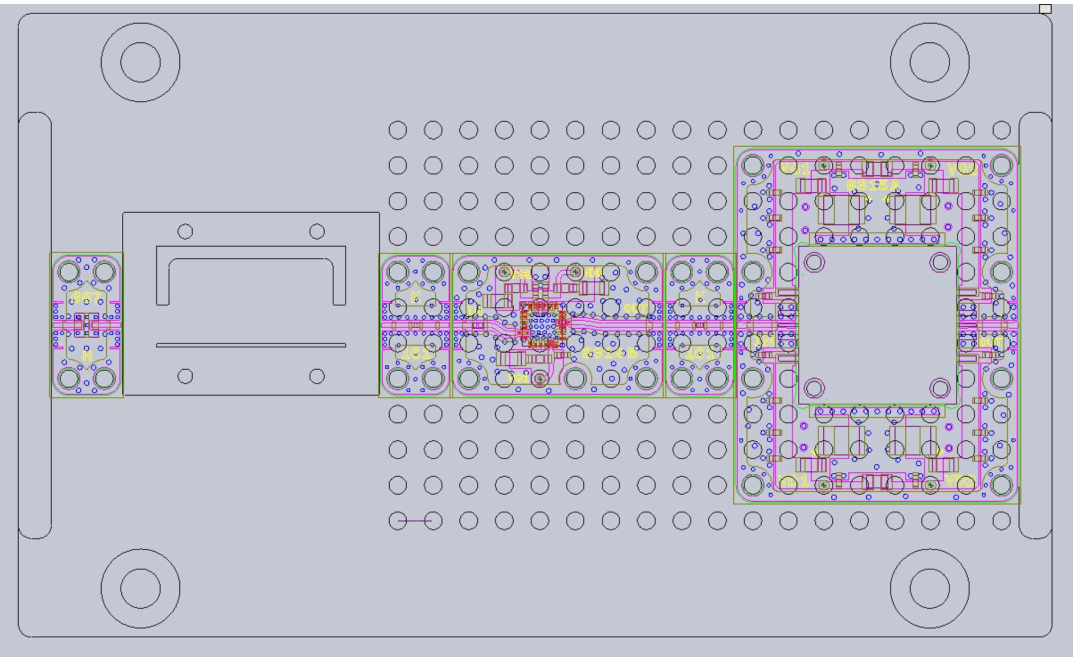

Figure 9: CAD drawing of compact RF transmitter

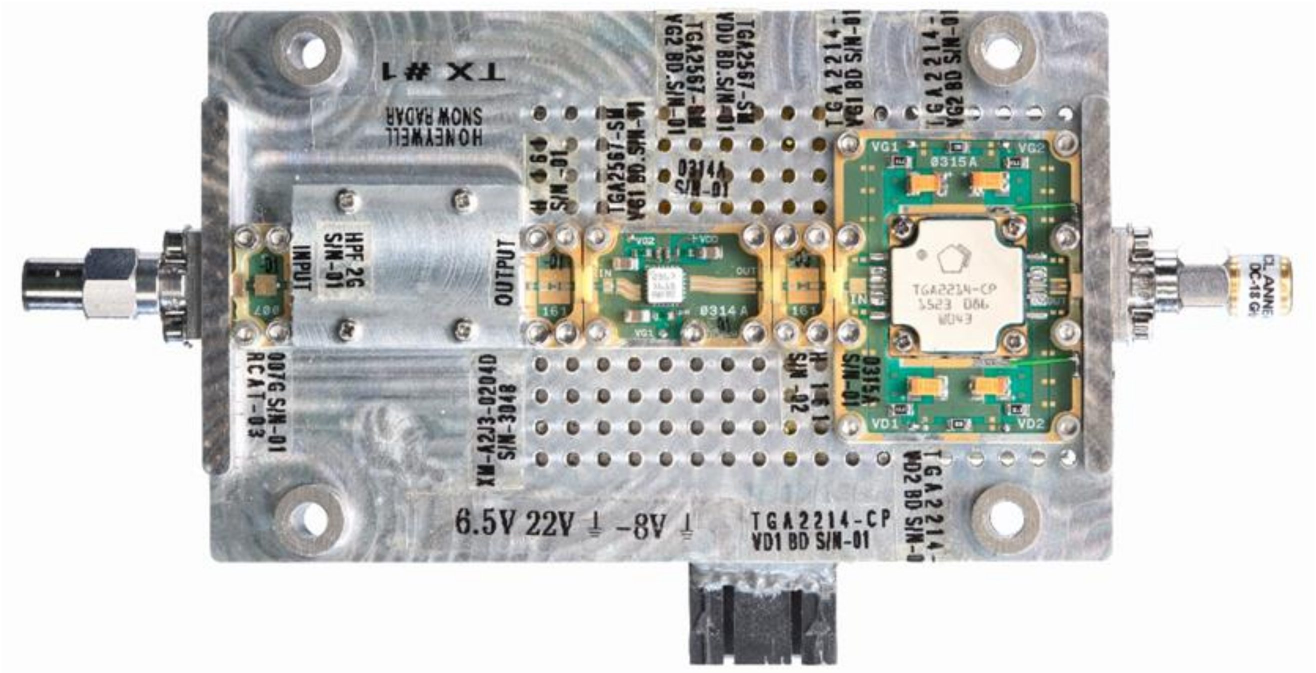

Figure 10: Photograph of compact Tx module

The AWG-generated transmit RF signal is first passed through a Minicircuits RCAT-0X+ attenuator (X-Microwave part XM-A232-0204D) to improve matching to the input of the Tx subsystem. It is followed by a custom 2-18 GHz bandpass filter, required for its high-pass characteristic, and measuring 964×683 square mils. To account for Tx gain rolloff at increased frequencies, the filter is followed by a Dielectric Laboratories AEQ05467 gain equalizer (X-Microwave part XM-A2H7-0204D). The first gain stage is the 17-dB TGA2567-SM from Qorvo (X-Microwave part XM-A3J2-0604D), which is followed by an additional gain equalizer identical to the aforementioned. The final feature of the compact module is the TGA2214CP 22-dB amplifier (X-Microwave part XM-A3J3-0810D).

3.1.3 Tx Biasing and Power Boards

Both active components of the Tx module require DC voltages for power and biasing. These voltages must be carefully applied, as they are depletion mode devices and their gates require a negative voltage bias; if the drain voltage is applied without biasing the gate first, the components can draw excessive current and fatal damage can occur. For the TGA2567 [58], a 5-V drain voltage is required, but as the device is an adjustable-gain amplifier, it requires two gate voltages (nominal V_{G1} = -0.7 V and V_{G2} = 1.3 V) with a quiescent drain current of 100 mA. The TGA2214 datasheet [59] specifies a drain voltage of 22 V, and a typical -2.3-V gate voltage is required for a nominal quiescent drain current of 450–600 mA.

To properly sequence these voltages, a DC-voltage biasing board was designed, using the existing module drawing as a reference for size. The board was designed to mate to the back of the module, and the sequenced voltage outputs are fed via wire through the existing holes in the module to connect with the X-Microwave blocks. The board is supplied by 6.5, 22, and -8 V voltage rails and 0-V ground reference voltages. A linear low-dropout voltage regulator generates a 5.2 V rail from the 6.5-V input voltage. This voltage is used throughout the board to power a variety of components for biasing. An additional voltage regulator is used to create a -2.39 V rail, which is used exclusively for biasing and sequencing the TGA2214.

For the TGA2214, the sequencing method is shown in Figure 11. The -2.39-V gate voltage is created on-board and applied to one input of an LT1011 negative voltage comparator and compared to a ratio of the -5-V rail. Once the gate voltage settles and is greater than the specified voltage divided -5 V rail, the output of the comparator goes low (0 V). This signal is inverted (low to high) and input to a relay (CPC1020N). When the relay input is high (5 V), the relay output-side pins are internally connected, and the 22-V voltage rail is passed to the drain of the TGA2214.

Through this, 22 V only will pass to the TGA2214 drain when the gate voltage has surpassed a requisite negative threshold (-2.14 V, 90%).

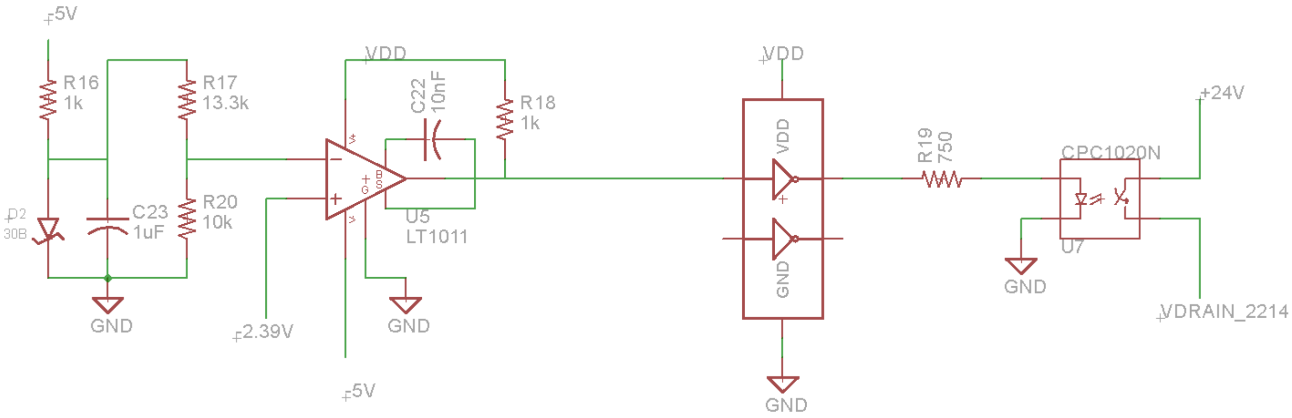

Figure 11: Schematic of the TGA2214 bias sequence circuitry

The TGA2567 requires multiple gate voltages, and a dedicated sequencing chip is used for sequencing. The Hittite HMC980 is an active bias controller [60]which automatically adjusts gate voltages to achieve a constant drain bias current. The functional diagram of the HMC980 is shown in Figure 12. The target drain current is specified by a resistor to ground, connected to the ISENSE pin, pin 20, and is calculated by $I_d = 150/R_{sense}$. As the TGA2567 requires a quiescent drain current of 100 mA, a 1.5-kΩ resistor is connected between the pin and ground. To account for potential variation in resistance value, the resistor is placed in parallel with an unpopulated resistor, such that two valued resistors may be combined to achieve the necessary resistance with more precision, if needed. Additionally, a divider network is connected to the VG2_CONT pin to specify the gate voltage by

$$V_{G2} = V_{dd} * \frac{R4}{R3 + R4} - 1.3 \tag{7}$$

The values of the divider network are R3 = 4.32 kΩ and R4 = 4.22 kΩ, yielding a V_{G2} gate voltage of 1.27 V. The S0 and S1 pins are internally pulled "high" and should be connected to ground depending on the desired drain current. They are connected to an optional pair of resistors to ground that are unpopulated, but the inclusion of these resistors allows for on-board programming of the board, depending on the desired load. The EN pin is left floating, as connecting it to ground bypasses all bias control and disables the chip.

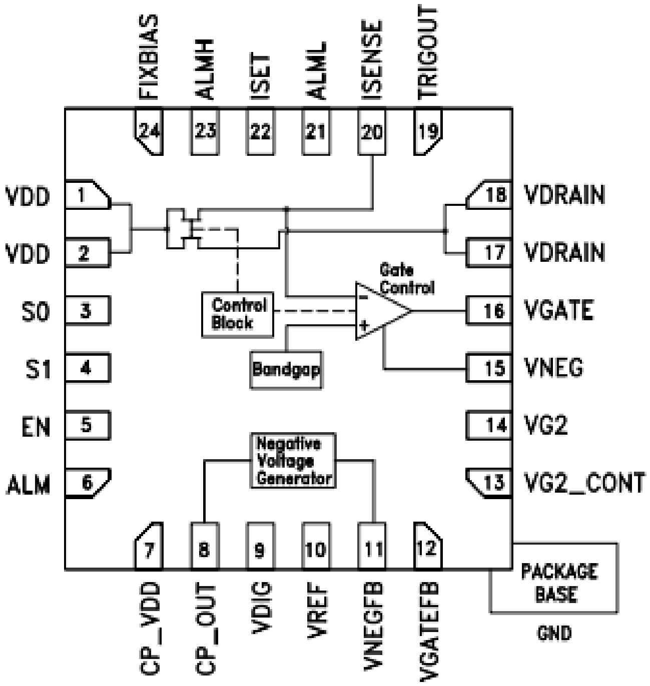

Figure 12: Functional diagram of HMC980 bias controller [60]

The CADSoft Eagle schematic is found in Appendix B, detailing the circuit nets and components in full. A layout view of the biasing board is shown in Figure 13. It measures 2.37 × 2.43 sqin and is designed on a 62-mil FR4 board material. Each hole for the sequencing outputs is an unplated via to avoid shorting to the aluminum module. The board was manufactured by Sierra Circuits, and Kapton tape was used on the bottom side to avoid shorting the signal/rail vias when installed. An image of the manufactured, populated, and installed biasing board is shown in Figure 14.

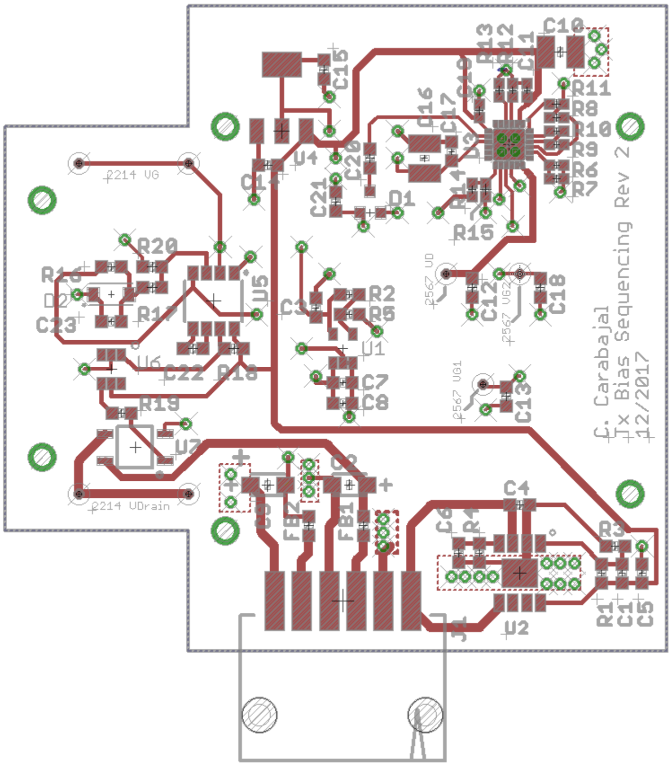

Figure 13: Compact transmitter biasing/power board layout

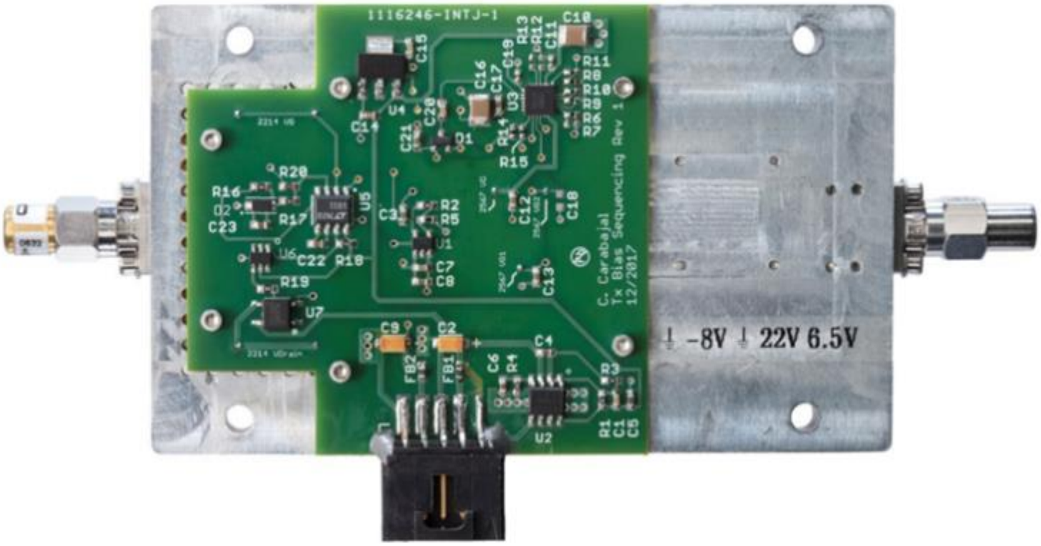

Figure 14: Tx biasing board installed on transmitter compact module

Operation of the voltage sequencing for the TGA2214 was tested in the laboratory. The 22-V supply drew 600 mA; The 6.5-V supply drew ~200 mA nominal. The -8-V supply was substituted with a -13.5-V supply and drew < 50 mA. The total power consumption of the module is ~15.2 W. The captured waveforms are shown in Figure 15. The blue waveform is the gate voltage, and the purple waveform is the drain voltage. The gate voltage drops to the requisite -2.3 V and the relay activates ~4 ms after, while the drain voltage is still rising to its maximum. The drain voltage reaches the nominal 22 V after 16.8 ms.

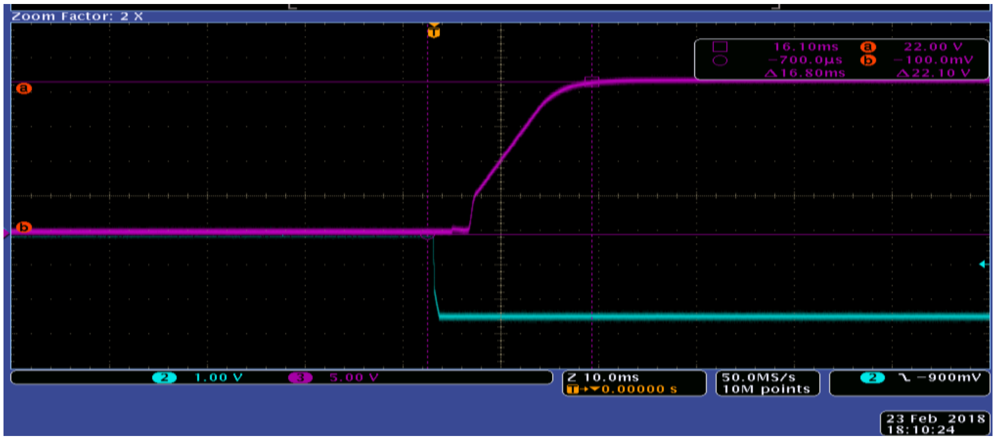

Figure 15: Measured waveforms of TGA2214 voltage sequencing

Figure 16 shows the sequencing operation of the TGA2567. The blue waveform is the gate voltage, the purple waveform is the drain voltage, and the yellow waveform is the gain control gate voltage. The gate voltage V_{G1} falls negative over ~2 ms, far exceeding its nominal value, until it is sufficiently low to activate the drain and AGC gate voltages, then rises until reaching -0.7 V.

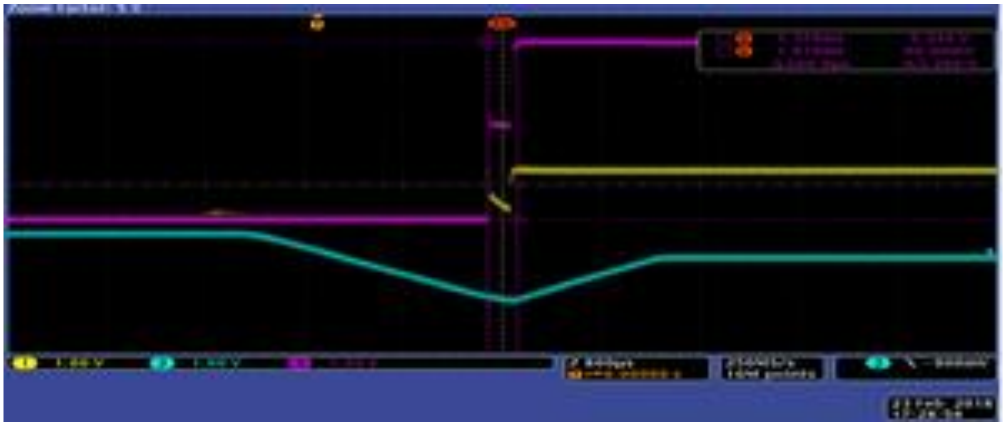

Figure 16: Measured waveforms of TGA2567 voltage sequencing

The scattering parameters of the modular transmitter were tested in the lab with a vector network analyzer (VNA). The plotted results are shown in Figure 17. In comparison to the connectorized system, the compact Tx module exhibits ~10-dB higher gain across the band, due to the inclusion of the 4-W TGA2214 amplifier, under-driven to an output power of 1 W. Variation in the response is largely due to the response of the high-power amplifier. The transmitter exhibits more than 30 dB gain across the 2-18 GHz system bandwidth. The gain matched the expected value as per the manufacturer's supplied S-parameters for individual components in the chain. Digital pre-emphasis is implemented using the AWG to accommodate for variation in the transmitter frequency response.

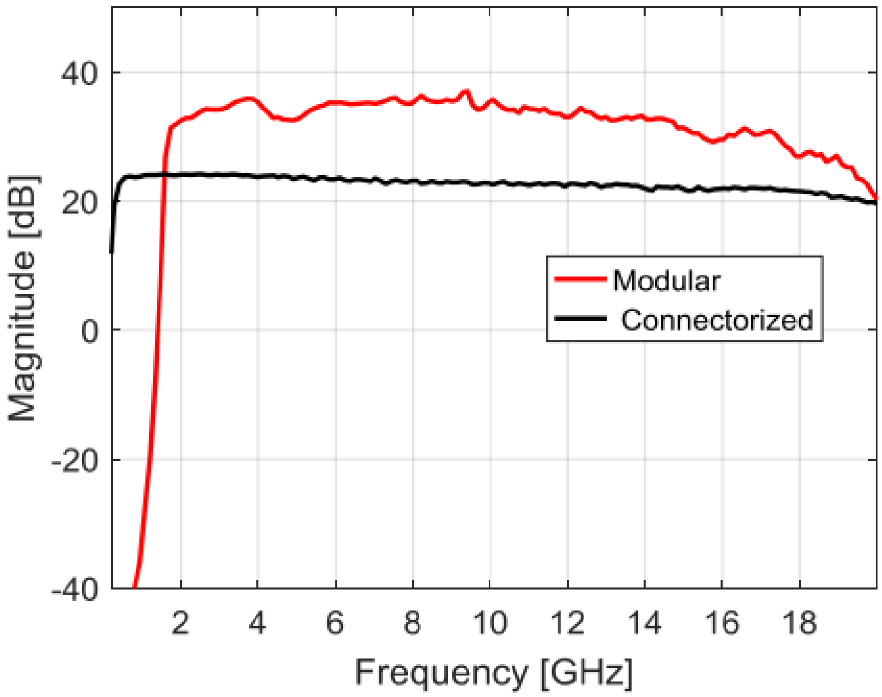

Figure 17: Measured gain of the modular Tx and comparison with its connectorized counterpart

3.2 Ultra-wideband Rx Module

3.2.1 Receiver Overview

The receiver block diagram is shown in Figure 18. Two key components of an FMCW radar are the de-chirping mixer and the low-noise amplifier (LNA). We evaluated various mixers and LNAs to determine the best possible configuration. The two best performing mixer components were the (Marki) T3-20 triple-balanced mixer, with a 0.01-20 GHz bandwidth and a required LO drive power of 15-27 dBm, with nominal 15-dB LO-RF isolation and conversion loss of 8.5 dB; and the Miteq DB0218 with a 2-18 GHz bandwidth, 7-13 dBm LO drive, typical 30 dB LO-RF isolation and 6.5-dB conversion loss. We found the Miteq DB0218 had superior performance, although it does not have a die-based or unpackaged version. We therefore pursued its integration as a drop-on component, removing its field-replaceable connectors and properly transitioning its coaxial output to CPWG in the X-Microwave modules.

The RF path uses the HMC463 as its initial gain stage and primary driver for receiver noise figure (NF) and reverse isolation, requiring a 5-V supply voltage. The LO path features the Analog Devices HMC606 amplifier, which has a 2-18 GHz operating bandwidth, 14-dB gain, used to amplify the coupled AWG chirp signal for use at the mixer LO port. The HMC606 requires a voltage supply of 5 V. It is followed by an additional gain stage, the Qorvo TGA2567 adjustable-gain 2-20 GHz amplifier, which features 17 dB of gain and requires a 5 V drain voltage drawing 100 mA quiescent current and two gate voltages, -0.7 V and 1.3 V nominal, although these are adjusted to achieve desired I_{DQ} and amplifier gain respectively. The IF signal is input to an 4-section absorptive high-pass filter with 10 MHz cut-off frequency, amplified with the 63-dB Miteq AU-1291 amplifier (not included in the microwave module), and passed into the 4-band anti-aliasing filter bank. The Rx module also features several Minicircuits RCAT-series 1-4 dB attenuators between active microwave components to improve matching between their ports and reduce amplifier input power to avoid saturation. The receiver has ~55 dB gain and a noise figure of ~3.5 dB. The biasing circuitry and the design variants are discussed in detail in Section 3.3.2.

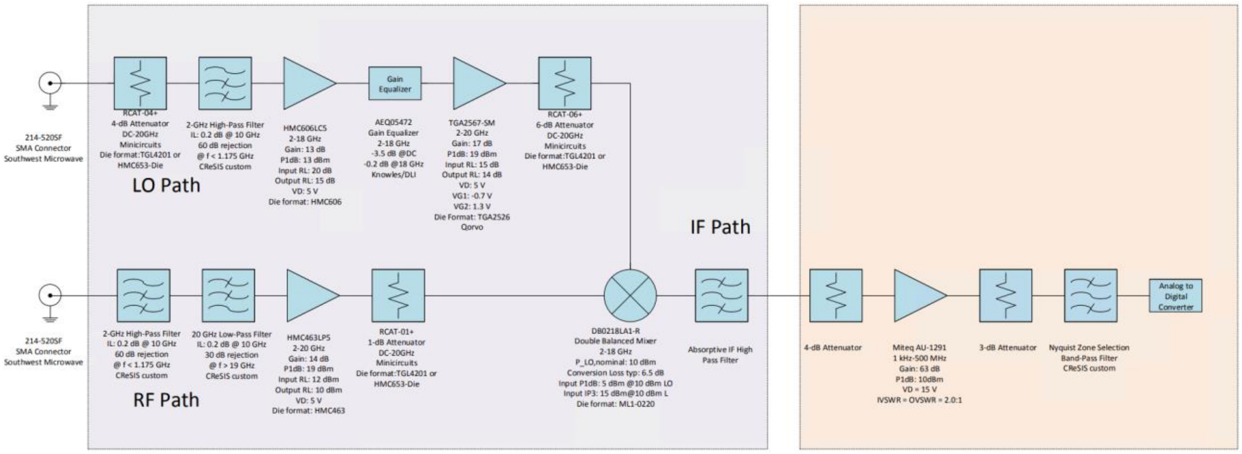

Figure 18: Receiver detailed block diagram

3.2.2 Compact RF Receiver Modules

Three receiver module revisions were made to accommodate different hardware, but this discussion will detail the “rev 1” module, as most of the hardware and dimensions are similar. A CAD drawing of the compact Rx module is shown in Figure 9. The module is 5.87” in length and 2.75” in width. Power is supplied via a multi-pin C-Grid connector attached to a biasing board on the back side, the design of which is detailed in the next section. Many of the components detailed in the CAD drawing are X-microwave boards, connected using jumpers, and align to the same grid structure discussed in Section 3.1.2.

The module has two inputs (RF and LO) and one output (IF). The RF signal is received from the antenna and is first passed through a Minicircuits RCAT-0X+ attenuator (X-Microwave part XM-A232-0204D) to improve matching between the antenna/cable run and the RF path. It is followed by the custom 2-18 GHz bandpass filter. The BPF is composed of a high-pass and low-pass filters cascaded, and used to filter out out-of-band interfering signals captured by the antenna (*e.g.* from other systems onboard the platform) or coupled onto the input. The next device in the RF path is the 13-dB HMC463 low-noise amplifier from Analog Devices (X-Microwave part XM-A343-0604D). To improve the amplifier’s output match, it is followed by an RCAT-01 attenuator and fed into the RF port of the Miteq DB0218 mixer.

The LO path receives a chirp signal from the AWG and first uses an RCAT attenuator to improve matching. A custom high-pass filter is again used to filter out low-frequency noise from the digital system and coupled signals from other systems. The 13.5-dB, 15-dBm HMC606 amplifier with low phase noise (X-Microwave part XM-A2A5-0404D) is used for a first stage of gain, followed by the AEQ05467 gain equalizer. As a secondary gain stage and to boost the LO power to requisite levels for the mixer, a TGA2567 amplifier is used (identical to that used in the transmitter subsystem). Between the amplifier and the mixer's LO port is another RCAT attenuator to improve matching.

Other versions of the Rx module were designed to accommodate updated SISL filter designs and to integrate the IF filter bank and gain stages into the module, each with incremental improvements but largely identical performance, as mentioned above.

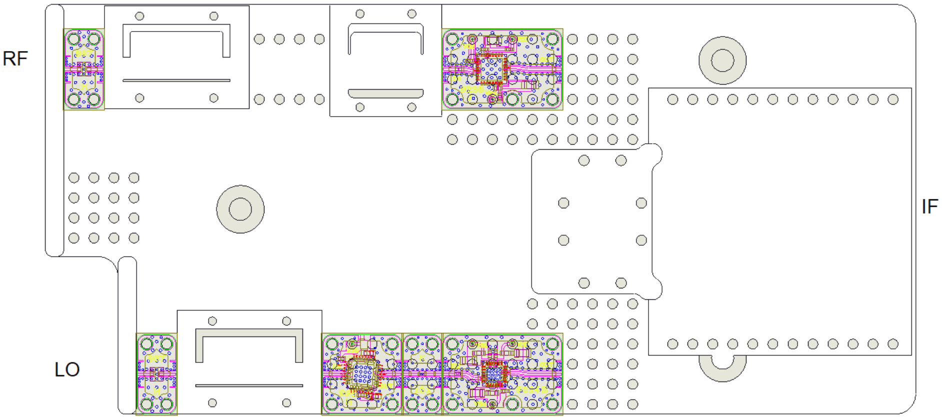

Figure 19: CAD drawing of compact Rx module

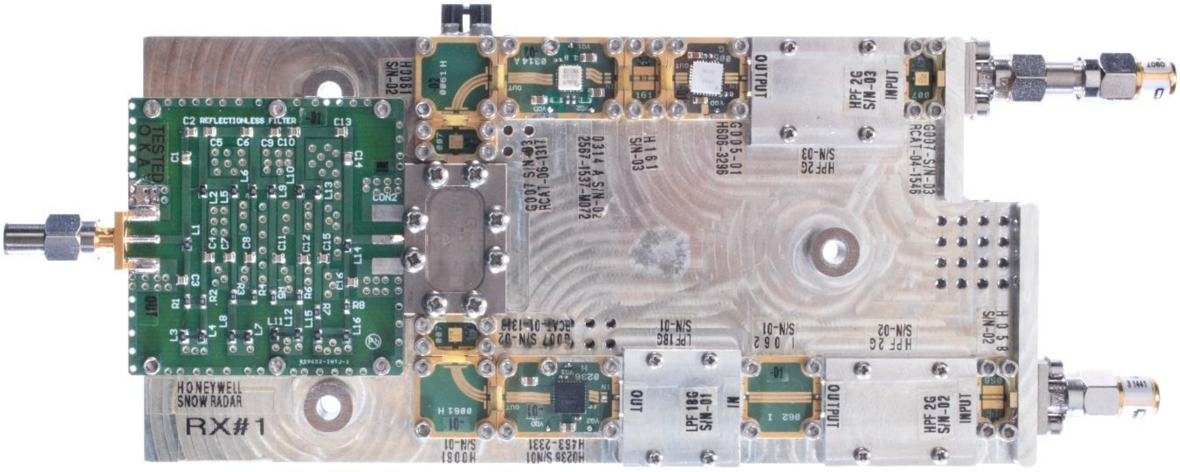

Figure 20: Photograph of the compact receiver module

3.2.3 Rx Biasing and Power Boards

The receiver module contains three active devices in the RF and LO paths in total. The TGA2567 requires the same biasing sequence and voltages as described in Section 3.1.3. The HMC606 [61] requires a supply voltage of 5 V and a drain current of 64 mA typical. The HMC463 requires a 5-V drain voltage drawing 60 mA current, and requires a gate voltage V_{gg1} of -0.9 V nominal and an optional V_{gg2} adjustable gain control (AGC) control bias voltage.

In tandem with the biasing board detailed in Section 3.1.3, a DC-voltage biasing board was designed to properly sequence the receiver device voltages. The board was designed to mate onto the back of the receiver module, and the sequenced voltage outputs are fed via wire to connect with the active devices. The board is supplied power via a 2-pin C-Grid connector with 6.5 V and a 0-V ground reference. The board features two LDO voltage regulators to generate 5.2 V and 3.3 V.

For the HMC606, only a 5-V drain voltage is required, and testing showed that a 5.2-V drain voltage resulted in acceptable performance. Hence, no sequencing was needed on the board, and the regulated 5.2-V rail was connected directly to the HMC606. The TGA2567 was biased identically to the one used in the Tx module, and thus its description is not repeated here. For the HMC463, a nominal 60-mA drain current is required, and the HMC980 is used again for bias control. To achieve 60-mA drain current, the ISENSE pin is connected to parallel set of resistors, one left unpopulated and the other with a value of 2.5 kΩ. The unpopulated resistor may be used to fine-tune the total equivalent resistance of the parallel pair if the desired drain current is not achieved. The S0 and S1 pins again feature unpopulated resistors to ground, and the EN pin is left floating, as it is internally pulled high. Although the HMC463 features optional gain control, it is not used in this system; however, to generalize the biasing board’s design, the voltage divider used to set V_{g2} for the HMC980 is still allocated layout space on the board, but the resistors are left unpopulated. Additionally, the net from the VG2 pin to the Vg2 hole on the board is disconnected by an unpopulated resistor, but it may be populated with a 0-Ω resistor in case the gain control is desired.

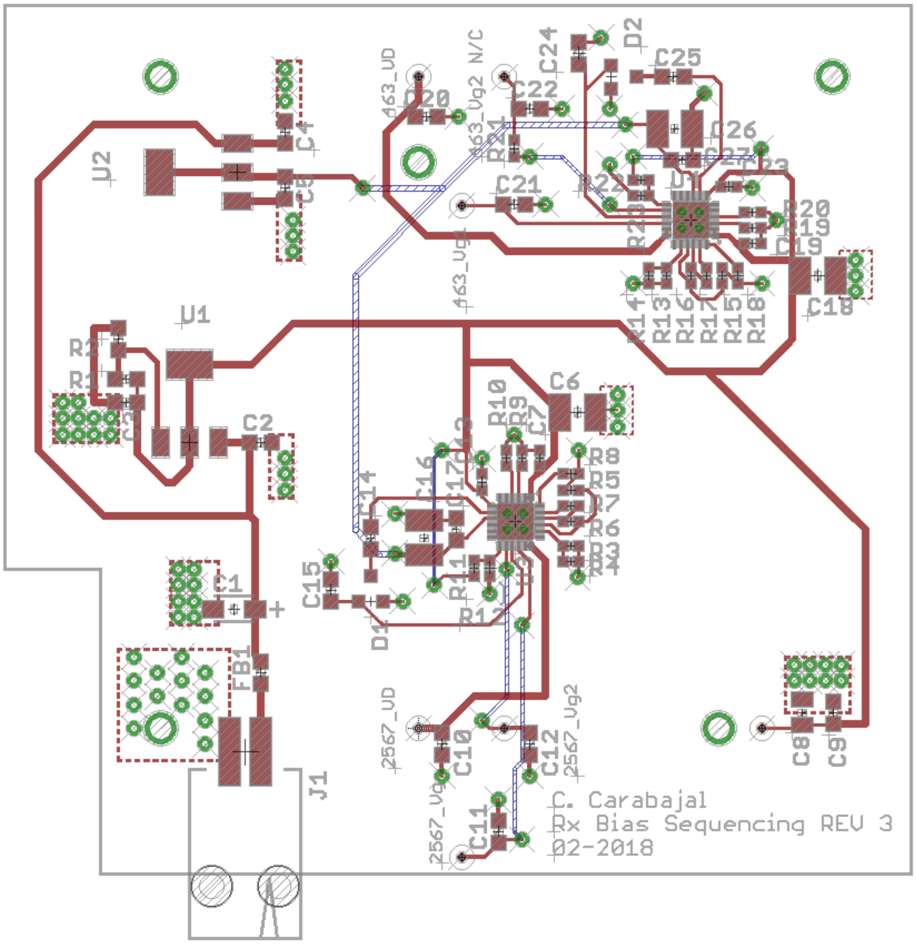

Figure 21: Compact receiver biasing/power board layout

The Eagle schematic of the Rx biasing board can be found in Appendix B. A layout view of the rev 1 module biasing board is shown in Figure 21. The board layout initially featured several “jumper” 0-Ω resistors to connect disparate lines, as routing the nets directly was not found to be possible (although a full topological analysis of the board was never performed). The board was instead revised to a 3-layer stack-up, making use of the middle layer to route various voltage rails. The board was manufactured by Sierra Circuits, and Kapton tape was used on the bottom side to avoid shorting the signal/rail vias when installed on the module. An image of the manufactured, assembled, and installed biasing board is shown in Figure 22.

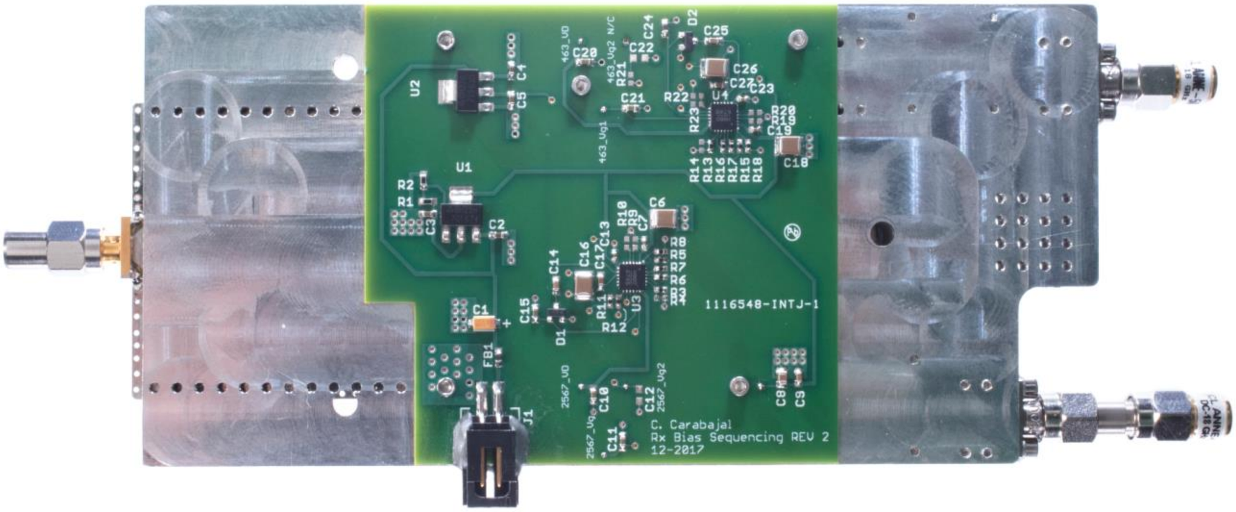

Figure 22: Photograph of biasing board installed on compact Rx module

VNA measurements of the modular receiver taken and the Rx conversion gain is compared to the connectorized system in Figure 23. The estimated conversion gain based on the specifications of the microwave components and IF circuitry is ~60 dB, but we added a 5 dB attenuator to make the gain match that of the connectorized receiver. The measured gain response shows good agreement in the passband, exhibiting a ~55-dB typical SC21. The module drew ~0.55 A from the 6.5-V supply (~3.6 W). For this measurement, the VNA was used in frequency-offset mode with a fixed IF (100 MHz) to simulate operation within the radar system. The modular Rx response matches well with the connectorized version, and differences in rolloff are attributed to variations in filter response, with negligible impact on radar performance [36].

Loopback testing was also performed, and the radar response is shown in Figure 24. The test was performed by placing a set of attenuators and a fiber optic delay line with a delay of 1.72 µs between the transmitter output and the receiver input. The setup is used to simulate a single target at 850 ft, thus determining the radar impulse response and sensitivity. The total attenuation in the loop was ~90 dB. A Hanning window function was applied to the time-domain data. The radar echoes were detected ~60 dB above noise level with 8 hardware presums and no off-line averages, and the 3-dB width of the main lobe corresponds to ~1.4 cm. The near-range sidelobes were close to -32 dBc, indicating good chirp frequency linearity. The "skirt" of the response is narrower for the modular design, due to the selection of amplifiers with lower phase noise.

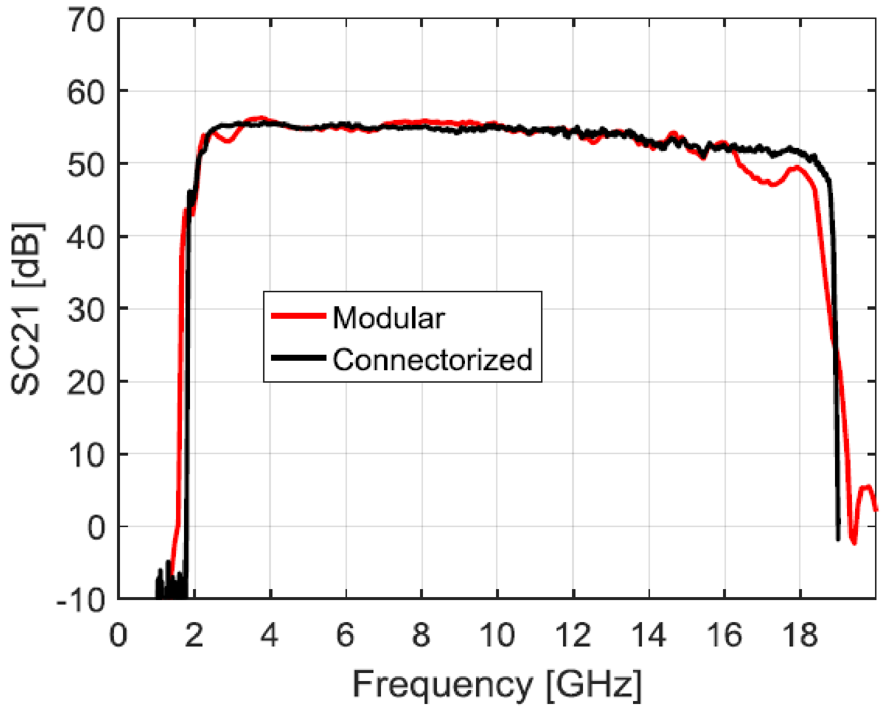

Figure 23: Measured gain of the modular Rx and comparison with its connectorized counterpart

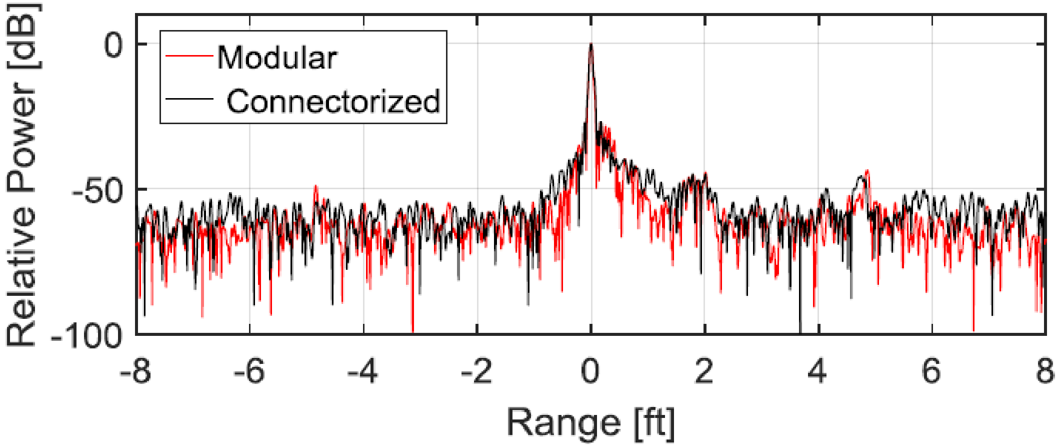

Figure 24: Loopback tested response of the radar using the connectorized system and the modular RF subsystems

Figure 25 shows a processed radar image from the 2018 NASA Operation IceBridge field season. The measurements were recorded at 1,500 ft AGL and span a 5-km flight segment. The modular system has been field-operated and verified to successfully generate detection data while reducing the size and weight of the radar's RF front end.

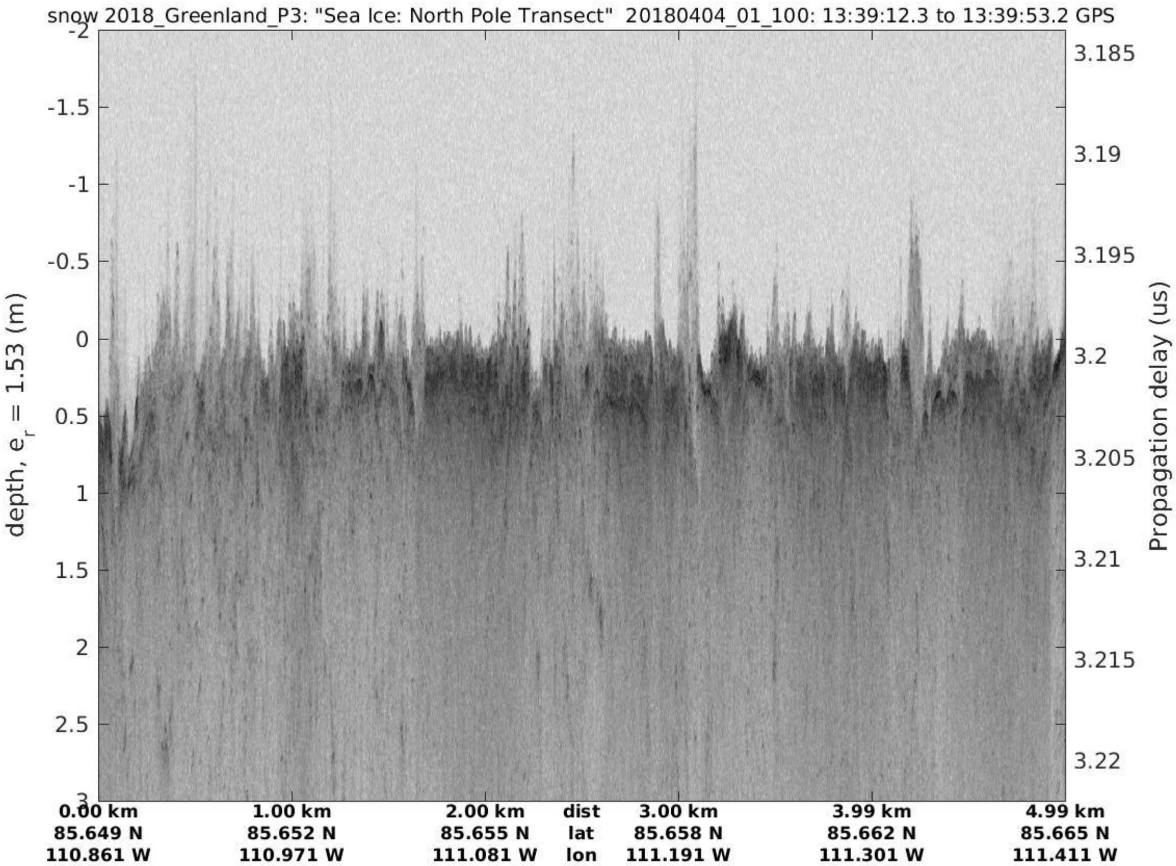

Figure 25: Processed echogram from measurements taken in 2018 Arctic OIB field season using Snow Radar with modular RF subsystems

4: 18 GHz Low Pass Filter

4.1 Design Requirements and Goals

The RF low pass filters used initially in the University of Kansas' 2-18 GHz Snow Radar were a COTS component from Microwave Circuits (L18G20G1) [27]. Subsequent upgrades included custom designs using a Suspended Substrate Stripline topology, first with an aluminum housing [38] [39] and then fully embedded into a PCB [40]. While these filters meet all performance criteria for the radar system, the fabrication requires building cavities, resulting in an overall height (2.16 mm for the SISL filter) that is large in comparison to typical dies (*e.g.*, 0.1 mm for the HMC463, TGA2526, or TGA2214). This created a major bottleneck for the reduction in size to the overall RF subsystems.

To design an adequate replacement, we had to meet several requirements: First, the performance of the previous filters from DC-18 GHz and out-of-band rejection was to be retained. Hence, we desire better than 10-dB input return loss across the pass band, less than 1.5-dB insertion loss, and better than 40-dB out-of-band rejection. Secondly, as we move toward MCM RF subsystems, we require a low-profile planar design of the filter system, preferably with no bottom-layer features and thickness less than 0.3 mm, as the filters will be mounted to the module directly for grounding. Third, we desire a reduction in size, which is aided by meeting the second requirement, as we no longer require an enclosure or built-in cavities, but further reductions are also possible if we make a proper selection of material and design topology.

4.2 Design Overview

The low pass filter designed here is a 9th order Chebyshev toppology designed on a multilayer Liquid Crystal Polymer (LCP) stackup. Due to the wide bandwidth required and the GHzmagnitude frequency of operation, a fully distributed design is required. Our initial design was based on a low-pass filter designed by Almorqi *et al.* [51] [52]. These papers provided limited detail on design methodology on both LCP and Rogers 6002 substrates. Here, we used classical techniques to build and verify the design independently, thereby providing a more detailed design flow and methodology from the ground up, which could serve as a reference for future implementations while being adaptable to various kinds of substrate materials and stack-up configurations.

4.2.1 Substrate Material selection

With miniaturization and weight reduction as a major factor for the design, selection of a suitable substrate material was a vital first step to designing the new filter. Although distributed low pass filters have been designed for multi-GHz frequencies and bandwidths for years, using alumina and ceramic materials, PTFE-based and composite laminates, low-cost FR4, etc, LCP laminates are a relatively new and infrequently-used induction to the RF design landscape [44] [45]. For high frequency applications, a low dielectric permittivity is preferred, with two-fold benefits – a reduction in parasitic capacitances between structures and a reduced size. Additionally, much of the size of a distributed microstrip component (*e.g.*, a filter) can be directly estimated from its overall 50-ohm microstrip width, which is in turn dictated by the ratio of its width W to its height h from the ground plane, W/h. The W/h ratio is determined by closed form equations relying upon the dielectric properties of the material, specifically ϵ_r, but as the height of the substrate is reduced, so is the width.

Hence, we desire a material with both a low dielectric constant and available substrates with smaller height profiles. This led to the initial selection of the Rogers Ultralam 3850 Liquid Crystal Polymer substrate. Comparable LCP substrate materials have been widely used for UWB filters in recent years. Table 1 in Section 1.1 may be referenced for an overview of recent literature related to LCP filters..

Our filter design proceeded in the early stages with the Rogers Ultralam 3850 material and bondply stackup, but we encountered some challenges toward fabrication, which resulted in several changes. First, upon contact for submission and fabrication of the original design with a 4-2-1 mils stack up using Ultralam 3850, it was determined that the material was no longer in production by Rogers. A Panasonic material stackup of 4-1-3 mils in use by Radar Consortium members at Michigan State University (MSU) was identified as a potential option, but limitations in the implementation of via holes at the time ultimately led to settling upon a commercial material and PCB manufacturing solution. Thus, the Panasonic Felios LCP material was selected, using commercially-available 1- and 4-mil thick RF705S LCP and the R-BM17 1-mil bondply. The material stack-up is shown in Figure 26.

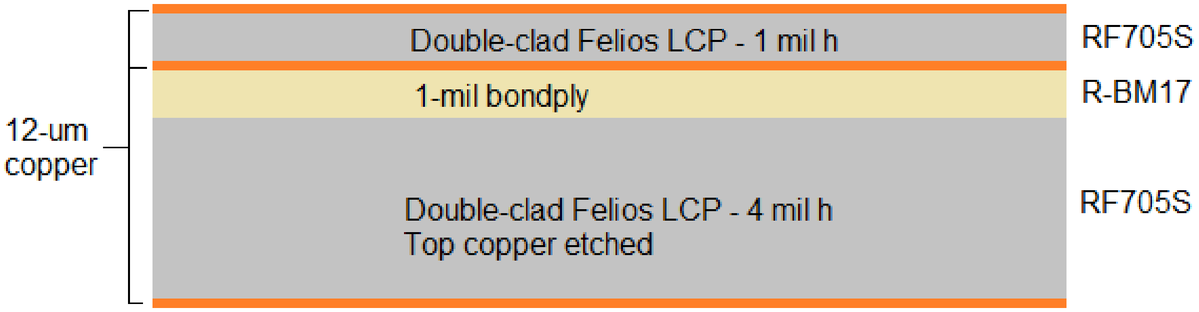

Figure 26: LCP Material stackup for filter design

Due to the deviation in material properties from the Ultralam material originally selected, this necessitated new electromagnetic simulations and parametric sweeps for the filter design, but with the previous groundwork laid for initializing the design and a layout already completed via optimizations and sensitivity analyses, the change in LCP substrate was accounted for with relative ease. Much of the foundational work was recalculated using the newly selected material, and the following sections only refers to the most recent design work including the Felios LCP material.

4.2.2 Generalized Chebyshev LPF Topology

The design of the lowpass filter can be approached using classical techniques, as described in the literature [62]. The following steps may be used:

1) Select a desired response and order (*e.g.*, Chebyshev, Elliptical, etc.)
2) Determine element values of a prototype filter with g_0 = 1 and Ω_c = 1.0
3) Transform the element values g using the desired filter cutoff frequency and source impedance
4) Realize the lumped-component filter with microstrip components that approximate the lumped elements.

The source and load impedance are 50 Ω, and our desired cutoff frequency is 20 GHz. Note that 20 GHz here is selected due to expectation that the passband may shrink as distributed elements are used in place of idealized components, and extension of the passband may also facilitate improved system performance. Additionally, inclusion of a guard band permits operating in a range of frequencies for which the group delay is relatively constant, maximizing chirp linearity.

Selecting an odd network degree, *n,* allows for a degree of network simplification and is desirable for a doubly-terminated filter with source and load impedances $R_s = R_L = 50\,\Omega$. S. Alseyab [63] presented a generalized ladder prototype using series inductors and shunt capacitive resonators that satisfies a Chebyshev insertion-loss response

$$IL = 1 + \epsilon^2 \cosh^2 \left\{ (N-3) \cosh^{-1} \left[\omega \left(\frac{w_0^2 - 1}{\omega_0^2 - \omega^2} \right)^{\frac{1}{2}} \right] + 3 \cosh^{-1} \omega \right\} \tag{8}$$

Here, the transmission zeros are at $\omega = \pm\omega_0$ with order *(n-3)*, and three at infinity. We can specify a passband minimum return loss of $RL_{min} = 20dB$. Assuming the filter is lossless, we can use this to determine

$$S_{11} = 10^{\frac{-20}{10}} = 0.01 \rightarrow S_{21} = 1 - S_{11} = 0.99 \tag{9}$$

$$dB(S_{21}) = 10 \log_{10} 0.99 = -0.044 \tag{10}$$

This result is the maximum pass band ripple associated with the specified input return loss.

From [62], we have the requisite filter degree needed for the Chebyshev filter specified by

$$n \geq \frac{\cosh^{-1} \sqrt{\frac{10^{0.1L_{As}} - 1}{10^{0.1L_{Ar}} - 1}}}{\cosh^{-1} \Omega_s} \tag{11}$$

Where $L_{As}$is minimum attenuation in the stopband, L_{Ar} is the passband ripple, and Ω_s is the frequency at which L_{As} is specified in the normalized frequency variable. Specifying design parameters $L_{As} = 50\ dB$ at $\Omega_s = 2$, and knowing $L_{Ar} = 0.044\ dB$, we see $n \geq 6.64$. Selecting a filter of degree n = 9 will exceed the specified performance while maintaining a small profile.

From [63], the prototype element values for the generalized filter are given for n=9, RL ≥ 20 dB, and stopband insertion loss I.L. ≥ 50 dB. These element values are shown here in Table 2.

Table 2: Chebyshev Prototype Element Values (N=9, RL>20dB, IL>50dB)

Prototype Element	**Value (Ω)**	**Prototype Element**	**Value (Ω)**
C1 = C9	1.03487	L4=L6	1.07413
C3 = C7	1.19263	L3 = L7	0.476885
C5	1.32834	L5	0.428164
L2 = L8	1.12352		

We can scale the frequency and impedance of the prototype filter elements by transforming the inductors and capacitors

$$L \rightarrow \frac{Z_0}{\omega_c} L \; ; \;\; C \rightarrow \frac{1}{Z_0 \omega_c} C \tag{12}$$

Here, ω_c is the desired cutoff frequency in radians per second and Z_0 is the system impedance. Hence, we achieve the scaled element values shown in Table 3. These values are close to the transformed capacitances and inductances reported by Shaman *et al.* [51], as the filter order, passband ripple, and desired bandwidth are similar.

Table 3: Lowpass Filter Transformed Lumped Element Values

Element	Value	Element	Value
C1 = C9	0.165 pF	L4=L6	0.427 nH
C3 = C7	0.190 pF	L3 = L7	0.190 nH
C5	0.211 pF	L5	0.170 nH
L2 = L8	0.447 nH		

A capacitance can be calculated for the open circuit stubs by approximating them as a simple parallel plate capacitor with $C = \epsilon A / d$, where $\varepsilon = 2.92\epsilon_0$ and d = 150 µm for our particular case.

An inductor can be approximated by a straight line microstrip given the length l of the line, its width W, and the substrate thickness t [62]:

$$L = 2 \times 10^{-4} l \left[\ln\left(\frac{l}{W+t}\right) + 1.193 + 0.2235 \frac{W+t}{l} \right] K_g \tag{13}$$

K_g is a correction factor for the effect of the ground plane and is approximated by:

$$K_g = 0.57 - 0.145 \ln\left(\frac{W}{h}\right) \; ; \frac{W}{h} > 0.05 \tag{14}$$

The values from Table 3 are translated via the parallel-plate capacitor and inductor equations. The lengths and widths of these components are both available as design variables. Solving for the capacitance area *A* is straightforward, and Equation 13 can be solved iteratively for length-width pairs using spreadsheet software. Table 4 shows the selected lengths and widths for the inductors and capacitors and their approximated values, using the nominal values determined in Table 3 as a starting point. Figure 27 shows a method of creating the stepped impedances for the ladder topology. The series inductor-capacitor pairs used in the filter can be estimated as a stepped impedance using Equations 13, 14. A thin, high impedance transmission line approximates a series inductor, while the wide, low-impedance plane approximates a parallel plate capacitor.

Table 4: Calculated Distributed Filter Elements

Element	**Length (mm)**	**Width (mm)**	**Value (pF)**	**Element**	**Length (mm)**	**Width (mm)**	**Value (nH)**
C1=C9	1+1	0.3	0.13	L2=L8	1	0.2	0.46
C3=C7	1	1	0.186	L4=L6	1	0.2	0.46
C5	1	1	0.186	L3=L7	0.5	0.2	0.17
				L5	0.5	0.2	0.17

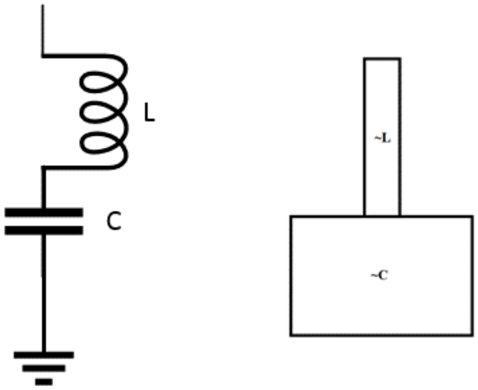

Figure 27: Distributed element approximation of L and C

4.2.3 Synthesis of Microstrip W/h

As the two Felios LCP substrates are bonded together with bondply, the effective dielectric constant must be calculated to accurately account for the effect of the bondply layer. The LCP R-

F705S datasheet [64] states a dielectric constant of 3.0, but the R-BM17 bondply dielectric constant is only provided for the given use-case of a 25-25-25 µm stack up. We can extract an approximate dielectric constant from the provided data by the expression for mixed-media capacitance. As the two LCP substrates are identical, we can reframe the problem as a 50-µm LCP substrate and a 25-µm bondply, as the order of the materials will not change the calculations. A multi-dielectric capacitor can be approximated by two capacitors in series with capacitances $\epsilon_1 A/d$ and $\epsilon_2 A/d_2$, respectively. Their combined capacitance is given by:

$$C = \frac{\epsilon_1 \epsilon_2 A}{\epsilon_2 d_1 + \epsilon_1 d_2} \tag{15}$$

Here, ϵ_1 and ϵ_2 are the relative permittivity of the LCP substrate and the bondply respectively, while d_1 and d_2 are the corresponding thicknesses in the test stack-up (50 and 25 µm). Given TEM wave propagation [62], the relative permittivity is calculated using the capacitances per unit length with free space C_a and with the dielectric C_d:

$$\epsilon_{re} = \frac{C_d}{C_a} \tag{16}$$

The effective dielectric constant ϵ_{re} is given as 2.85 in the R-BM17 datasheet for the 25-25-25 µm test condition. C_a is calculated as an equivalent free-space capacitor $C_a = A/(d_1 + d_2)$. As the area A will be present in both numerator and denominator, it will cancel, and we can substitute known values when substituting the multilayer capacitor expression into the expression for ϵ_{re}:

$$\epsilon_{re} = \frac{C_d}{C_a} = \frac{\epsilon_1 \epsilon_2}{\epsilon_2 d_1 + \epsilon_1 d_2}(d_1 + d_2) \tag{17}$$

Equation 17 can be rewritten to solve for ϵ_2:

$$\epsilon_2 = \frac{\epsilon_{re}\epsilon_1 d_2}{\epsilon_1(d_1 + d_2) - \epsilon_{re} d_1} \tag{18}$$

Therefore, we estimate that the bondply has an effective dielectric constant of ϵ_r = 2.59. We may now calculate the effective dielectric constant of our design substrates using the same equations. As our stack-up consists of 100-µm and 25-µm substrates bonded together with a 25-µm bondply adhesive, we calculate ϵ_{re} = 2.92.

With the effective dielectric constant of our stack-up, we may calculate the requisite width of a microstrip line for a 50-Ω characteristic impedance. Numerous resources are available to achieve such calculation, and the expressions provided by Wheeler [65] and Hammerstad [66] provide better than one percent accuracy. For $W/h \leq 2$:

$$\frac{W}{h} = \frac{8\exp(A)}{\exp(2A) - 2} \tag{19}$$

$$A = \frac{Z_c}{60}\left\{\frac{\epsilon_r + 1}{2}\right\}^{0.5} + \frac{\epsilon_r - 1}{\epsilon_r + 1}\left\{0.23 + \frac{0.11}{\epsilon_r}\right\} \tag{20}$$

Knowing ϵ_r = 2.92 and our desired characteristic impedance Z_c = 50 Ω, we calculate *W/h* = 2.57. With *h* = 150 µm, we calculate a microstrip width of *W* = 385 µm.

4.3 Circuit Simulation via Schematic View in ADS

The schematic view simulation was approached on two fronts: First, a component-only view was created using ideal capacitors and inductors to verify operation of the prototype filter. This was accomplished using the linear circuit simulator of Keysight's Advanced Design System (ADS). Figure 28 shows the schematic view of the filter using lumped, ideal components. This design is used to verify operation of the prototype filter after transformations. Figure 29 shows the performance of the prototype filter as designed in ADS. This allows evaluation of several figures of merit: return loss, insertion loss, cut-off frequency and out-of-band rejection. The simulated S-parameters exhibit a 20-dB input return loss across the band, and a precise cutoff at 20 GHz, as designed.

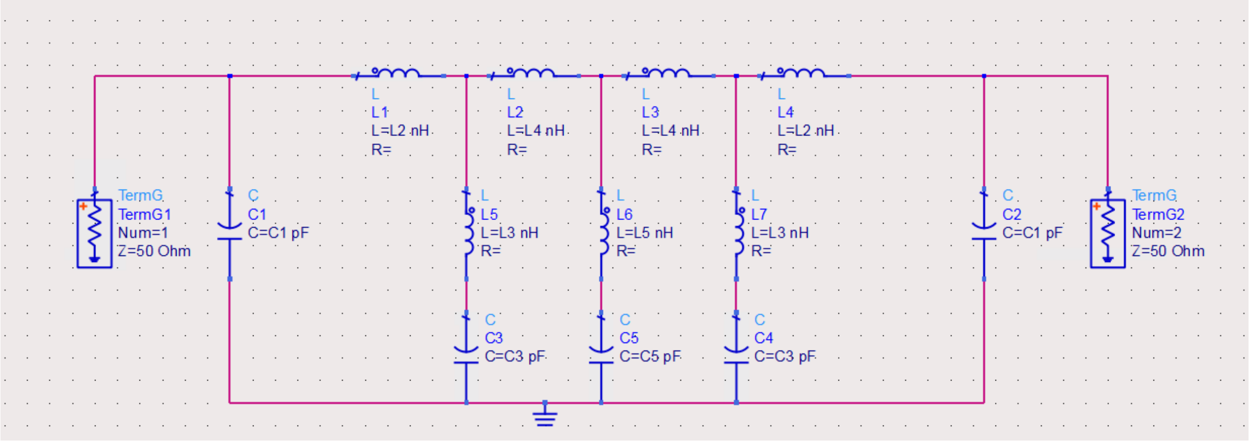

Figure 28: Lumped element LPF schematic in ADS

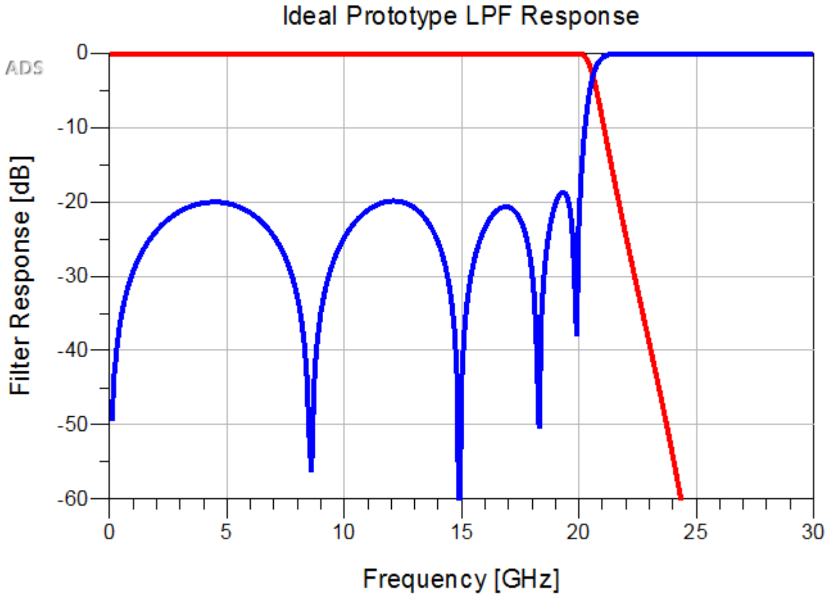

Figure 29: Simulated lumped element LPF response

The second schematic view was created to test circuit model-based components for the implementation of the lowpass filter. This provides a first-order approximation in simulating low-thickness, wideband operation.

Using the widths and lengths approximated in Table 4, the schematic view in Figure 30 was created. This view has been parameterized for quick optimization. Although this component-view design is idealized without effects that would be accounted for by a full electromagnetic simulation, it provides a starting point. The microstrip transmission line performance is approximated by the lengths and widths specified for each model, referencing a substrate model with 150-µm thickness to reflect the design stack-up and ϵ_r of 2.92 as calculated in Section 4.2.3. Figure 31 shows the simulated response of the filter under these conditions.

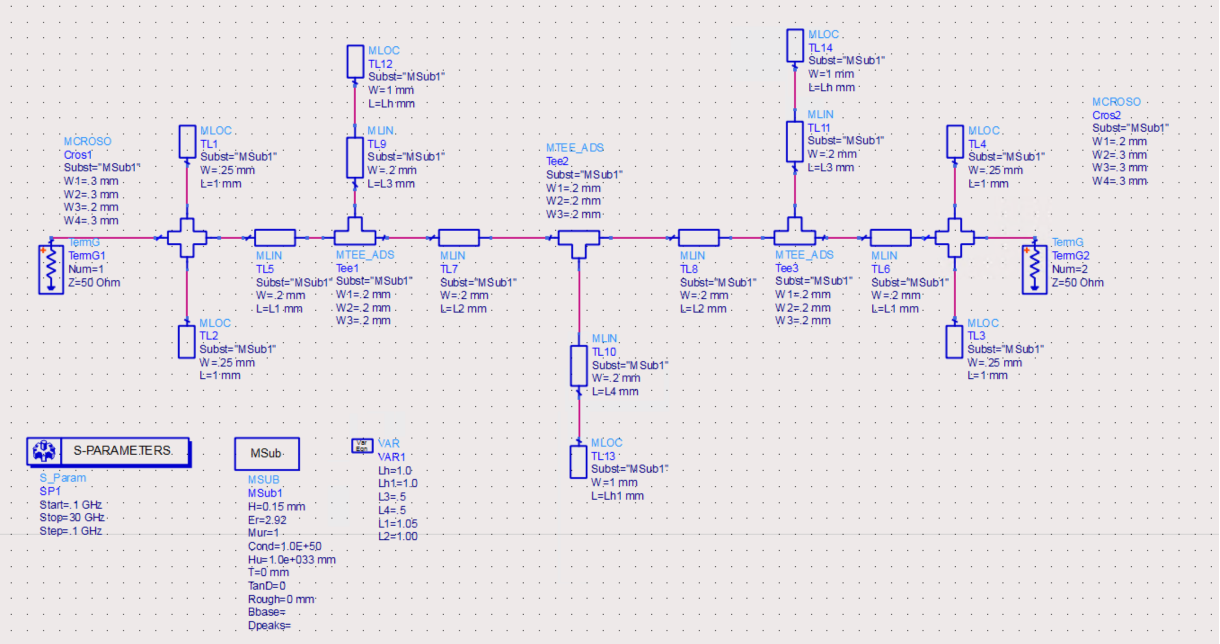

Figure 30: Microstrip model LPF schematic in ADS

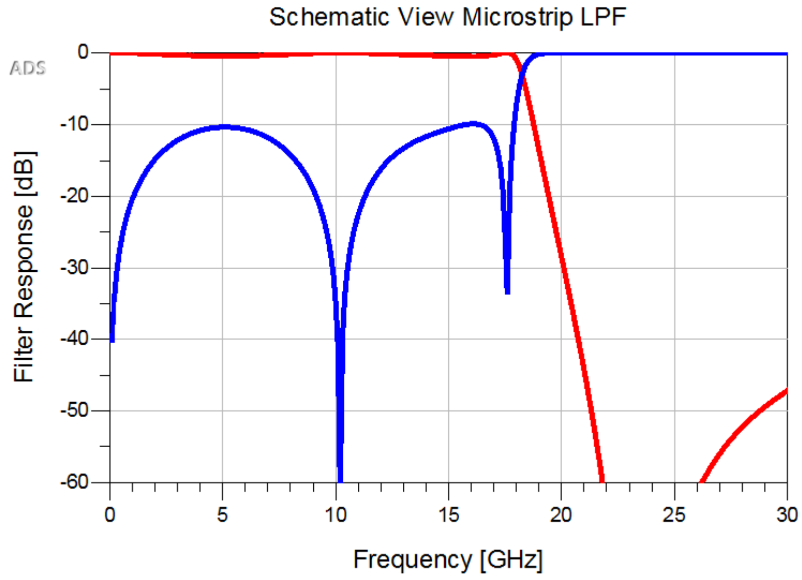

Figure 31: Microstrip model LPF simulated response

This response does not cover the 0-20 GHz bandwidth the prototype was designed for, which illustrates deviations caused by second-order effects not accounted for in the lumped element design. To achieve the designed bandwidth, the schematic was manually tuned on a 0.05-mm scale. The tuned filter response is shown in Figure 32. This simulation shows a maximum in-band insertion loss of 0.255 dB at 5 GHz and a worst-case input return loss of 12.438 dB, and a final S21 peak before roll off at 19.90 GHz. Hence, the bandwidth has been expanded to a 20-GHz cutoff frequency while retaining better than 10-dB input return loss across the band, meeting our stated requirements. Figure 33 details the layout of the filter design, displaying dimensions and indicating the structure of the filter.

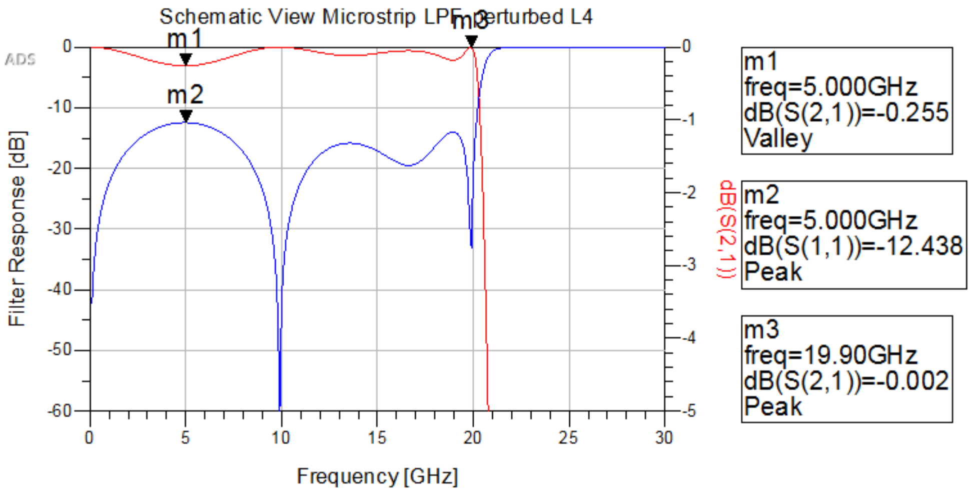

Figure 32: Tuned microstrip model-based LPF simulated response

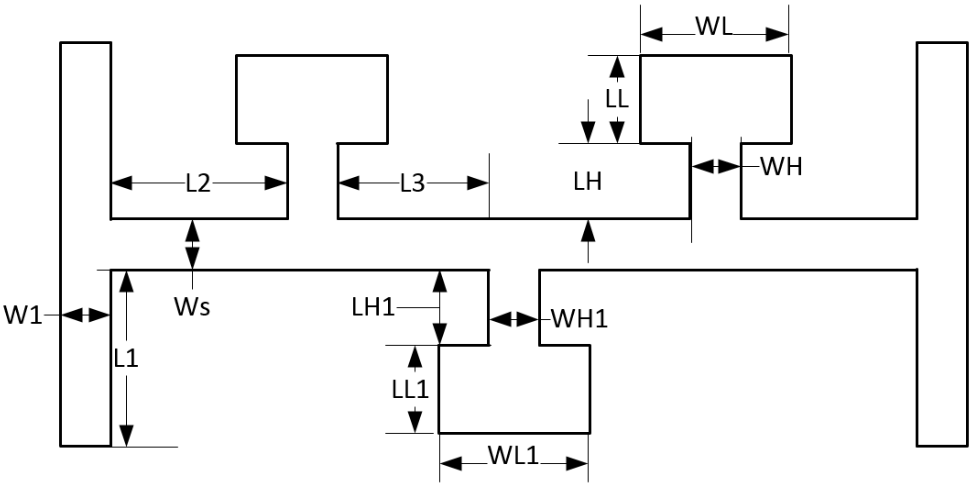

Figure 33: Dimension drawing of LPF dimensions; symmetry is retained for dimensions

Table 5 displays the selected values for the design lengths and widths, obtained from the microstrip schematic simulation.

Table 5: Tuned design dimensions for LPF

Dimension	**Value (mm)**	**Dimension**	**Value (mm)**
LL	0.8	LH	0.5
LL1	0.8	LH1	0.5
L2	1.05	Ws = WH = WH1	0.2
L3	1.0	WL = WL1	1.0

Though these values were determined using a schematic microstrip view, and only tuning the lengths of the structure's features, the sensitivity of the filter to slight changes in lengths of the approximated inductors and capacitor pads was made apparent. For instance, Figure 34 displays the effect on the filter response by sweeping LH1 (tuned as "L4") from 0.4 to 0.6 at 0.02-mm intervals. Through perturbing the design 0.1 mm away from the nominal 0.5-mm value in either direction, the cutoff frequency can shift by as much as 1 GHz. This level of sensitivity to changes in feature lengths is considered for the eventual design of the panelized filter variants detailed in Section 4.5.

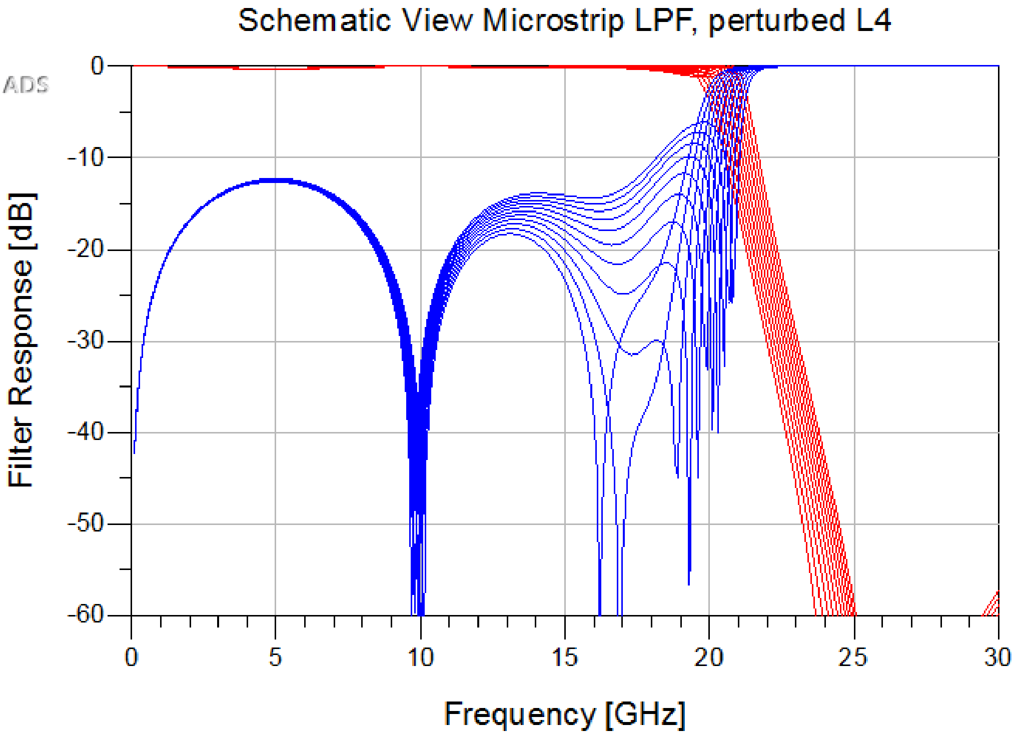

Figure 34: Simulated LPF sensitivity to varying design dimensions (perturbed L4)

4.4 EM-Circuit Co-Simulation and Optimization

The distributed circuit analysis used to obtain a first-order approximation of distributed elements does not account for radiation effects, fringing fields, and other effects that can only be modeled via electromagnetic (EM) simulations. Therefore, EM simulation tools were employed to obtain an optimized design. To proceed with the optimization of the filter design, the geometry settled upon in Section 4.3 was used to create a layout view in ADS. The first-pass EM layout is shown in Figure 35. Input and output microstrip transmission line feeds are added to include the T-line effects that will be present in the final filter design, instead of placing EM ports directly at the first and last capacitive elements. The microstrip feeds have a width of 0.34 mm and are 1 mm in length. The overall dimensions of the filter shown in Figure 35 is 7.2 mm by 2.7 mm. The port reference planes were placed at the end of the transmission line feeds.

As a first pass, this filter does not include the eventual CPW transitions and probe landing sections that will be required for interfacing with the device. It also does not yet have the parameterization that will be used to optimize its features. The simulation was performed using Keysight Momentum, which used frequency-domain Method of Moments (MoM). Since the filter is a planar structure in this case, the computational time using Momentum is significantly faster than comparable EM tools such as Ansys HFSS [67] [68] [69]. Momentum provides sufficient accuracy for planar designs operating all the way to millimeter waves, while providing ease of integration with circuit simulations via ADS's EM-circuit co-simulation framework. Figure 37 shows the Momentum-simulated response of the EM view. Simulations of these geometries take ~30 seconds to generate an adaptive-frequency 50-point sweep within our current computing capabilities. As anticipated, the full electromagnetic simulation lost some of the bandwidth achieved by the component view, reducing the bandwidth of the filter to 18 GHz. The worst-case insertion loss and input return loss have also degraded; the insertion loss reaches a maximum of nearly 0.4 dB, associated with a worst-case in-band input return loss of 10.8 dB, now at 16.56 GHz instead of 5 GHz as simulated in the schematic view.

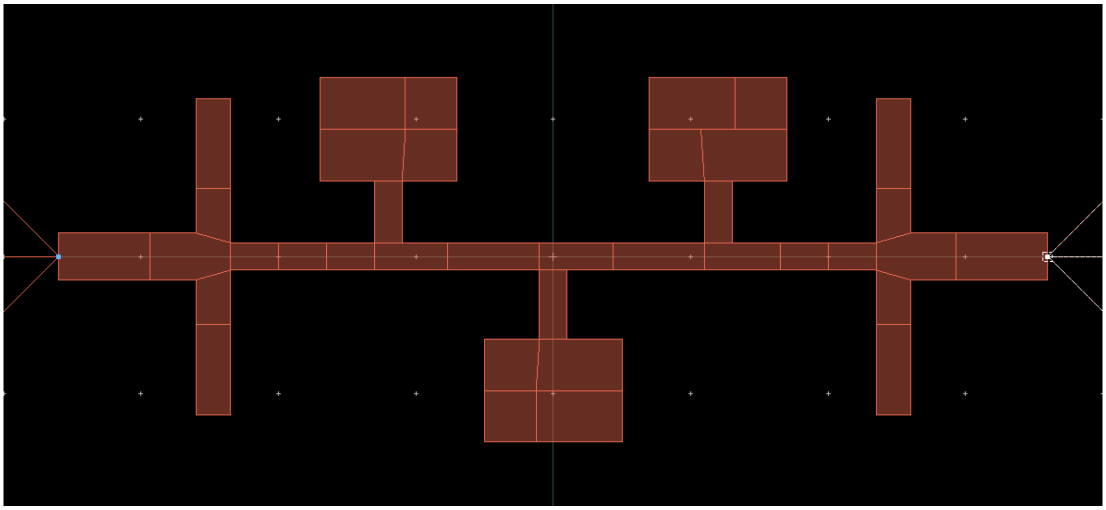

Figure 35: LPF layout in ADS Momentum

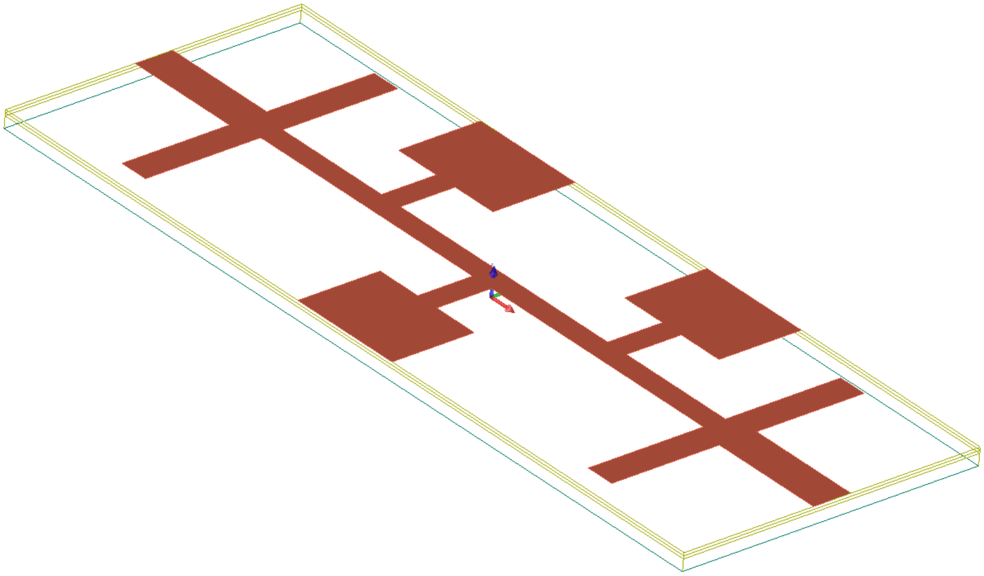

Figure 36: LPF 3D layout view

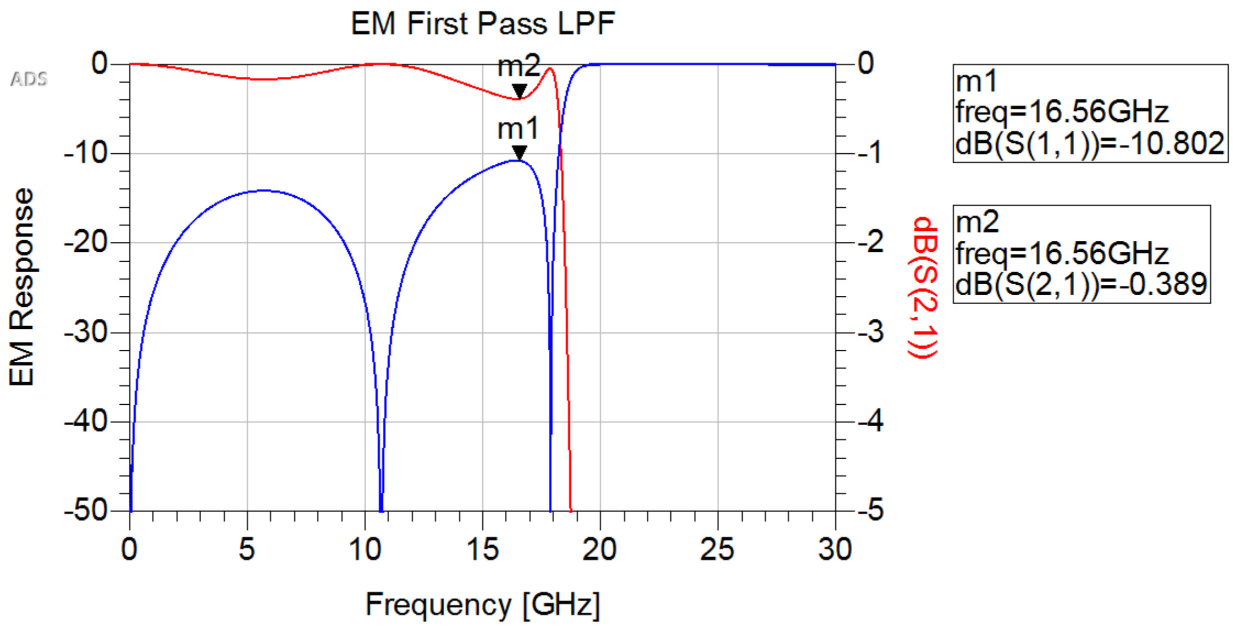

Figure 37: First-pass LPF EM co-simulated response

While the frequency response deviates from that of the schematic view, the EM simulation still meets all requirements stated in Section 4.1. Hence, the design was parameterized using the ADS Co-simulation and EM parameters features. As seen in Section 4.3, shifts as small as 0.1 mm can lead to a shift of 1 GHz in bandwidth. The design was parameterized for lengths L1, L2, L3, and L4 as shown in Figure 38. The parameterized layout was then co-simulated in a schematic view, as shown in Figure 39, and a parameter sweep was performed on the EM layout of the filter. Each of the four parameters were swept over three values, varied 25 microns from the nominal value, providing EM simulated data for 81 total filter variations. The result of the parameter sweep is shown in Figure 40. The dark blue and red traces show the nominal S11 and S21 response of the filter, while the lighter blue and red traces are the responses of the swept responses. Despite the small perturbation of only 25 microns, when varied over four lengths on the filter, the filter cutoff frequency shifts by as much as 0.75 GHz in either direction.

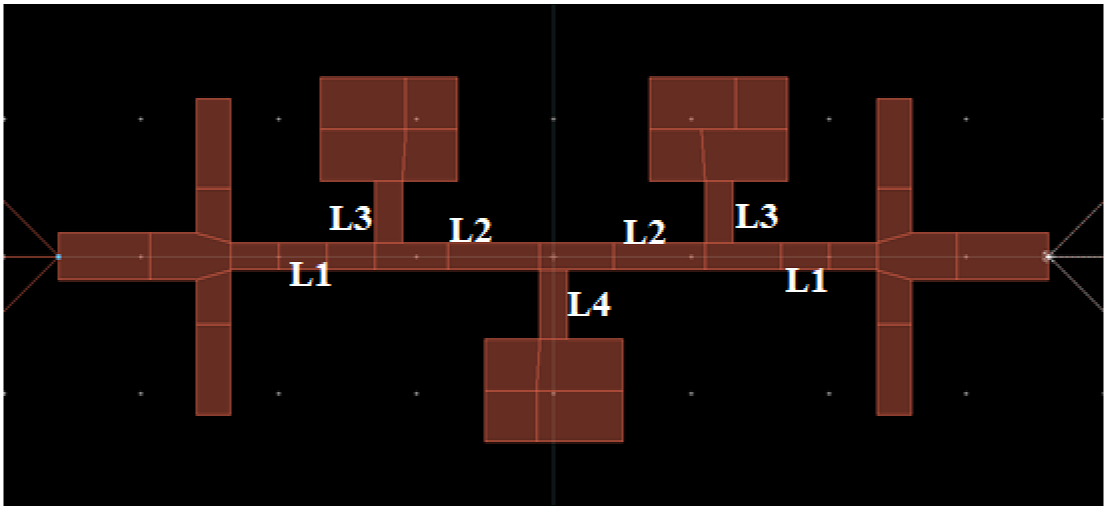

Figure 38: Parameterized LPF layout with variable indicators

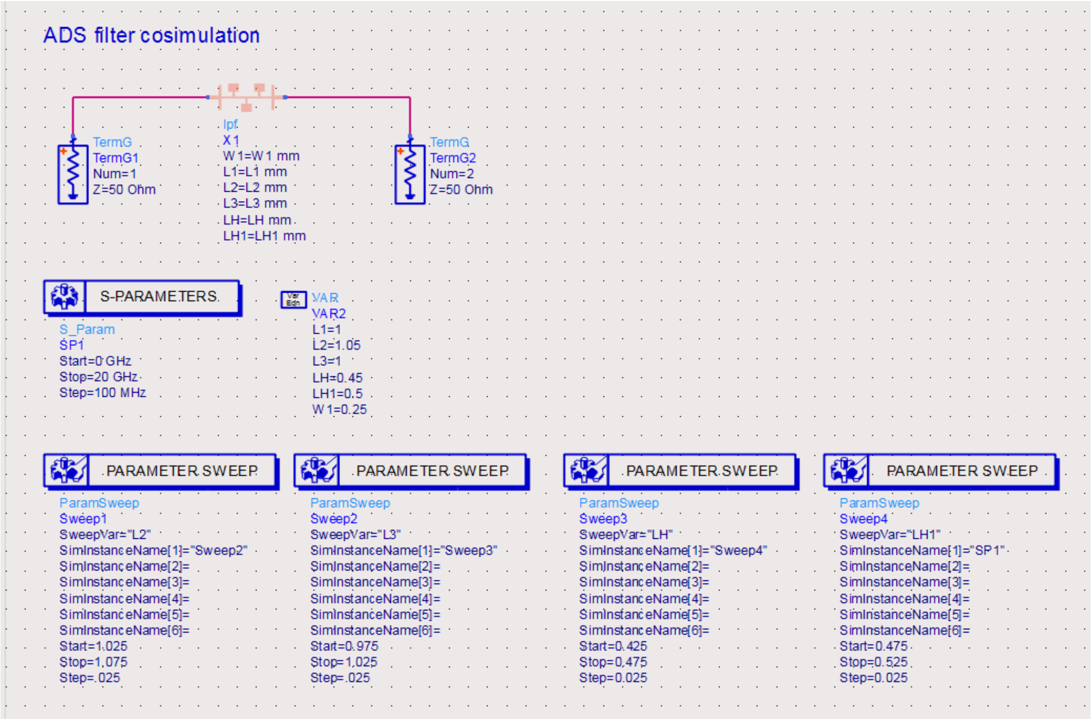

ADS filter cosimulation

lpf
X1
W1=W1 mm
L1=L1 mm
L2=L2 mm
L3=L3 mm
LH=LH mm
LH1=LH1 mm

TermG
TermG1
Num=1
Z=50 Ohm

TermG
TermG2
Num=2
Z=50 Ohm

S-PARAMETERS
S_Param
SP1
Start=0 GHz
Stop=20 GHz
Step=100 MHz

VAR
VAR2
L1=1
L2=1.05
L3=1
LH=0.45
LH1=0.5
W1=0.25

PARAMETER SWEEP
ParamSweep
Sweep1
SweepVar="L2"
SimInstanceName[1]="Sweep2"
SimInstanceName[2]=
SimInstanceName[3]=
SimInstanceName[4]=
SimInstanceName[5]=
SimInstanceName[6]=
Start=1.025
Stop=1.075
Step=.025

PARAMETER SWEEP
ParamSweep
Sweep2
SweepVar="L3"
SimInstanceName[1]="Sweep3"
SimInstanceName[2]=
SimInstanceName[3]=
SimInstanceName[4]=
SimInstanceName[5]=
SimInstanceName[6]=
Start=0.975
Stop=1.025
Step=.025

PARAMETER SWEEP
ParamSweep
Sweep3
SweepVar="LH"
SimInstanceName[1]="Sweep4"
SimInstanceName[2]=
SimInstanceName[3]=
SimInstanceName[4]=
SimInstanceName[5]=
SimInstanceName[6]=
Start=0.425
Stop=0.475
Step=0.025

PARAMETER SWEEP
ParamSweep
Sweep4
SweepVar="LH1"
SimInstanceName[1]="SP1"
SimInstanceName[2]=
SimInstanceName[3]=
SimInstanceName[4]=
SimInstanceName[5]=
SimInstanceName[6]=
Start=0.475
Stop=0.525
Step=0.025

Figure 39: LPF co-simulation workspace in ADS

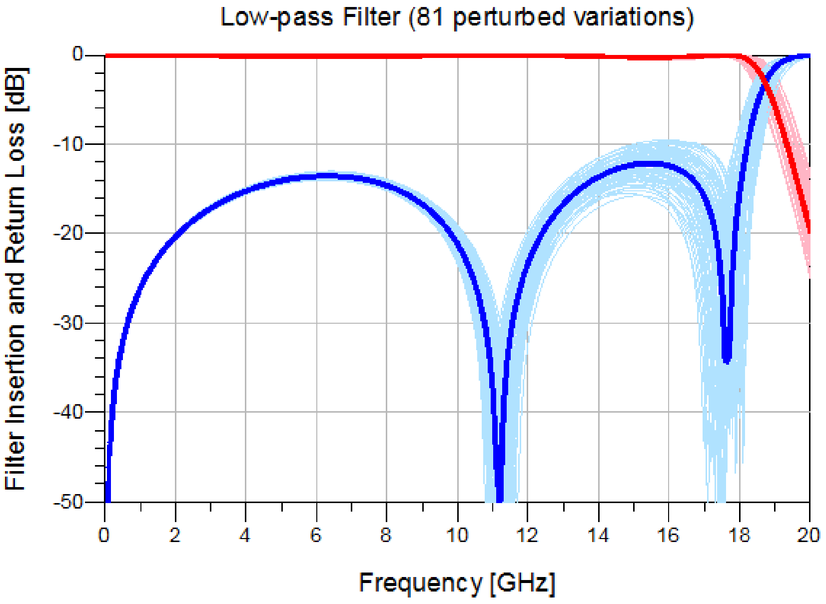

Figure 40: LPF co-simulated parameter sweep simulated results in ADS

The variability in performance based on small parameter shifts led to the eventual inclusion of multiple variations of the LPF filter design on the panel created for manufacture.

4.4.1 CPW-G Probe Considerations and Design

The EPS150RF probe station, available for the eventual measurement of RF components and devices procured for the Snow Radar project, was set up to interface with an HP 8722C VNA for measurements, through the use of |Z| GSG 250-micron pitch probes (Z40-X-GSG-250). To properly accommodate the probes, and to also provide a ground-signal-ground (GSG) connection to the low pass filters for eventual inclusion in a multi-chip module, the design of each varied filter was modified to include a coplanar waveguide with ground (CPW-G) to microstrip transition and a GSG probe landing area.

The CPW-G transmission line features can be determined through equations described by Wadell [70], and numerous calculators are available based on these equations.

After several iterations, a compact transition and landing area was designed for the LCP stackup of the filters. The design requires a trade-off between a desired 50-ohm transmission line and manufacturability. Figure 41(a) shows the original design, while Figure 41(b) shows the final design, which was created to accommodate the needs of the PCB manufacturer—specifically, the trace/space requirements of the manufacturer and the minimum via size informed the final design of the transition area. Due to the necessary trace/space minimum values provided by the fabrication house, a minimum spacing of 70 microns was selected, and to retain ease of probing, a 50-μm excess of copper was included toward the signal trace on the sides of the probes' ground pins. This allows for a 260-micron trace width, with the aforementioned 70-μm gap, resulting in a 55-ohm transmission line section. Although an imperfect match, the associated return loss of a 50-ohm source terminated in a 55-ohm load is better than 27 dB, and the effect of the mismatch is minimized further by transitioning to a 50-Ω microstrip after the 400-μm (less than $\lambda/60$ at 20 GHz) landing and transition area.

The CPW-G transition layout was EM simulated using ADS Momentum, using 50-Ω ports at the end of the traces for CPW-G and microstrip, and referencing the CPW port to ground pins connected to the landing position for the ground pins on the probe, separated by 250 μm. The response of the final transition is displayed in Figure 42. The insertion loss due to the transition itself remains better than 0.1 dB beyond 30 GHz, and the input return loss is better than 23 dB at 25 GHz.

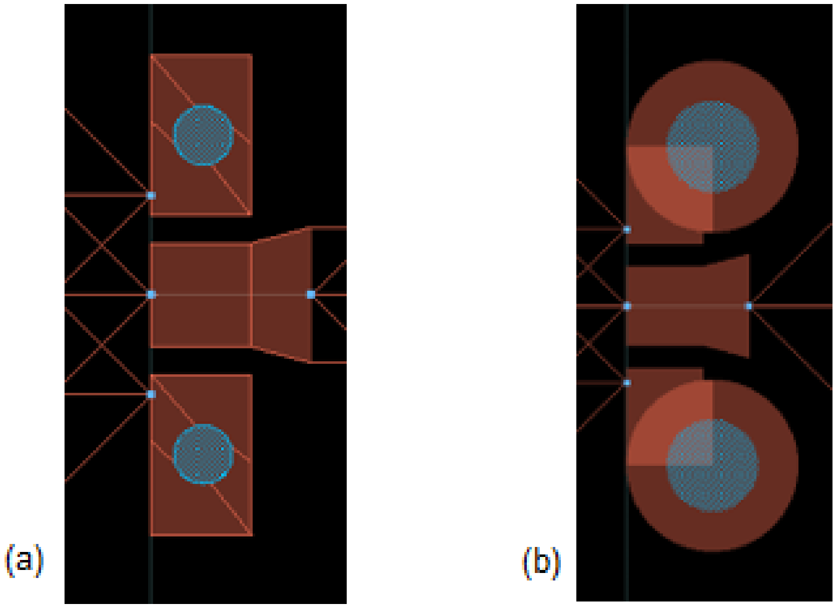

Figure 41: ADS layout for probe landing and CPW-ustrip transition. (a) Original (b) Updated

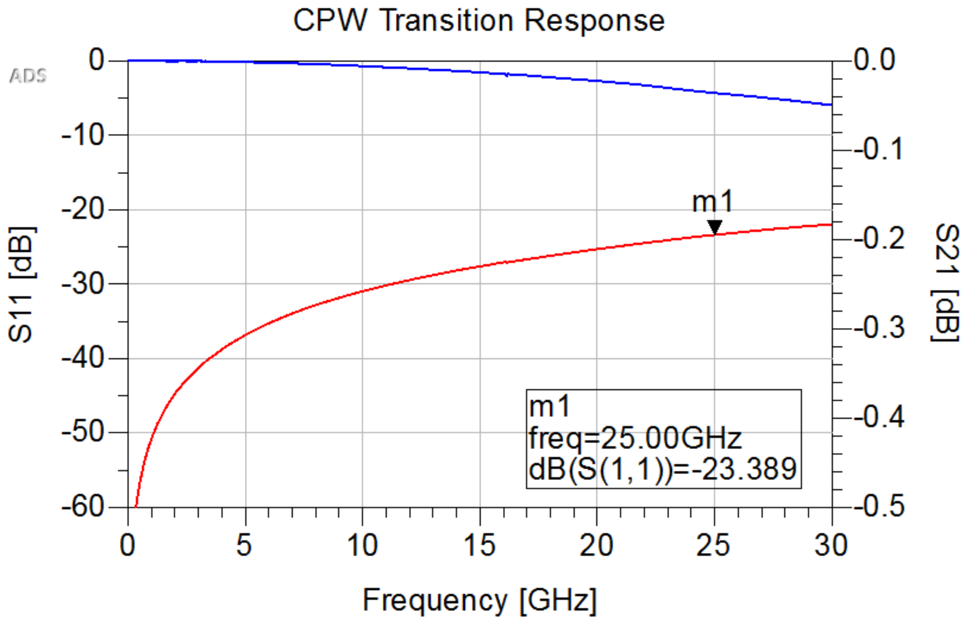

Figure 42: Simulated transition response

To finalize the filter design, the probe landing and CPW-G transition was included in a full EM simulation, including parameter sweeps. Layout view of the filters, including the transition, is shown in Figure 43. The overall filter is standardized (in conjunction with the band-pass filters) to a square shape footprint, with a size of one square centimeter. Because the length of filter elements for variants can lengthen or shorten the overall filter length, the parameterization accommodates by shortening or lengthening the microstrip feed between the transition and the far-side capacitive elements. Thus, each filter variant retains a 1-sqcm footprint, while the internal microstrip lines adjust slightly for changes in length.

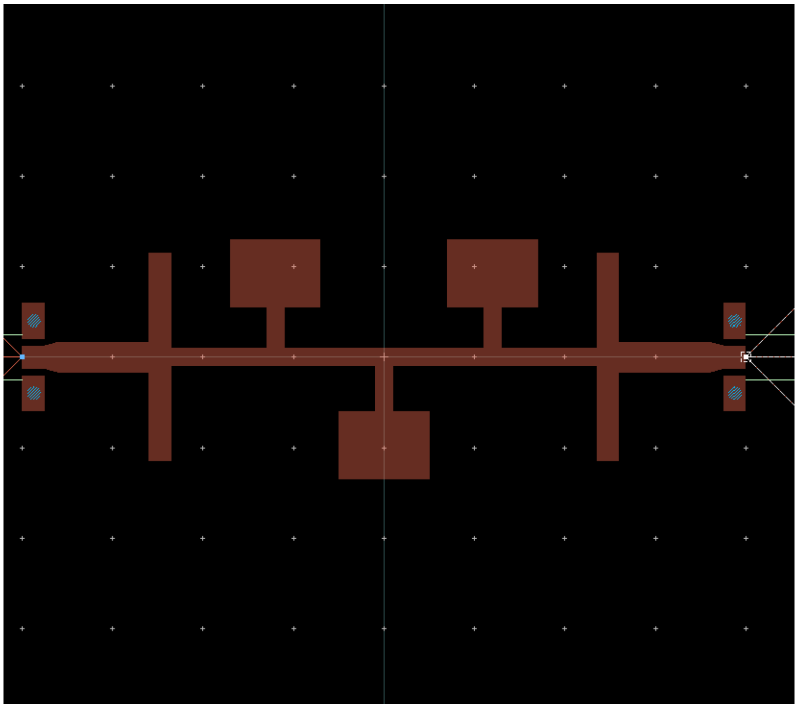

Figure 43: LPF Momentum view with probe transitions

Figure 44 displays the EM-circuit co-simulated response of the swept filter responses. The 18-GHz bandwidth is not appreciably affected by the inclusion of the CPW transitions. The transmission loss for the nominal filter is better than 0.5 dB in the pass band, and the return loss is better than 11.8 dB from 0-18 GHz.

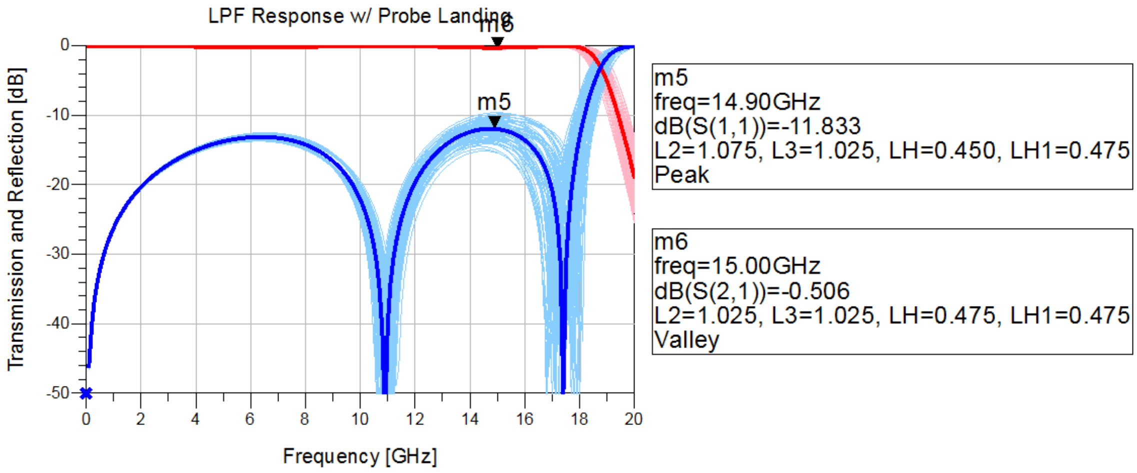

Figure 44: LPF EM-simulated response with probe transitions

4.5 Automated Layout of Design Variants via Scripting

Due to the custom stackup selection, a full panel of filters was the choice of manufacturing method. Hughes Circuits was selected as the PCB fabrication house, through which we obtained a quote for a 5"x8" panel of filters, upon which we would place each design variant for both low-pass and band-pass filters. For panelization, a requisite 8-mm gap was necessary between each board, and with a standardized filter size of 1 sqcm, this left enough room on the panel for 70 filters with a small amount of room to spare for ancillary, non-filter designs.

CADSoft Eagle was used to create the layout artwork for the panel. Initially, one filter was drawn manually as shown in Figure 45, using the polygon tool and manual calculation of the vertices for each corner on the design. This process took too much time (~1.5 hours) to be feasibly repeatable, so a method to automate the artwork generation was developed. Due to the cascading nature of changing a single variable and its effect on the rest of the artwork, manual creation of the design variants was infeasible and prone to design errors.

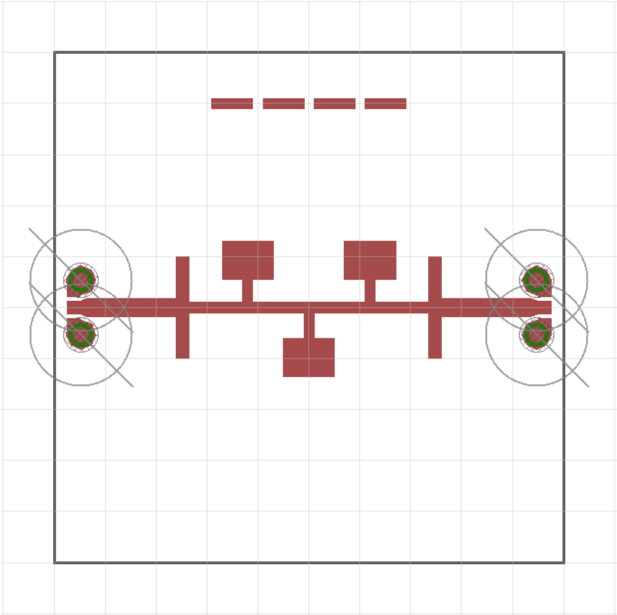

Figure 45: Layout view of a single lowpass filter in CADSoft Eagle

Eagle features an optional command-line interface along with its graphical user interface (GUI). A script file (.scr) can be written in a plain text file using a text editor such as Notepad to load multiple commands in sequence. Because the variations in designs are best considered as perturbation from nominal lengths and widths (*e.g.*, L1), it was determined the most accurate way to approach the issue of panelization was through abstracting the Eagle layout from a higher view of these variables in particular. This was accomplished by writing an Excel document that features the design variations in a readable, modifiable format, then using Matlab to read the Excel document and output a plain-text script that can be run in Eagle.

The custom Matlab script is written specifically for the design of these LCP filter designs. It likewise makes use of the Eagle polygon tool to create the artwork, but through use of read-value variables from the Excel spreadsheet, it automatically adjusts each vertex of the polygon as a calculated value. Additionally, it panelizes the filter variants by using an adjustable reference point for the starting coordinate of each filter. The Matlab code itself is included in its entirety in Appendix A.

Through use of this script, the panel artwork was generated, as shown in Figure 46. The panel includes 35 low-pass filters. The filters were designed with both the CPW transition for use with probing and a microstrip end launch, and the four variables swept in Section 4.4 (L2, L3, Lh, Lh1) were swept instead over two values: nominal and reduced by 25 microns – (that is, $2^4 = 16$ combinations). Thus, the 35 LPF design variations feature 16 unique CPW-launch designs and 16 unique microstrip-launch designs, leaving room for two additional CPW nominal designs and one additional microstrip nominal design.

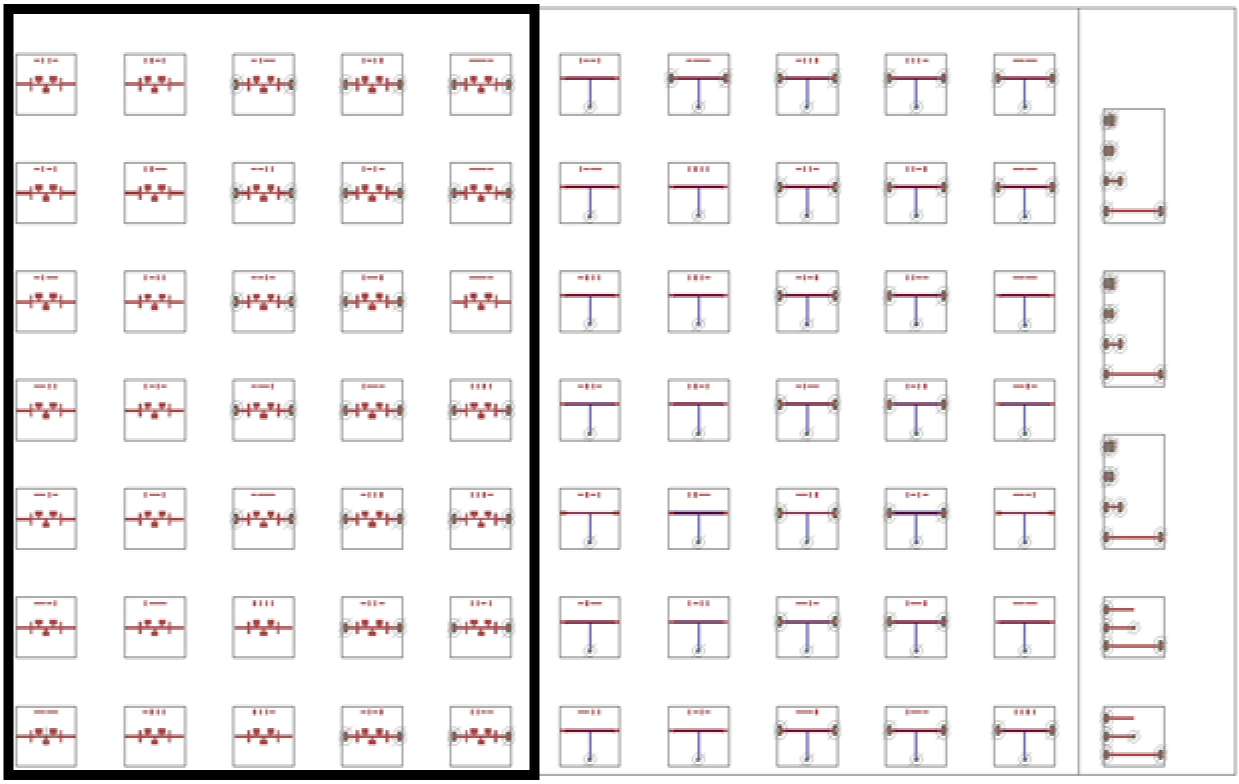

Figure 46: Panelized filter layout (5"x8" useable space); LPFs highlighted

Each filter is also identified by a set of markers, each representing the four variables and their value for the given filter. In particular, the filter displayed in Figure 45 has four horizontal markers, indicating the code "AAAA." The order of the markers is L2, L3, Lh, Lh1. The codes "A" and "B" refer to the nominal value and the 25-micron reduced value for each variable, respectively. Hence, the filters are identifiable as the design variant from these markers.

4.6 Measurements and Results

4.6.1 Panelized LPF Measurements

The panel was manufactured by Hughes Circuits in Spring 2020. At request, the manufacturer was also able to cut the large panel into distinct panels sections for ease of measurement on the probe station, as the station platen was too small to accommodate the full 5"x8" panel. The LPF section of the manufactured panel is shown in Figure 47.

Figure 47: Manufactured panel section featuring 35 LCP lowpass filters

Using the Cascade EPS150RF probe station, the HP 8722C VNA was first calibrated using a WinCal-compatible short-open-load-thru (SOLT) calibration sets. Although LCP custom thru-reflect-line (TRL) calibration sets were also created, calibrating at with the SOLT sets instead retains the effect of the probe transition in the measurement; instead of isolating the response of the filters alone, the probe landings are eventually included in the overall system response upon integration, so including them in the measurement is vital. The filters were characterized in terms of their scattering (S-) parameters and group delay. The S-parameter data were taken for each filter and is shown in Figure 48.

The panelized filters all exhibit better than very close to 10-dB return loss across the passband, and a worst-case 20-dB rejection at 23 GHz. The 3-dB cutoff frequency varies between 17.75 GHz and 19.75 GHz. While variation between filters is expected, these results may indicate some level of measurement error, as the results appear to be split into two groups; examining the S11 responses in Figure 50, the second peak extends below 10 dB return loss near 14 GHz for half of the measured filters, while remaining below 12 dB for the other group. The error is believed to be due to early misalignment and movement of the panel on the station between measurements.

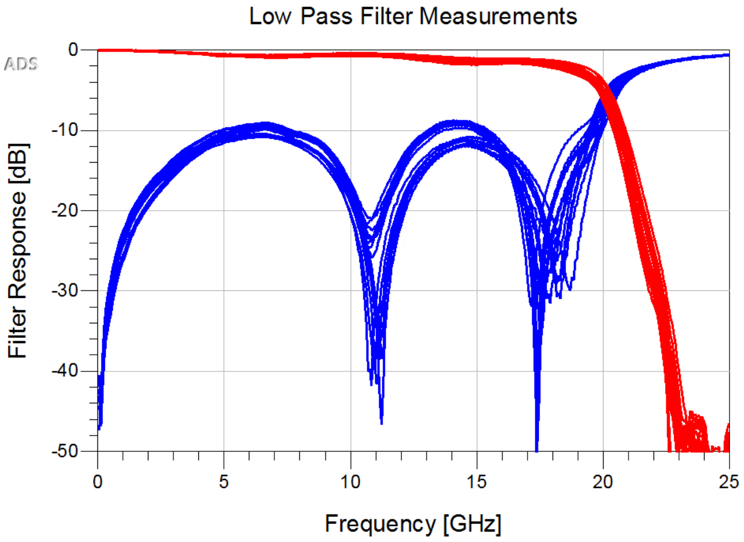

Figure 48: Lowpass filter responses for manufactured filters

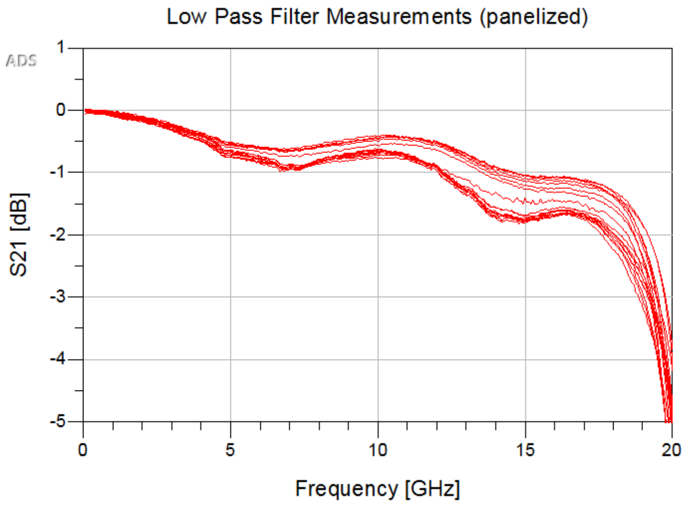

Figure 49: Panelized LPF measurements for manufactured filters (S21)

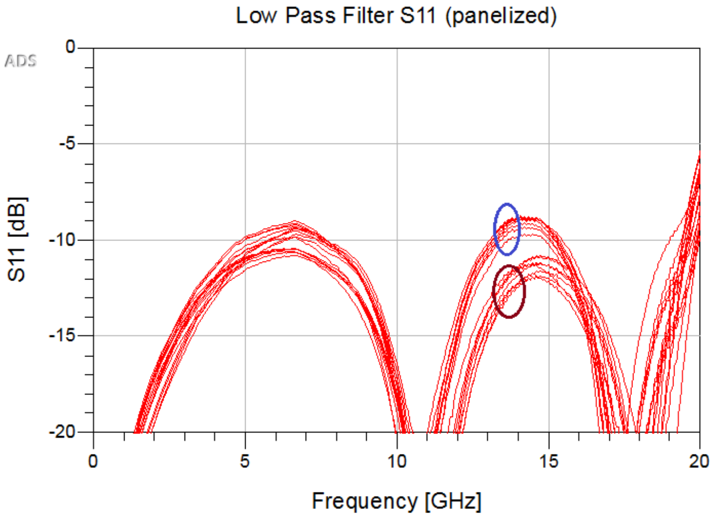

Figure 50: Panelized LPF measured S11 indicating measurement error

4.6.2 Routed LPF Measurements

Over the 2020 summer, Radar Consortium members at the University of Nebraska Lincoln Laser Assisted Nano Engineering group separated the filters individually via laser routing. Figure 51 shows a comparison of the physical size of a single filter and a penny. As designed, the filters measure only 1 sqcm and are fully planar. To compare with the panelized filters, each filter was remeasured. Figure 52 shows a comparison between two “ABBA” filters pre- and post-routing.

Although the upper-band null shifts slightly from 17.8 GHz to 17.9 GHz, this could be explained as slight differences in probing of the filters while taking the measurements. Provided minute changes attributed to testing, the responses are identical.

To indicate the measurement error for several filters as discussed in Section 4.6.1, Figure 53 shows a comparison between the panelized and routed "AABB" filter measurements. The upper passband null is shifted by ~2 GHz, and the routed filter exhibits a minimum in-band return loss of 11 dB, while the panelized filter has a minimum return loss of 9 dB. Due to the size of the panel sections, many of the panelized filter measurements were taken with the devices under test in suboptimal positions such that the panel could not lie perfectly flat on the probe station, while the routed filters were measured in a repeatable process, using the same position on the station. Thus, the routed filter measurements supersede those taken for the panelized filters.

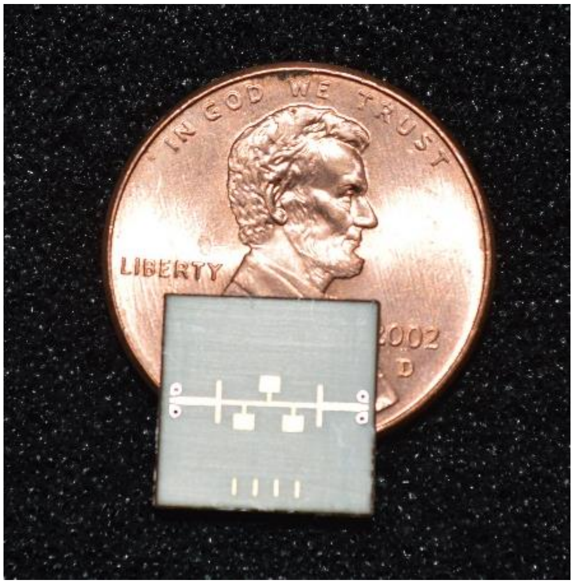

Figure 51: Photograph of routed lowpass filter

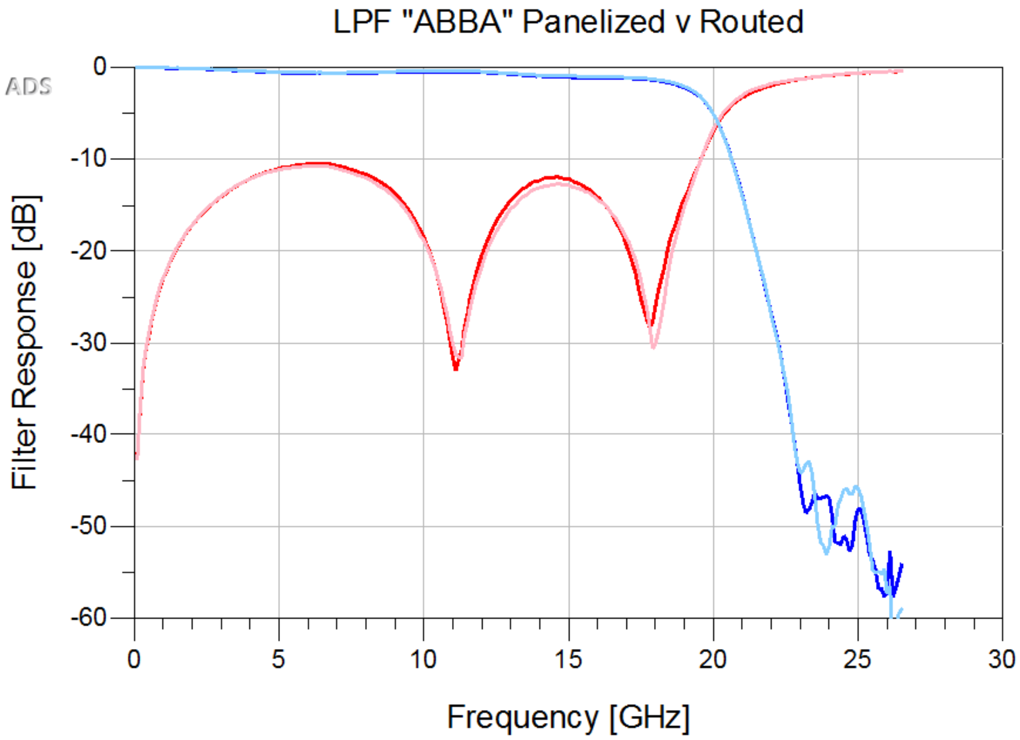

Figure 52: LPF measurement comparison between panelized (dark) and routed (light) (designator "ABBA")

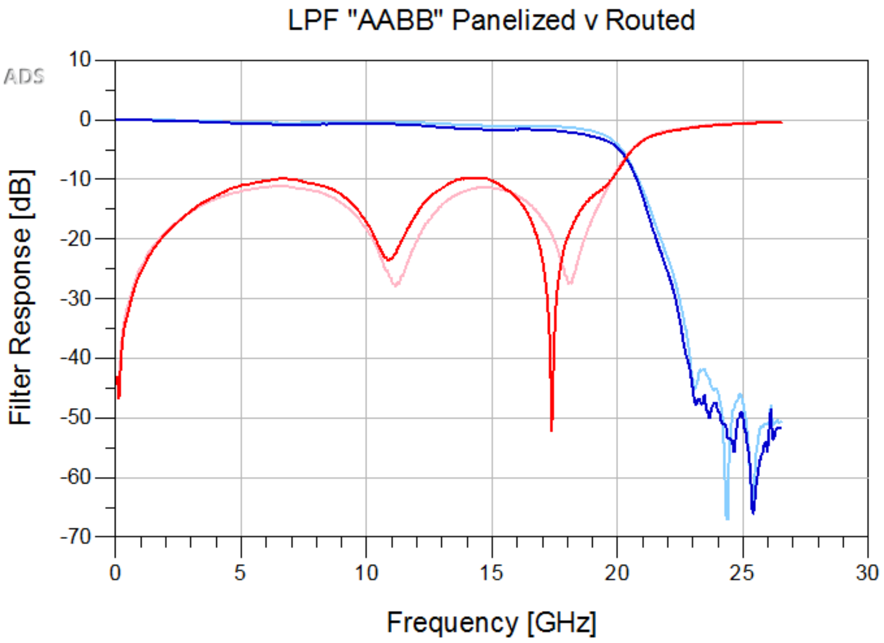

Figure 53: LPF measurement comparison between panelized (dark) and routed (light) filter (designator "AABB")

The S-parameters for the routed filters are shown in Figure 54. The passband transmission response is shown with finer detail in Figure 55. The routed filters exhibit better than 10-dB return loss from DC to 19.3 GHz. The out-of-band rejection is better than 20 dB at 22 GHz and better than 30 dB at 22.5 GHz for all filters. At 10 GHz, the worst-case insertion loss is 0.5 dB. The insertion loss is better than 1 dB for DC-14 GHz and better than 1.4 dB at 18 GHz, and the minimum 3-dB cutoff frequency is 19.4 GHz. All filters exhibitted similar responses, while variation in the upper passband null was expected with element variation. Further discussion of individual filters and corresponding simulation is presented later in this section.

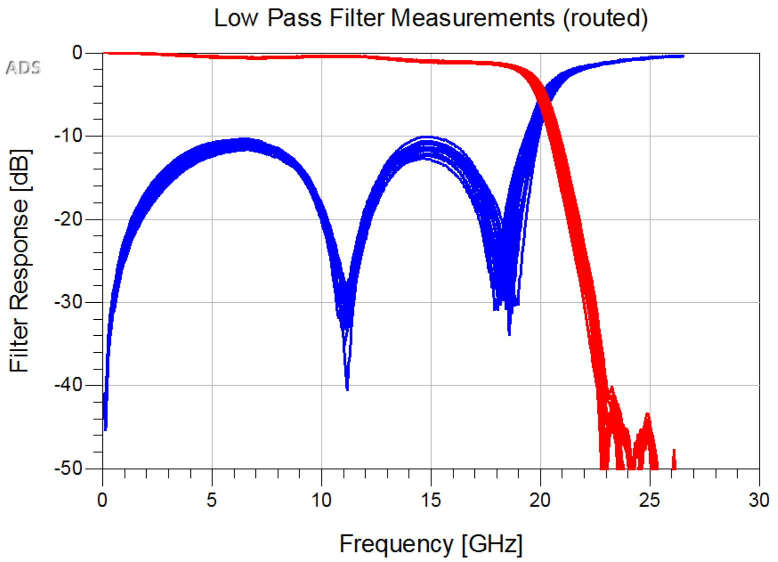

Figure 54: Routed LPF measurements - S parameters

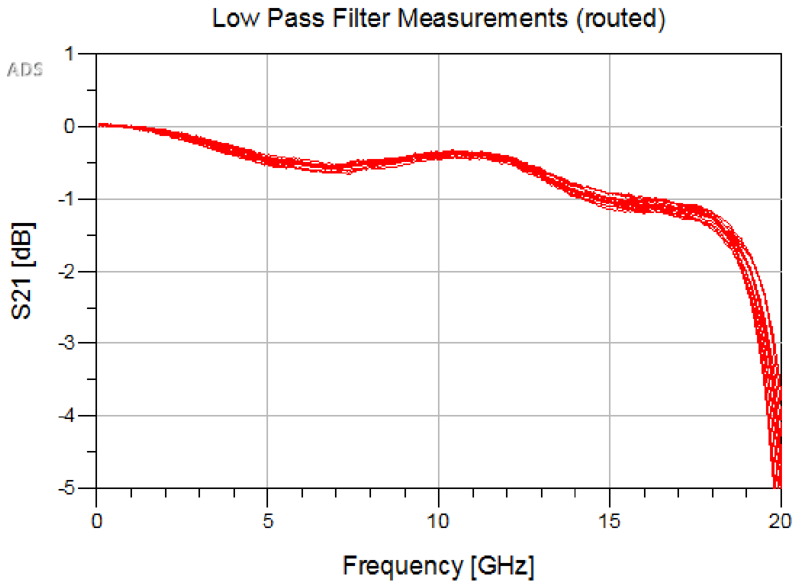

Figure 55: Routed LPF measurements - S21

For UWB operation, besides the in-band insertion and return losses, another relevant figure of merit is the group delay. Group delay can influence radar performance because of potential phase distortion and thus frequency non-linearities, which may affect range sidelobe performance unless corrections are applied. The group delay of the lowpass filters is plotted in Figure 56. The filters show good agreement in group delay across the passband; they exhibit a nearly constant group delay of 70 ps from DC to 13 GHz, reaching 100-ps delay at 16 GHz, and a continued gradual, expected increase toward the band edge, reaching 150 ps at 18 GHz and 200 ps at 19 GHz.

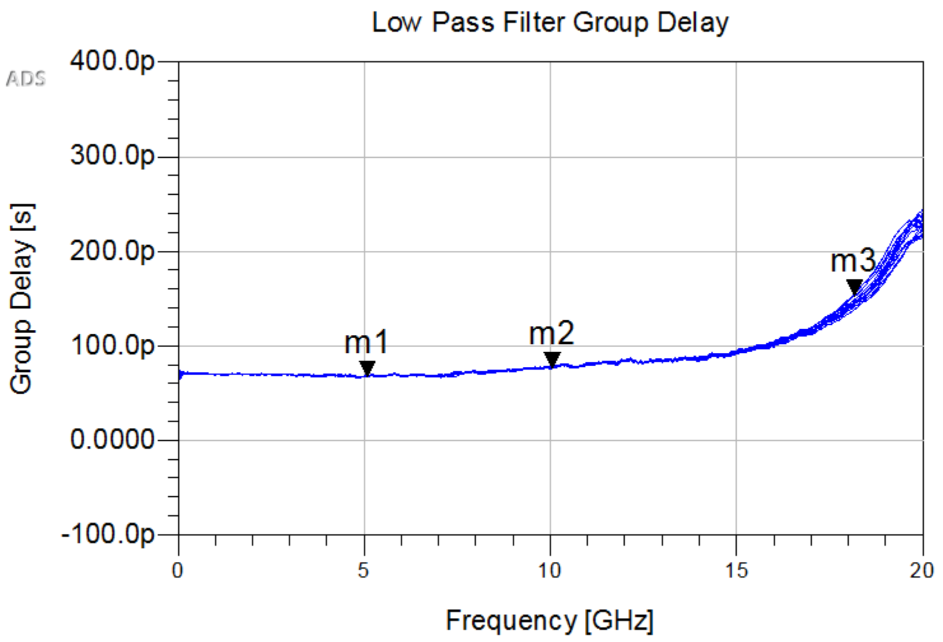

Figure 56: Routed LPF measurements - group delay

Most notable of the results is the shift in all filter responses to a higher cutoff frequency and increased passband attenuation at the upper passband. The increased transmission attenuation is ascribed to conductor and dielectric losses at higher frequencies, unaccounted for by the EM simulation[3]. The extended passband is attributed to be a result of translating the exacted rectangles of the filters in ADS to Eagle and a bias toward larger filter elements when routed by the manufacturer. As each filter in the manufactured set has a tendency toward higher bandwidth, it is believed that both the non-zero width of the outlines defining the polygons in the layout software and imperfect routing of the filter elements resulted in larger elements for every filter in the set. Larger filter elements would result in shorter transmission lines, as the polygons defining the next element after a given transmission line would be encountered sooner.

---

[3] The EM simulation models assumed a constant conductor thickness of 12 μm and no dielectric losses. In practice, the copper is nominally 17 μm thick with an extra Ni/Pd/Au surface finish and the manufacturer's specified loss tangent of the LCP substrate is 0.002.

Figure 57 shows a comparison between the nominal “AAAA” simulated filter and the three manufactured filters with its layout. Comparison indicates small changes in performance due to manufacturing tolerance variation, as each filter has the same design; although the three nominal filters were designed with the exact same layout in Eagle, there are very slight differences in the null placement near the cutoff frequency. The near-identical match between the manufactured filters indicates strong repeatability and hardiness to manufacturing tolerances.

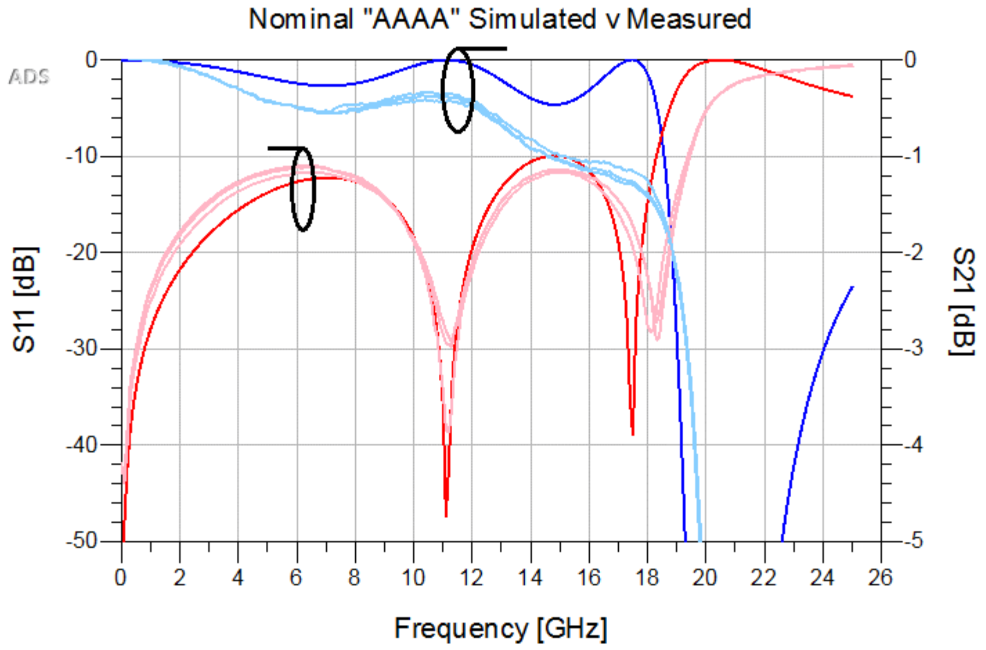

Figure 57: Comparison of simulated (dark) and three manufactured (light) nominal LPFs

The routed filters in Figure 57 exhibit less than 1-dB of transmission loss up to 15 GHz and ~1.4 dB at 18 GHz. They also exhibit a tendency toward a higher 3-dB cutoff frequency – while the simulated filter has 3-dB insertion loss at 19 GHz, the measured filters have the same insertion loss at 19.25 GHz.

The simulated filter that corresponded to the highest bandwidth (from Figure 44) was the filter with the smallest values of L2, L3, LH, and LH1. To further indicate the bias toward larger filter elements, Figure 58 shows a comparison between the simulated and measured S-parameters for the fully-perturbed “BBBB” filter. This filter has each length L2, L3, LH1, and LH2 shortened by 25 µm. Comparing to the close S21 match for the nominal filter shown in Figure 57, the “BBBB” filter indicates a shift toward a higher cutoff frequency than its corresponding simulated results. As all element lengths are shortened, larger element widths (*i.e.*, wider traces and pads) would shorten the lengths further and increase the cutoff frequency; That is to say, a bias toward larger element widths would create a numerical difference in length Δl_{bias} for each filter such that $l_{manu} = l_{design} - \Delta l_{bias}$, and the filter with the shortest designed lengths would be more heavily affected by Δl_{bias} as it would account for a larger difference as a percentage of the total length.

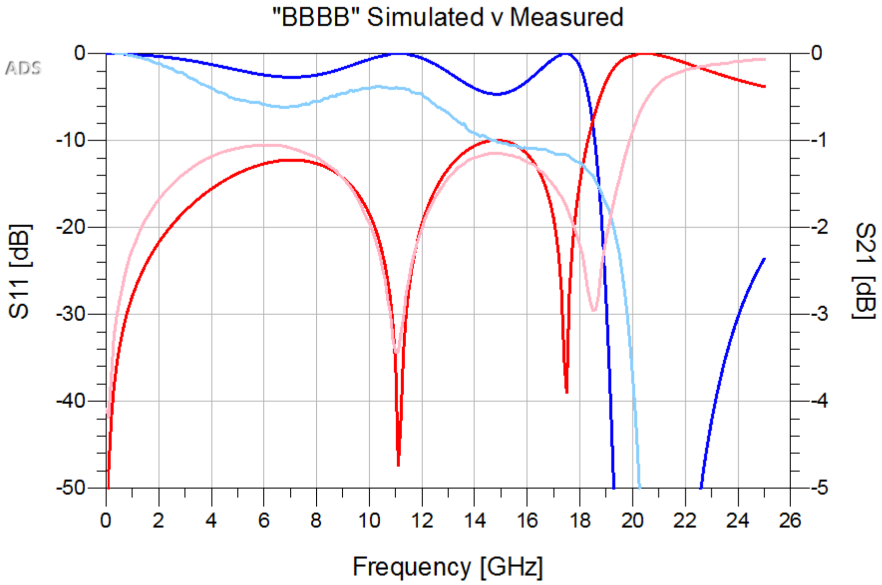

Figure 58: Comparison of simulated (dark) and manufactured (light) filter (designator "BBBB")

5: 2-18 GHz PC-SLR Band Pass Filter

5.1 Design Requirements and Goals

The desired low- and high-frequency cutoffs for the design are designated f_1 and f_2, respectively: $f_1 = 2\ GHz$; $f_2 = 18\ GHz$ Thus, we may calculate the center frequency, f_c, as

$$f_c = \frac{f_1 + f_2}{2} = 10\ GHz \tag{21}$$

The fractional bandwidth FBW of the filter is calculated by

$$FBW = \frac{f_2 - f_1}{f_0} = 160\% \tag{22}$$

Other key requirements for the design include a combined LPF-BPF cascaded length of less than 1.7”, low insertion loss (<1.5 dB), return loss better than 10 dB across the bandwidth, and rejection better than 40 dB at 200 MHz, which is the operating frequency of the VHF radar sounder, a system typically operated on the same flights as this system [20].

A variety of techniques are available for the design of band pass filters, but only a few methods allow achieving very wide bandwidths by means of classical synthesis techniques [71]. As mentioned in Section 4.2, to achieve filter performance up to 18 GHz, lumped components are not viable. Therefore, a distributed filter topology will be necessary. A method for synthesizing parallel-coupled stub loaded resonator (PC-SLR) filters and demonstrated on RT5880 has been detailed by Akra *et al.*, as discussed in [72]. Using SLRs, several wideband BPFs have been realized. A summary of several reported SLR or LCP wideband BPFs can be found in Table 6.

Table 6: Selected reported SLR and LCP wideband BPFs

Reported Filter	Implementation	Substrate	Size	Bandwidth description	Performance notes
PC UWB [73]	E-shaped resonators SLR, 1-layer	ϵ_r=2.65, 0.8 mm	30 x 30 mm	3.75-6.45 GHz	< 2 dB IL across band
Wideband microstrip BPF [74]	Microstrip SLR, 1-layer	FR-4; 1.52mm	59 x 97 mm	74% with 1.92 GHz fc	< 2.5 dB IL @ 1.92 GHz
Compact DSLR [75]	Dual-stub loaded resonator, 1-layer	Unspecified	22.4 x 14.5 mm	2.9-10.9 GHz	<1.5 dB IL across band
Compact LCP UWB BPF [43]	Vialess 5-capacitor multilayer	Rogers 3850 LCP; 800 µm	15.15 x 4.7 mm	3.9-10.1 GHz (3dB)	0.58 dB @ 7.0 GHz
Planar UWB filter [76]	1-layer, microstrip, meandered transformer	Rogers 3850 LCP; 50µm	5 mm x 5 mm	2-18 GHz	2.6 dB IL @ 18 GHz
LCP PC-SLR UWB BPF [50]	Multilayer PC-SLR, SC stub	Rogers 3850 LCP multilayer; 200 µm	8.3 x 5.35 mm	2-18.5 GHz	0.8 dB IL @ 10.5 GHz

Using the SLR synthesis method described in [72], Almorqi *et al.* [50] implemented a 2—18.5 GHz BPF on 200-µm LCP using a PC-SLR topology, achieving a simulated 20-dB return loss across the passband with five return loss poles in the passband. This topology also offers high out-of-band rejection and low in-band insertion loss combined with good in-band return loss, which make them well-suited for our application. This design was therefore used as a starting point for the filter design described in this chapter. We adapted it to match the same material stackup used in the low-pass filter described in Chapter 4.

To lay the foundation for PC-SLR filter design, this chapter will discuss this particular topology from a generalized prototype and show equivalence to the distributed narrow-band filter implementation, detailing how equivalence between the PC-SLR and a low-pass prototype can be achieved. Parallel couplers are also discussed and their equivalent inverter circuits. Next, as the design method is described, issues for wideband operation are discussed and a method is determined for creating a wideband bandpass filter using CAD software. The method was employed to design a PC-SLR bandpass filter, which was manufactured by a commercial board fabrication house (Hughes Circuits) in a panel with many design variations. We describe a series of trade studies completed to ensure first-pass design success. Finally, measured results for the manufactured filters and comparisons with simulations are presented and discussed.

5.2 Generalized Bandpass Filter

The general form of a transformed bandpass filter ladder topology is shown in Figure 59. Beginning with a low-pass prototype filter, we transform the structure of the filter such that each inductive element g_i maps to a series LC resonator L_s and C_s, while each capacitive element g_c maps to a parallel LC resonator L_p and C_p [62]. The lowpass prototype is normalized to $\Omega_c = 1\, rad/s$ and source and load impedances of $1\,\Omega$ (for odd filter order *n*), as was discussed in Chapter 4. To perform the transformation to a bandpass ladder filter, we must assess the center frequency ω_0 and fractional bandwidth FBW of the desired transformation, and map the prototype frequency domain Ω to the angular frequency domain ω:

$$FBW = \frac{\omega_2 - \omega_1}{\omega_0} \tag{23}$$

$$\omega_0 = \sqrt{\omega_1 \omega_2} \tag{24}$$

$$\Omega = \frac{\Omega_c}{FBW}\left(\frac{\omega}{\omega_0} - \frac{\omega_0}{\omega}\right) \tag{25}$$

Here, $\omega_{1,2}$ describe the lower and upper passband edge angular frequencies. To yield the series and parallel reactive component values, $L_{s,p}, C_{s,p}$, we evaluate

$$L_s = \left(\frac{\Omega_\mathrm{c}}{FBW\omega_0}\right)\gamma_0 g \tag{26}$$

$$C_s = \left(\frac{FBW}{\omega_0\Omega_c}\right)\frac{1}{\gamma_0 g} \tag{27}$$

$$C_p = \left(\frac{\Omega_c}{FBW\omega_0}\right)\frac{g}{\gamma_0} \tag{28}$$

$$L_p = \left(\frac{FBW}{\omega_0\Omega_c}\right)\frac{\gamma_0}{g} \tag{29}$$

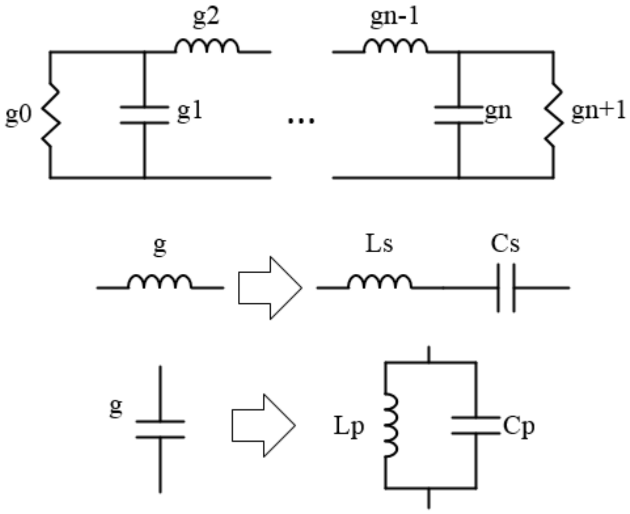

Figure 59: Bandpass transformation of lowpass ladder prototype

By noting the relationship between the series and parallel elements as described in Equations 26-29, we see that

$$\omega_0 = \sqrt{\frac{1}{L_s C_s}} = \sqrt{\frac{1}{L_p C_p}} \tag{30}$$

These describe the resonant angular frequency of the LC resonators, which is equal to the operating center frequency of the filter. Lumped realization of resonators at GHz frequencies is problematic, as many inductors have (in the range of 100s of MHz) a self-resonant frequency (SRF) – or frequency at which the device's inductance and parasitic capacitances are resonant, beyond which the reactance of the capacitance dominates the device's performance. In order to realize a bandpass filter that would operate in the 2-18 GHz range, distributed resonant elements are required.

5.3 Distributed Filter Elements

5.3.1 Stub-Loaded Resonators

A schematic representation of the elementary short-circuited stub-loaded resonator (SLR) is shown in Figure 60. It is described by a transmission line with physical length $2L_{oc}$ characteristic impedance Z_{oc}, loaded by a short-circuited stub at its center, with characteristic impedance Z_{sc} and physical length L_{sc}. The physical lengths can be translated to electrical lengths by $\theta = \beta L$, where $\beta = 2\pi/\lambda$ is the phase constant expressed in radians per meter. As with any microwave 2-port network, the admittance parameters of the SLR can be described by a system of equations relating the input and output currents and voltages

$$\begin{bmatrix} I_1 \\ I_2 \end{bmatrix} = \begin{bmatrix} Y_{11} & Y_{12} \\ Y_{21} & Y_{22} \end{bmatrix} \begin{bmatrix} V_1 \\ V_2 \end{bmatrix} \tag{31}$$

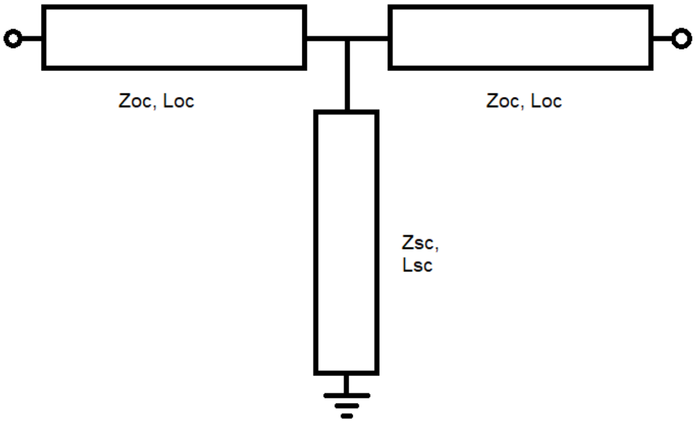

Figure 60: Elementary stub-loaded resonator circuit

The input admittance, $Y_{in} = Y_{11}$, can be obtained by expanding

$$I_1 = Y_{11}V_1 + Y_{12}V_2 \tag{32}$$

$$Y_{11} = \frac{I_1}{V_1} \mid (V_2 = 0) \tag{33}$$

That is, the input admittance is obtained by calculating the ratio of total current flowing into port 1 to the total voltage at that port, provided a short circuit condition on port 2. The input admittance for the SLR is detailed in [72]

$$Y_{in} = jY_{oc}\left[\frac{(2 * \tan(\theta_{sc}) * \tan(\theta_{oc}) - Z_{oc}/Z_{sc}}{\tan(\theta_{sc}) + \tan(\theta_{oc}) * \left(\frac{Z_{oc}}{Z_{sc}} - \tan(\theta_{sc}) * \tan(\theta_{oc})\right)}\right] \tag{34}$$

Note that the input admittance of the SLR is purely reactive and follows the form $Y_{in} = jB_i$, where B_i is the susceptance of the SLR. The ratio of characteristic impedances Z_{oc}/Z_{sc} can be rewritten as $R_z = Z_{oc}/Z_{sc}$. For resonance of the circuit, we require $Y_{in} = 0$ and recognize that the numerator of Equation 34 can be evaluated for a resonant condition for the SLR:

$$2\tan(\theta_{sc})\tan(\theta_{oc}) = \frac{Z_{oc}}{Z_{sc}} = R_z \tag{35}$$

Careful selection of the resonator lengths θ_{oc}, θ_{sc} and the impedance ratio R_z provide a design path for creating equivalent resonators for the bandpass filter topology.

5.3.2 Parallel-Coupled Lines and Immitance Inverters

Coupling between two transmission lines is often an undesired effect for high-speed digital electronics [62], but careful design of coupled lines can be employed to implement a variety of microstrip components, such as power dividers, directional couplers, and filters.

One implementation of a coupler that is frequently used in microwave circuit design is parallel-coupled lines. A circuit model for parallel-coupled lines is shown in Figure 61(a). The coupler is defined by its electrical length θ_c and its even-mode and odd-mode characteristic impedances. The even-mode impedance is the characteristic impedance of the coupler when excited with equal, in-phase voltages on each line, such that $V_1 = V_2$, which the odd-mode impedance is the characteristic impedance when the voltages are equal and 180 degrees out-of-phase, $V_1 = -V_2$. Note that V_1 and V_2 do not represent terminal voltages, but instead represent total voltage at any point on the transmission line, such that $V_1(z) = \pm V_2(z)$ for the even and odd modes, for all points z on the transmission line. Figure 61(b) shows the equivalent circuit model, which is a cascaded connection of two transmission lines with characteristic impedance Z_0 and electrical length, θ_C, separated by an ideal admittance inverter.

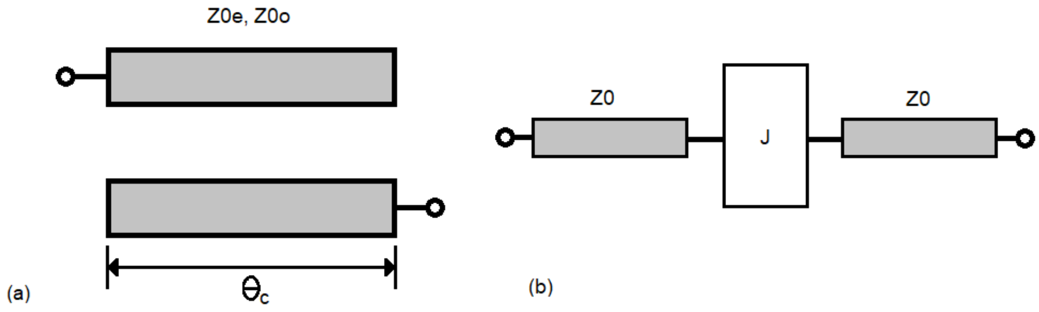

Figure 61: (a) Circuit representation of parallel-coupled lines; (b) Equivalent circuit of parallel-coupled lines. Each transmission line has length θc

The ideal admittance inverter has the property that, when terminated by an admittance Y_L on one side, the input admittance seen from its opposite side is

$$Y_{in} = \frac{J^2}{Y_L} \quad (36)$$

Here, J is a real value and is termed the inverter's characteristic admittance. Similarly, an impedance inverter has the same property as the admittance inverter, in that the input impedance of an impedance inverter terminated in load impedance Z_L is $Z_{in} = K^2/Z_L$. These two devices together are termed immittance inverters, a portmanteau of the words *impedance* and *admittance*. The utility of immittance inverters for bandpass filter design is evident in considering the need for inductive elements. In practicality, due to the inverting nature of the device, they can be used to implement, for instance, a series inductive element using a shunt capacitive element surrounded by two ideal inverters. Further, the transformed reactance may be absorbed into the design of the remaining resonator structures in a ladder topology.

As discussed in [77], equivalence between the coupler circuit and a circuit model is obtained by analyzing each circuit in terms of its ABCD parameters and equating them—although an assumption is made that the even- and odd-mode phase velocities are equal such that $\theta_{0e} =$

θ_{0o}. For brevity, the result of the analysis is shown here without detail; for equivalence, the fundamental matrices of both circuits are solved and equated for transmission lines of arbitrary coupling length, yielding:

$$Z_{0e} = Z_0 \frac{1 + JZ_0 \csc \theta_c + J^2 Z_0^2}{1 - J^2 Z_0^2 \cot^2 \theta_c} \tag{37}$$

$$Z_{0o} = Z_0 \frac{1 - JZ_0 \csc \theta_c + J^2 Z_0^2}{1 - J^2 Z_0^2 \cot^2 \theta_c} \tag{38}$$

To reiterate, satisfying Equations 37 and 38 yields equivalence between the parallel-coupled line coupler and the inverter/line model. To transform a general ladder topology bandpass filter through use of inverters, consider the prototype lowpass filter in Figure 59. Generalizing the shunt LC resonators as distributed circuits, including microwave resonators, we obtain a generalized bandpass ladder topology featuring inverters and susceptances $B_i(\omega)$ that represent the resonant structures. As shown in [62], the bandpass topology and design equations can be examined. Figure 62 shows the filter structure.

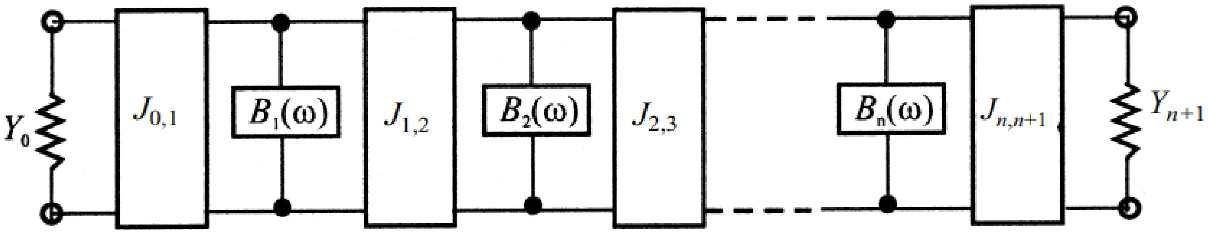

Figure 62: Generalized ladder topology filter using admittance inverters and distributed resonators

The lowpass prototype is transformed via the following equations

$$J_{0,1} = \sqrt{\frac{Y_0 FBW b_1}{\Omega_c g_0 g_1}} \tag{39}$$

$$J_{i,i+1} = \frac{FBW}{\Omega_c}\sqrt{\frac{b_i b_{i+1}}{g_i g_{i+1}}}\Big|_{i=1\ to\ n-1} \tag{40}$$

$$J_{n,n+1} = \sqrt{\frac{FBW b_n Y_{n+1}}{\Omega_c g_n g_{n+1}}} \tag{41}$$

Thus, we can transform a lowpass prototype filter to a cascaded inverter-resonator bandpass filter using the design equations above, as a function of the input and output admittances Y, the fractional bandwidth *FBW*, and the prototype filter elements g. We also must account for the distributed circuit, which is not necessarily equal to the lumped LC resonator element. However, we can create equivalence by introducing the slope parameter b for a given resonator

$$b = \frac{\omega_0}{2}\frac{dB(\omega)}{d\omega}\Big|_{\omega=\omega_0} \tag{42}$$

Note that for lumped shunt LC resonators, Equation 42 can be solved to yield $b = \omega_0 C$, and thus equivalence between the distributed element and a lumped LC resonator is retained. However, *b* is necessarily resultant from analysis of the implemented resonator and must be carefully considered in application of these equations.

5.3.3 PC-SLR Filter Design

Combining the parallel-coupled lines and the stub-loaded resonator, we obtain the PC-SLR bandpass filter, with a general structure as shown in Figure 63. Here, a series of SLRs are placed in cascade via parallel lines that couple the open-ended resonator lines θ_{oc} to subsequent SLRs. As discussed in Section 5.3.2, the equivalent circuit model of the couplers can be expressed as two transmission lines interjected by an admittance inverter with characteristic admittance *J*. An equivalent model of the PC-SLR filter is achieved by replacing the couplers with their inverter-based models, yielding a cascaded line-inverter-SLR model, as shown in Figure 64.

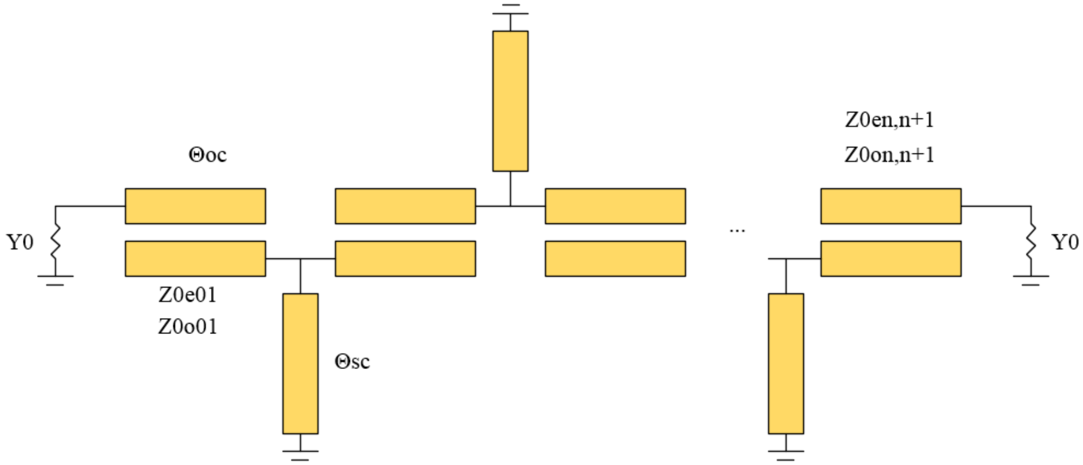

Figure 63: Nth order bandpass filter using a PC-SLR topology [72]

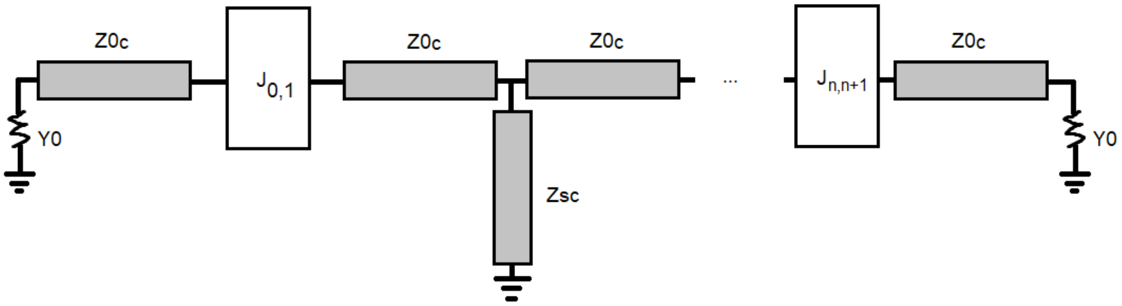

Figure 64: PC-SLR equivalent network using transmission lines and inverters

At this point, we may collapse the input and output transmission lines into the loads and assess the admittance as seen looking into the inverter, to find an equivalent representation of the line-inverter model. As further detailed in [72], the structure of the PC-SLR can be equivalently represented as a cascaded network of inverters and susceptances as shown in Figure 65. Here, the equivalence of the left and right-most sides of the filters is obtained by considering the input admittance Y_B looking into the inverter J_{01} from the interior of the filter, and the input admittance Y_A looking into the first transmission line terminated in the Y_o load, such that $Y_B = \frac{J_{01}}{Y_A} = \frac{J_{01}}{Y_0 A} + jB_b$; hence, the equivalent circuit can be comprised of a real-valued conductance $Y_0 A$, followed by inverter J_{01} and an extracted susceptance B_b.

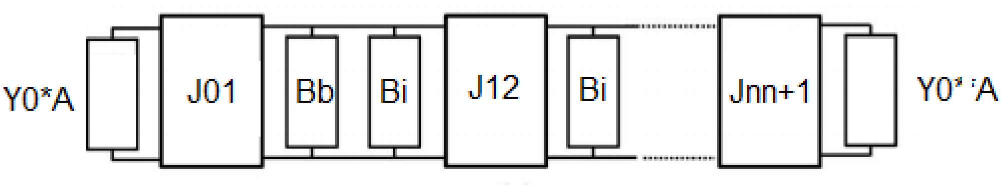

Figure 65: PC-SLR equivalent inverter-susceptance circuit

The equations to match the desired model to the transmission-line components are calculated

$$A = \frac{1 + \left(\frac{Y_{oc}}{Y_0}\right)^2 + \tan^2\theta_{oc}}{1 + \tan^2\theta_{oc}} \tag{43}$$

$$B_b = \frac{J_{01}^2}{Y_{oc}} \frac{1 - \left(\frac{Y_{oc}}{Y_0}\right)^2}{1 + \left(\frac{Y_{oc}}{Y_0}\right)^2 \tan^2\theta_{oc}} \tan\theta_{oc} \tag{44}$$

To establish the final link between the PC-SLR circuit model and the inverter-susceptance bandpass filter model discussed in Section 5.3.2, the susceptance slope parameters for B_b and B_i are required, which are evaluated as

$$b_b = \frac{\omega_0}{2}\frac{dB_b}{d\omega}|_{\omega=\omega_0} = \frac{J_{01}^2\theta_{oc}}{2Y_{oc}\cos^2\theta_{oc}} \frac{(Y_0^2 - Y_{oc}^2\tan^2\theta_{oc})}{(Y_0^2 + Y_{oc}^2\tan^2\theta_{oc})}(Y_0^2 - Y_{oc}^2) \tag{45}$$

$$b_i = \frac{\omega_0}{2}\frac{dB_i}{d\omega}|_{\omega=\omega_0} =$$

$$Y_{oc}\ \frac{\left(16\theta_{oc}(1-\cos^2\theta_{sc})\right)+8R_z\cos^2\theta_{oc}\,(\theta_{sc}+\theta_{oc}R_z\cos^2\theta_{sc})-4\theta_{oc}R_z\sin(2\theta_{sc})\sin(2\theta_{oc})}{16\cos^2\theta_{sc}\cos^4\theta_{oc}\,(\cos(2\theta_{oc})\tan(\theta_{sc})\sec^2(\theta_{oc})+R_z\tan(\theta_{oc}))^2} \tag{46}$$

Now, we have equivalence to Equations 39-42, replacing $b_{1,n-1} = b_b + b_{i=1,n-1}$ for the expressions $J_{01} = J_{n,n+1}$ and $J_{1,2} = J_{n-1,n}$, and the load impedances are likewise substituted $Y_0 = Y_0 A$. As Equation 45 contains the term J_{01}, it can be rearranged and solved to express

$$J_{01} = J_{n,n+1} = \sqrt{\frac{Y_0 * FBW * A * b_i}{g_0 g_1 - Y_0 A\dfrac{FBW\theta_{oc}(Y_0^2 - Y_{oc}^2)(Y_0^2 - Y_{oc}^2\tan^2\theta_{oc})}{2Y_{oc}\cos^2(\theta_{oc})\,(Y_0^2 + Y_{oc}^2\tan^2\theta_{oc})^2}}} \tag{47}$$

Note that in Equation 47 for J_{01}, the calculation does not match that in the literature [72] [78], due to an error in the source's expression, determined by the author of this thesis. The J_{01} term can now be used in the expression for b_b and subsequently used for solving

$$J_{12} = J_{n-1,n} = FBW\sqrt{\frac{(b_i + b_b)b_i}{g_1 g_2}} \tag{48}$$

$$J_{j,j+1} = FBW\sqrt{\frac{b_i^2}{g_j g_{j+1}}} \tag{49}$$

Finally, the inverter terms can be used to calculate the requisite even and odd mode impedances as shown in Equations 37 and 38. Thus, in principle, a bandpass filter defined by elements g_i may be realized by PC-SLR sections using the following steps:

(1) Select a filter response (Butterworth, Chebyshev, etc.) and define the fractional bandwidth FBW and center frequency ω_0 of the desired bandpass filter.

(2) Choose an impedance ratio $R_z = Z_{oc}/Z_{sc}$ and electrical length θ_{oc} for the elementary stub-loaded resonators.

(3) Using Equations 43 and 46, calculate the inverter J_{01}, susceptance *bb*, and inverters J_{12}, *Jjj+1*.

(4) Determine the requisite even- and odd-mode impedances for the parallel couplers with equations *Zoe, Zoo* and realize the couplers using synthesis software or numerical techniques.

Although these steps are comprehensive according to the literature and describe how equivalence is achieved, the results have been shown to be accurate only on narrow band filters but do not accommodate for wider bandwidth operation [72]. For example, an ideal inverter will operate the same over all frequencies, but physical inverter circuits are limited by their implementation – for instance, a quarter-wavelength transmission line has an equivalent fundamental (ABCD) matrix that follows the form of an inverter, but only near the frequency which corresponds to said quarter wavelength [77]. Application of this design process can be used in conjunction with spurious frequency analysis of the structure to improve out-of-band rejection [79] for narrow-band filters, but a model-first approach [50] can also be used together with the principles of PC-SLR filter design literature and simulation/optimization to develop wideband filters. Lower-frequency PC-SLR filters may achieve compactness by considering the total length of the coupled lines and must trade increased bandwidth and improved pass-band performance via additional transmission zeros (couplers approaching θ_{oc} = 90°) for total filter size $(2\theta_{oc} + \theta_{sc})$. For higher frequency filters, designers may take advantage of the reduced wavelength to increase bandwidth while retaining a compact footprint. While the above procedure relies on narrowband assumptions, a wideband PC-SLR filter may be designed through the following steps:

(1) Select a desired passband response based on system requirements (bandwidth, ripple, roll-off, etc.).

(2) Create a PC-SLR model and optimize coupler length and even- and odd-mode impedances, and stub parameters to find an operating point the meets specifications with an idealized coupler and stub.

(3) Implement and simulate physical components that match the idealized couplers and stub using a desired substrate.

(4) Perform an electromagnetic simulation and optimization of the PC-SLR filter to obtain the desired performance metrics.

Parametric EM simulations are required because of the complexity of the structures being considered. We have successfully shown this process to work, resulting in a design procedure that can be scaled to accommodate different bandwidths as well as different substrate material thickness and permittivity.

5.4 Ultra-wideband PC-SLR Bandpass Filter Implementation

Let us design a 1-stage PC-SLR filter with passband ripple L_{AR} of 0.01 dB and operates over the 2-18 GHz bandwidth of the radar system. Note, for a lossless two-port microwave network $|S_{11}| + |S_{21}| = 1$. Hence, a maximum passband ripple of $L_{AR} = 0.01$ dB is equal to S_{21} = 99/100, which necessitates

$$S_{11,max} = \left(1 - \frac{99}{100}\right) = 0.01 \rightarrow dB\left(S_{11,max}\right) = -20 \tag{50}$$

Then, our desired filter has a maximum in-band return loss of -20 dB. For wideband operation, the physical lengths of the structures will be such that $l = \lambda/4$ at the center frequency 10 GHz. To proceed, an idealized model is created in the ADS schematic view. The model is shown in Figure 66. The couplers and the stub are designed at electrical length (“Ec”) of 90°, the frequency (“F”) is the center frequency of the design (10 GHz), and the even and odd mode impedances (along with the stub impedance) are variables to be optimized. To find an operating point, an optimization procedure is followed based on the requirements of the filter, primarily via an optimization goal of dB(S(1,1)) < -20. We may estimate an operating point of $Z_{0e} > 100$ and $Z_{0o} < 25$ based on wideband implementations of PC-SLR filters [50] [74] to reduce the solution space of the optimization. Including the short circuit stub's characteristic impedance as an optimization variable permits further improvement of the passband return loss [74]. Running the optimizer for the even- and odd-mode characteristic impedances and the short circuit stub impedance rapidly converges to a response with Z_{0o} = 8 Ω, Z_{0e} = 108 Ω, and Z_{sc} = 100 Ω.

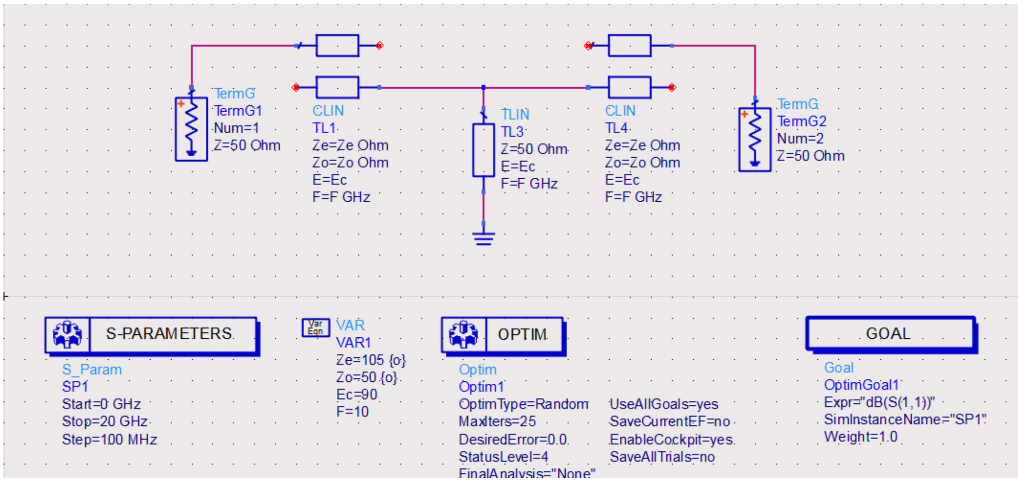

TermG
TermG1
Num=1
Z=50 Ohm

CLIN
TL1
Ze=Ze Ohm
Zo=Zo Ohm
E=Ec
F=F GHz

TLIN
TL3
Z=50 Ohm
E=Ec
F=F GHz

CLIN
TL4
Ze=Ze Ohm
Zo=Zo Ohm
E=Ec
F=F GHz

TermG
TermG2
Num=2
Z=50 Ohm

S_Param
SP1
Start=0 GHz
Stop=20 GHz
Step=100 MHz

VAR1
Ze=105 {o}
Zo=50 {o}
Ec=90
F=10

Optim
Optim1
OptimType=Random
MaxIters=25
DesiredError=0.0
StatusLevel=4
FinalAnalysis="None"
UseAllGoals=yes
SaveCurrentEF=no
EnableCockpit=yes
SaveAllTrials=no

Goal
OptimGoal1
Expr="dB(S(1,1))"
SimInstanceName="SP1"
Weight=1.0

Figure 66: ADS model of single-stage PC-SLR filter using ideal couplers and transmission lines

Now, physical models for the coupler and stub must be determined. At this point, it is important to address the desired physical layout of the filter. As a filter with similar passband performance and bandwidth has been demonstrated [50] using broadside coupled microstrip parallel-coupled lines, we aim to implement our filter using the proven physical implementation. However, as discussed in Chapter 4, the stack-up is varied based on available materials, and thus we must conform our design to what may be manufactured on the 4-1-1 mils LCP substrate stackup. In this substrate configuration, the input feed is connected to the top-side open-circuited lines, that are coupled to the internal-layer stub-loaded resonator. According to the intended manufacturer, minimum line width and space using their “Advanced” manufacturing capabilities can be 0.002”, corresponding to 50 µm. Using a calculator for embedded microstrip, the maximum impedance obtainable for the short circuit stub is 87 Ω.

Thus, the optimization is constrained, and setting Z_{sc} to 87 Ω, we yield new values of Z_{0e} and Z_{0o} of 102 Ω and 8 Ω, respectively. The response of the optimized filter is shown in Figure 67. The return loss is better than 10 dB across the 2-18 GHz band, and better than 30 dB from 5-15 GHz.

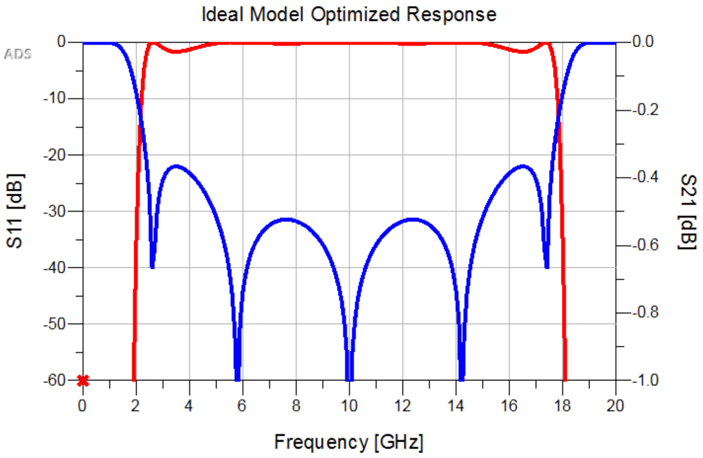

Figure 67: Simulated model response for ADS single-stage PC-SLR using ideal components Z_sc=88 Ω, Z_0e=102 Ω, Z_0o=8 Ω.

To implement as physical devices, the ideal coupler and stub components must be replaced by physical models. For the short circuit stub, the ideal transmission line is replaced by an embedded microstrip line. As previously calculated and due to manufacturing limits, the width of the line is 50 µm. The length can be estimated, as embedded microstrip demonstrates a propagation velocity of ~80% of a surface microstrip line [80] [81]. The effective dielectric constant of microstrip for the desired stack up is $\epsilon_{eff} = 2.5$, and we calculate

$$v_{emb} = 0.8 * v_{ustrip} = 0.8\frac{c}{\sqrt{\epsilon_{eff}}} = 1.52e8\ m/s \tag{51}$$

A quarter wavelength at 10 GHz at this velocity of propagation can then be calculated by $f\lambda = v_p$, and hence the length of the stub is calculated l_{stub} = 3.8 mm. For the broadside microstrip coupler, numerical techniques using spectral domain analysis are available [82], and capacitor matrix analysis methods are possible using EM software [83], but parametric analysis or direct optimization are also possible by using the ideal coupler and a multi-layer coupler in ADS and creating an error term $E = |S_{11,ideal} - S_{11,model}|$ for S in dB to minimize. This technique was utilized to create an equivalent microstrip broadside coupler, as shown in Figure 68. The error term is plotted as a function of frequency in Figure 69, and a comparison of S parameters for the ideal coupler (light) and microstrip broadside coupler (dark) are shown in Figure 70. The error term has a maximum of 1.2 dB difference between the models.

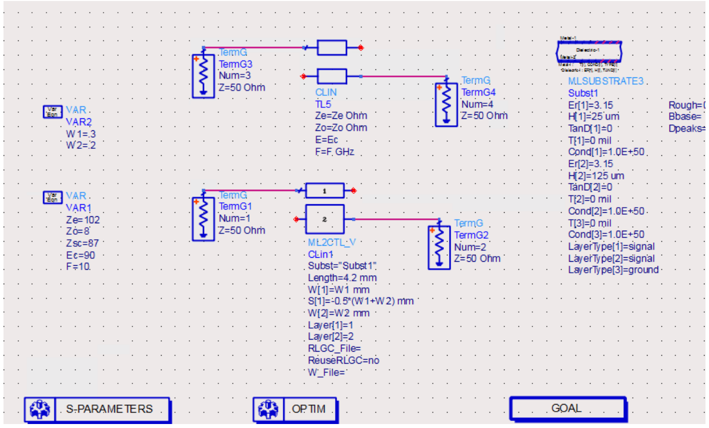

Figure 68: Equivalent broadside-coupled microstrip extraction schema

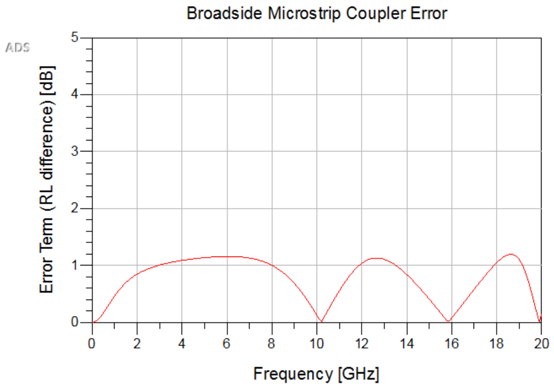

Figure 69: Return loss difference error between ideal coupler and broadside multilayer coupler model

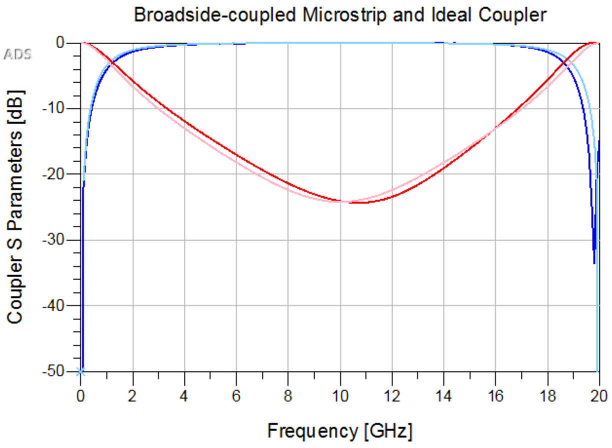

Figure 70: Comparison of simulated S-parameters for ideal coupler and broadside multilayer coupler model

The physical parameters of the broadside couplers are W1 = 0.28 mm, W2 = 0.23 mm, and L = 4.3 mm. Along with the previously-determined values for length and width of the stub, a starting point for a full-filter simulation and optimization is obtained. Replacing the ideal components of Figure 66 with the multilayer T-line models, and using the lengths and widths of the couplers and stub as variables, an optimization is run with a goal for return loss greater than 20 dB. The goal of this optimization is to determine initial values for a full EM simulation of the filter. Upon optimization, the filter response is shown in Figure 71. Although the response reaches a worst-case input return loss of 19 dB, the eventual response of the filter is expected to perform better than 10-dB return loss, and reductions in performance are expected. The optimized initial values for the lengths and widths are presented in Table 7, corresponding to the dimensions as displayed in Figure 72, which displays layer 1 and 2 as orange and blue rectangles, respectively. Note that the gap between the top-layer conductors is equal to the width of the short-circuited stub.

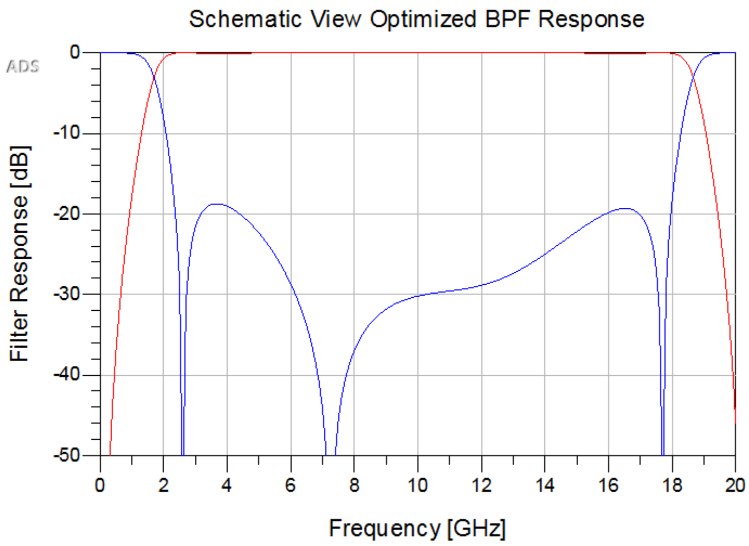

Figure 71: Schematic view multilayer BPF model simulated response

Table 7: First-pass dimensions of PC-SLR Filter

Parameter	**Value**	**Parameter**	**Value**
L1	4.25 mm	W2	0.35 mm
L2	4.5 mm	Wsc	0.15 mm
W1	0.3 mm		

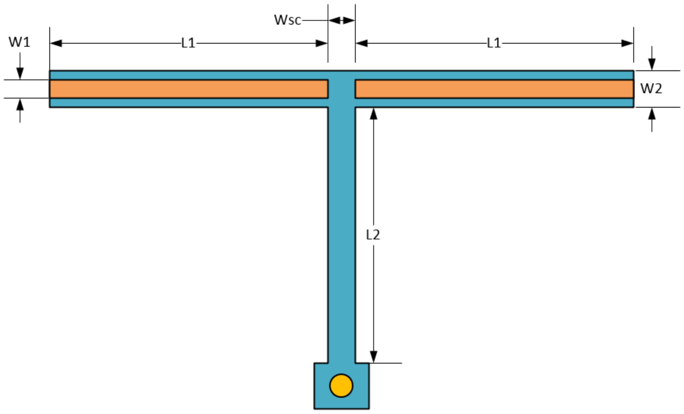

Figure 72: Layout dimension diagram for PC-SLR Filter

To finalize the design, the above dimensions are imported into the ADS layout view in preparation for EM simulations. The short circuit was initially implemented as a 0.15-mm drill via hole to ground, centered on a circular antipad with 0.33-mm diameter, though it was later changed to a 0.3-mm drill via hole with an antipad of 0.56-mm diameter to accommodate manufacturing requirements. While the finite size and non-ideal effects of the through-hole via will contribute to the overall length of the short-circuit stub and its response, it will ultimately be compensated by the optimization. The layout view was parameterized, as discussed in Chapter 2. As the eventual manufacturing of the filters requires both no launch and a CPW probe launch, two optimizations were run for both layouts. Design of the CPW probe landings for the BPFs was accomplished in tandem with the LPF design, so discussion of the CPW launch is not repeated here. Figure 73 and Figure 74 show the ADS layout view of the bandpass filters with and without the probe landing. To reduce simulation time, the design was first optimized for the microstrip launch filters, and the widths and lengths were inserted as a starting point for the CPW optimization. The via holes were assumed to be solid in the simulations.

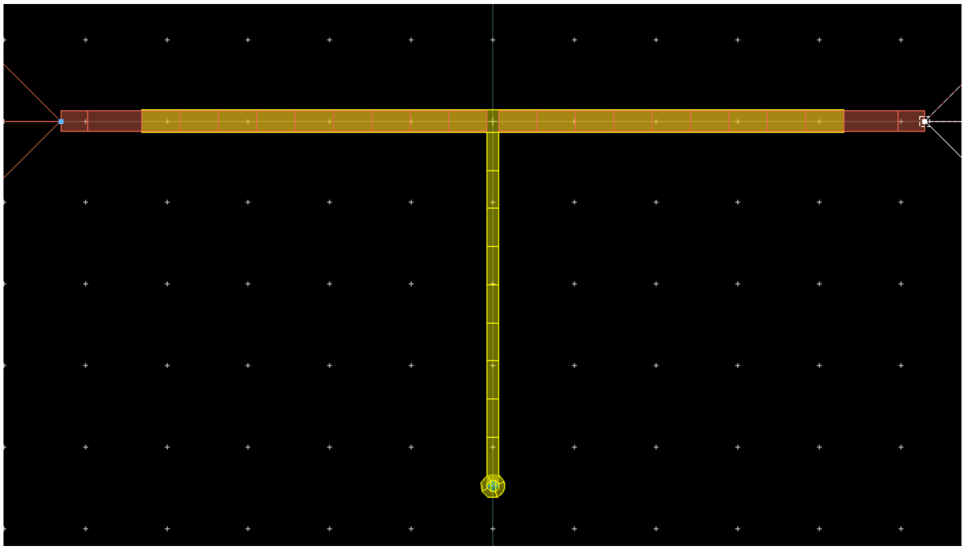

Figure 73: BPF EM layout with microstrip launch

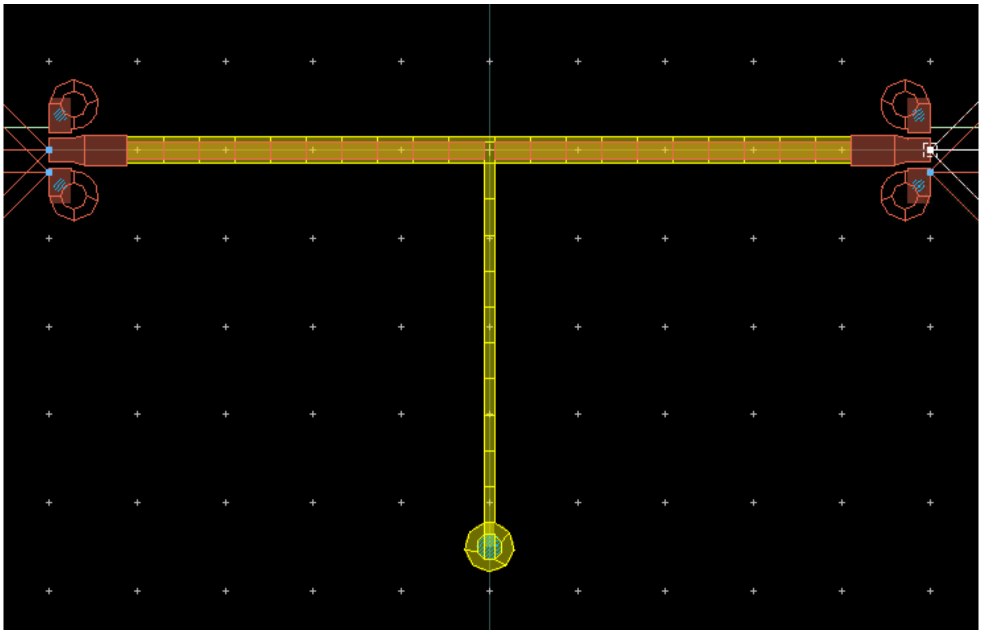

Figure 74: BPF EM layout with CPWG launch

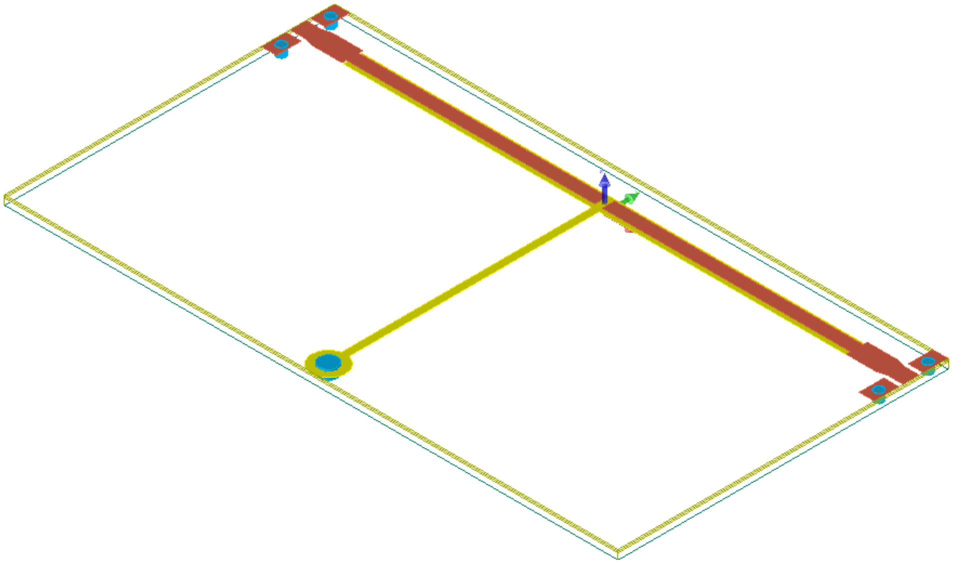

Figure 75: 3D layout of PC-SLR bandpass filter

The EM layout was parameterized and used as a component for circuit/EM cosimulation in a separate schematic cell. The lengths and widths L1, L2, W1, W2, and Wg were used for optimization, upon which a nominal filter response (dark blue) was obtained. After this, a parameter sweep was done for the lengths and widths L1, L2, W1, and W2, while Wg was kept constant at 150 µm to minimize variations. The filter variation response is shown in Figure 76, with the nominal design highlighted. As previously seen in the idealized filter response, five passband nulls are present for the nominal filter, but variation of filter elements allows nulls to collapse into the same positions, and the filter response is sensitive to variation. Each filter variant shown in the figure is based on a 25-µm perturbation of the width and length variables and unlike the LPF, the location and number of nulls highly varies between variations. The extended passband response is also notable, as the filter was previously designed for 2-18 GHz operation, but the simulated filters exhibit an upper-band cutoff of 19-20 GHz. However, this result is not entirely detrimental, as the BPF also exhibits periodicity with frequency, with a passband that repeats at frequencies beyond the nominal operating frequencies and must be cascaded with a lowpass filter to remove repeated passbands. The highpass characteristic of the BPF is the desired aspect, and an extended upper-band response is not problematic and may prove beneficial. The BPF and LPF will be implemented in cascade to remove repeated passbands, so a higher cutoff for the BPF will result in a band-edge response largely dictated by the LPF.

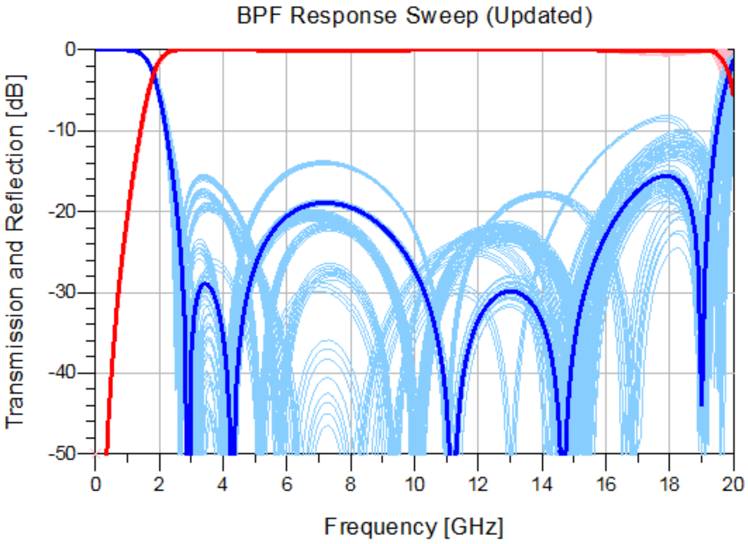

Figure 76: Parametric EM simulation results of the BPF after varying L1, L2, W1, and W2

After determining the nominal and perturbed filter designs, the filter layouts were designed in CADSoft Eagle using the script described in Section 4.5, allowing for rapid population of a panel. The panel layout is shown in Figure 77. Each filter is marked by a four-marker code with horizontal and vertical bars, horizontal bars indicating an “A” and vertical bars indicating a “B.” The panel includes 35 BPF design variations, “AAAA” through “BBBB”, and both microstrip and CPW launches, *i.e.*, 32 design variations. With the remaining room for three design variants, the nominal filter was included thrice more – two nominal filters using the CPW launch and one for the microstrip launch.

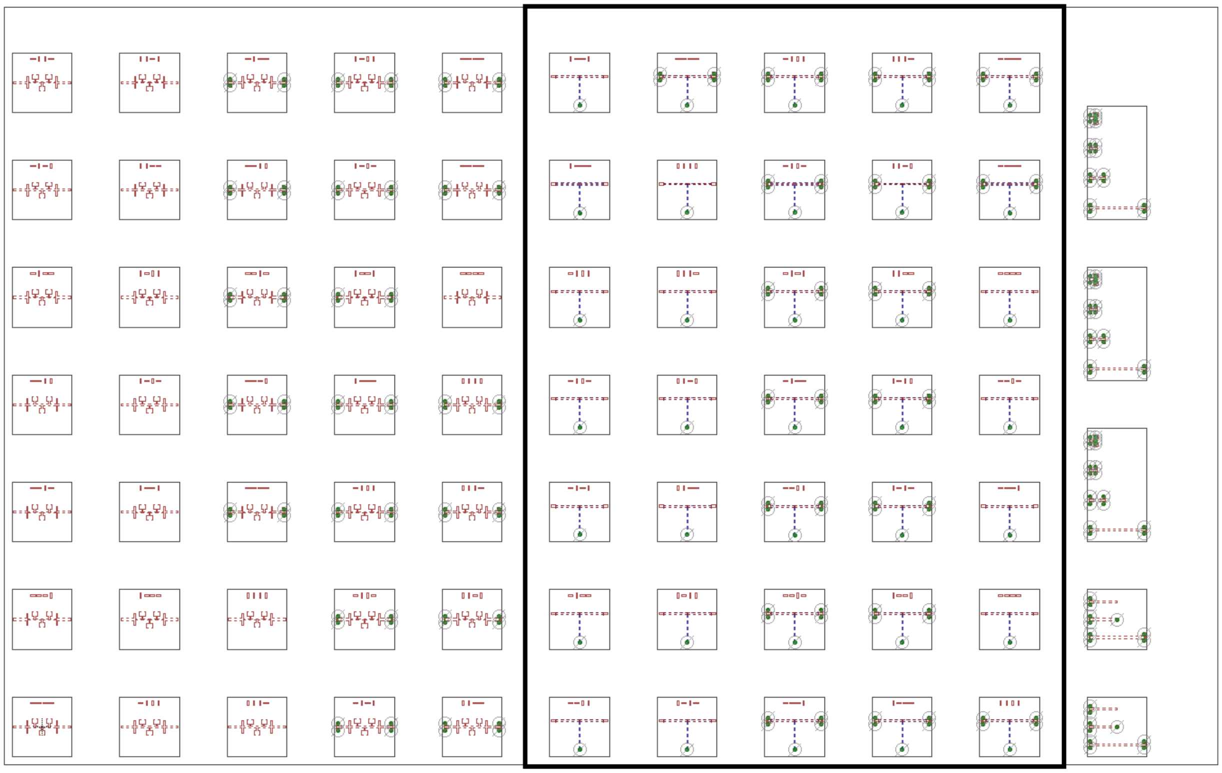

Figure 77: Panelized layout of BPFs in Eagle

5.5 Measurements and Results

5.5.1 Panelized BPF Measurements

The panel incorporating all design variations was manufactured by Hughes Circuits, as described in Chapter 4. The BPF section of the manufactured panel is shown in Figure 78. The figure compares the BPF panel section to a penny for size reference. The measurements of the panel were taken in tandem with the LPF measurements; details about calibration and the probe station are available in Chapter 4 and are not repeated here. The measured S-parameters for the panelized filters are shown in Figure 79, with a detailed view of S21 in Figure 80.

All the tested filters exhibited an insertion loss of 0.3 dB or better at 10 GHz as well as a 3-dB bandwidth extending from 2 GHz to 19.25 GHz. The 1-dB bandwidth is affected by the upper-band cutoff, which varies between 16.2 GHz and 18.4 GHz. All manufactured BPFs exceed

30 dB out-of-band rejection at 760 MHz and 20.9 GHz, 40 dB at 520 MHz and 22 GHz, and over 65 dB rejection at 200 MHz. At higher frequencies, the filter response is periodic, and a second passband begins at 24 GHz. The variation in passband response is discussed in greater detail in Section 5.5.2.

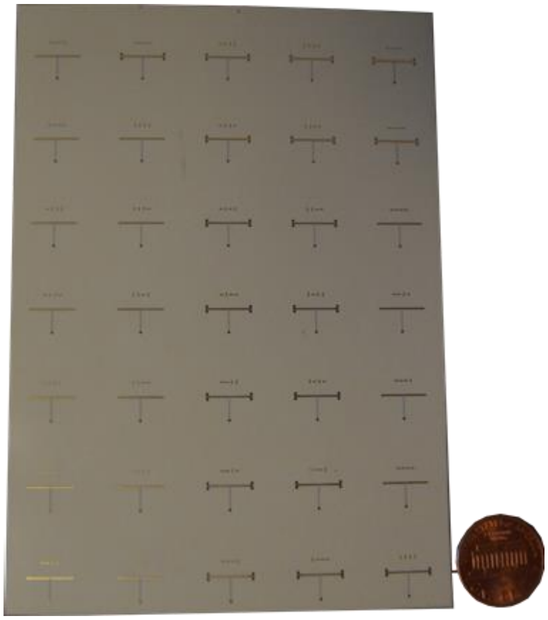

Figure 78: Manufactured panel section featuring the BPFs

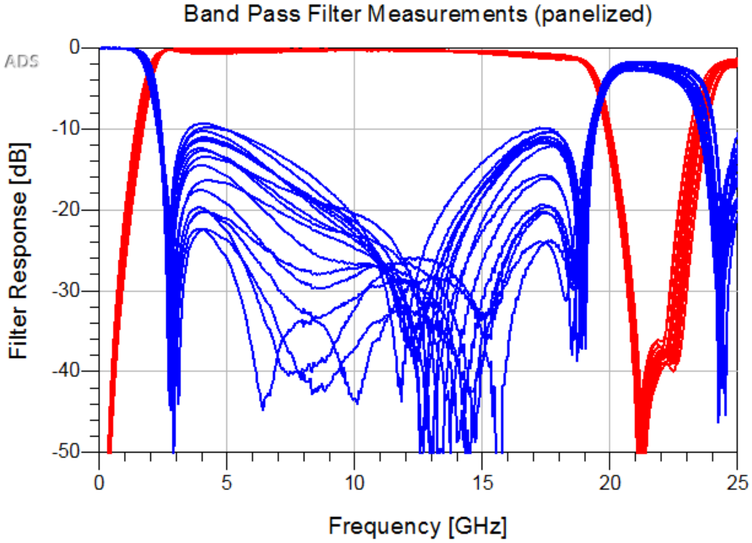

Figure 79: Measured responses for panelized manufactured bandpass filters

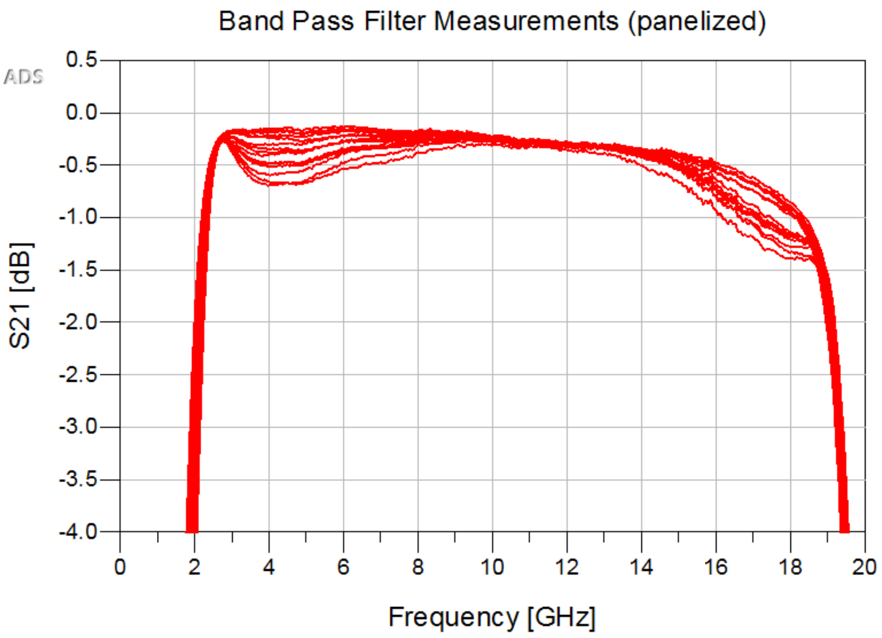

Figure 80: Panelized filter S21 measurements

The filter exhibiting the worst passband performance is one of the nominal “AAAA” filters, which had a worst-case in-band return loss of 9.8 dB at 4.3 GHz and slightly exceeded 1-dB insertion loss at 16.2 GHz. A comparison against simulated data for this filter is provided in Section 5.5.2. One of the best performing filters is the “AABB” BPF, which exhibited better than 1-dB insertion loss from 2.3 GHz to 18.4 GHz, and a worst-case in-band input return loss of 19.3 dB. A comparison between the measured and simulated results for this filter is shown in Figure 81. As with all other filters, the measured results featured increased passband attenuation at higher frequencies. As in the case of the low-pass filter, this is attributed to conductor and dielectric losses that were unaccounted for by the simulation. The measurement and simulation show excellent S11 match at the band edges, featuring nearly identical responses near 2 GHz and 18 GHz. The 3-dB bandwidth of the measured filter is reduced by ~3% compared to the EM simulation, extending from 2 to 19 GHz. The location of passband nulls differs between the data sets – this may be due to biases toward larger manufactured filter structures and will be discussed in greater detail in the next section.

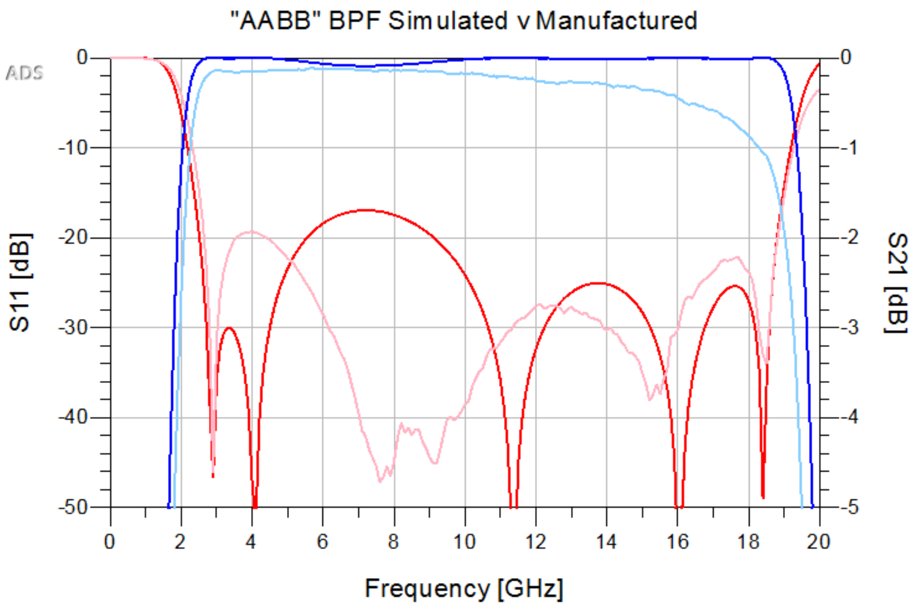

Figure 81: Comparison of "AABB" simulated (dark) and measured (light) performance

5.5.2 Routed BPF Measurements

After performing measurements on the panelized filters, each individual circuit was also routed using a high-power laser from consortium members at the University of Nebraska Lincoln. Figure 82 shows a photograph of one of the routed filters with a penny for size reference. The routed filters were re-measured, and the measured S-parameters of the routed BPFs are provided in Figure 83.

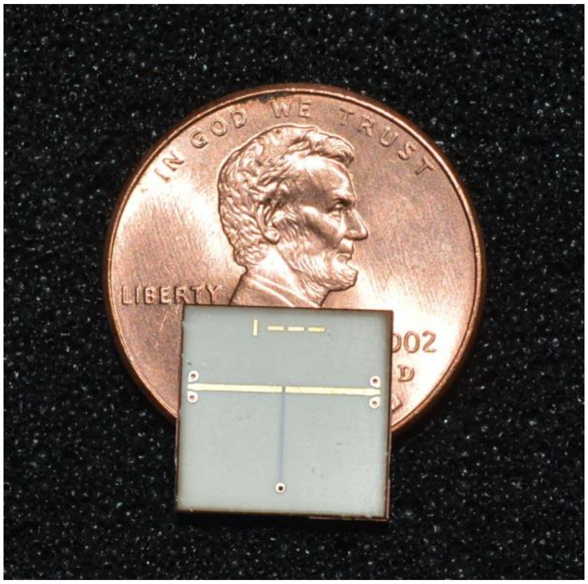

Figure 82: Photograph of a manufactured BPF after laser routing

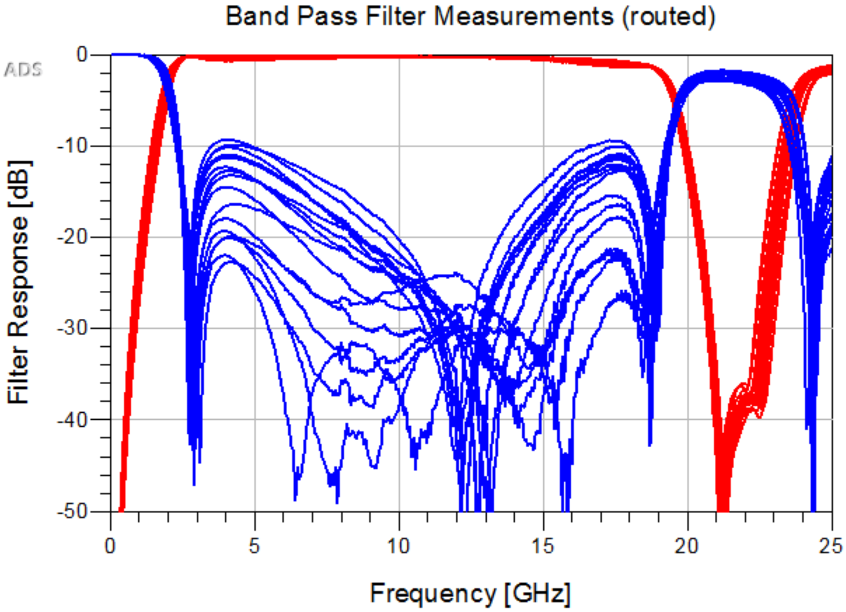

Figure 83: Measured response of the BPFs after laser routing

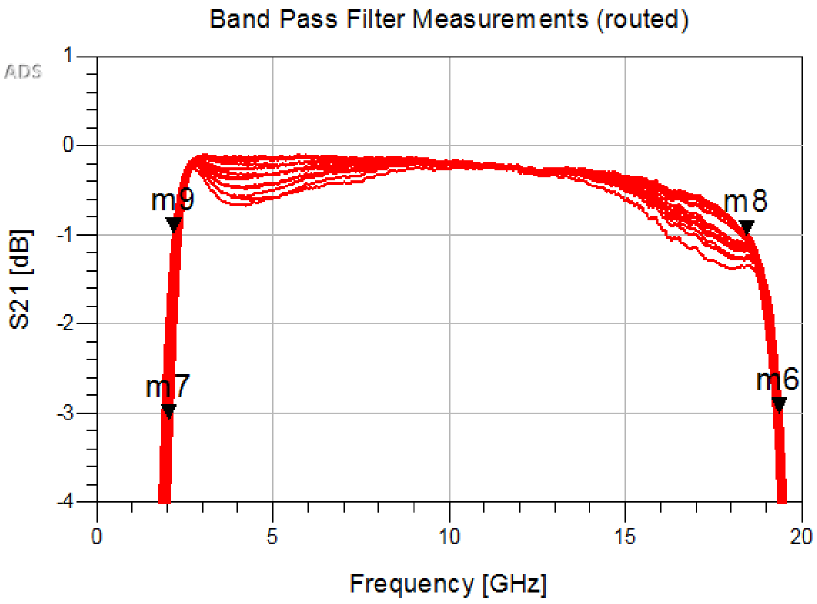

Figure 84: Measured transmission response of the BPFs after laser routing

We did not observe any significant variation in the measured response of the filters after routing. For example, Figure 85 shows a comparison of the filter “ABBA” as measured both pre- and post-routing. The responses are largely identical except for slight variation in the S11 response around 11-12 GHz. Although the responses do not vary highly from measurements taken of the panelized filters, the repeatability of the measurement for individual filters, measured in the same location without requiring movement of either the probes or the panel, leads to higher consistency between measurements. No large deviations between measurements for any particular filter were noted, but due to the repeatability in probing and consistency, the post-routing measurements are used for the following discussion.

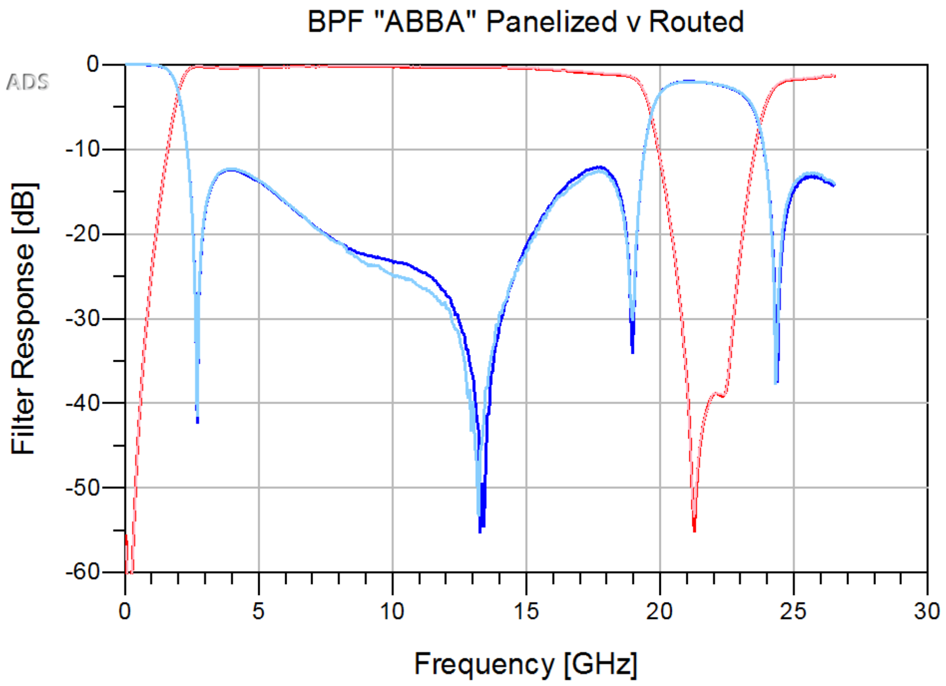

Figure 85: Comparison of BPF measurement between panelized (dark) and routed (light)

Figure 86 shows the measured group delay of the filters. They exhibit a nearly constant group delay of 70 ps from ~5 GHz to 16 GHz, reaching 100-ps delay at 4 GHz and 17.5 GHz, and a continued gradual, expected increase toward the band edges, reaching 330 ps at 2 GHz and 290 ps at 19.5 GHz.

As mentioned in Section 5.5.1, the nominal “AAAA” filters demonstrated the worst-case S11 and S21 responses of the manufactured filters. Figure 87 shows a comparison of the nominal “AAAA” BPF EM simulation to three manufactured filter responses. The manufactured filters have the same layout, but the center null differs by as much as 1 GHz in location, and while the responses match at the band edges, there is as much as 4-dB variation in the S11 response near the 4-GHz peak. The filters retain much of the same response, as the layouts are identical and the measurements were taken both pre- and post-routing without variation, the difference between the filters can only be attributed to manufacturing tolerance and design sensitivity; for future manufacturing, a lower tolerance, if available, should be a high priority for consistent results.

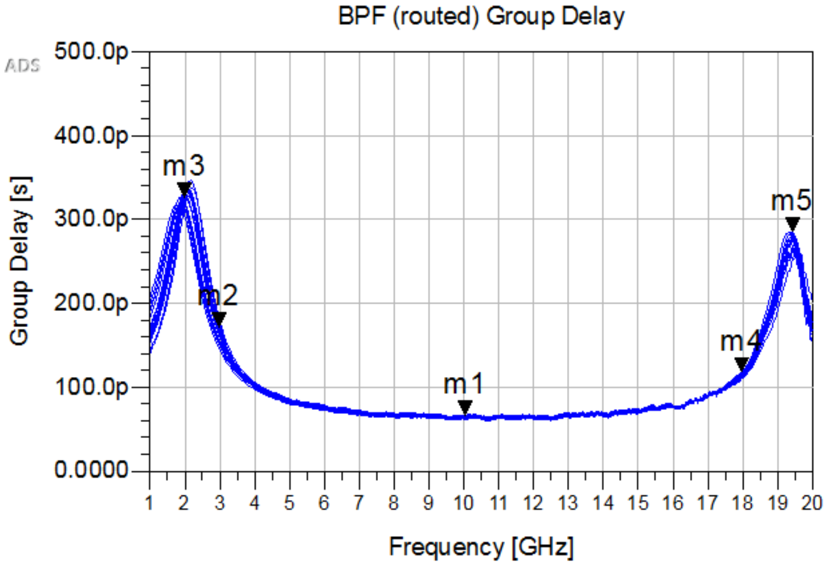

Figure 86: Group delay of the manufactured BPFs

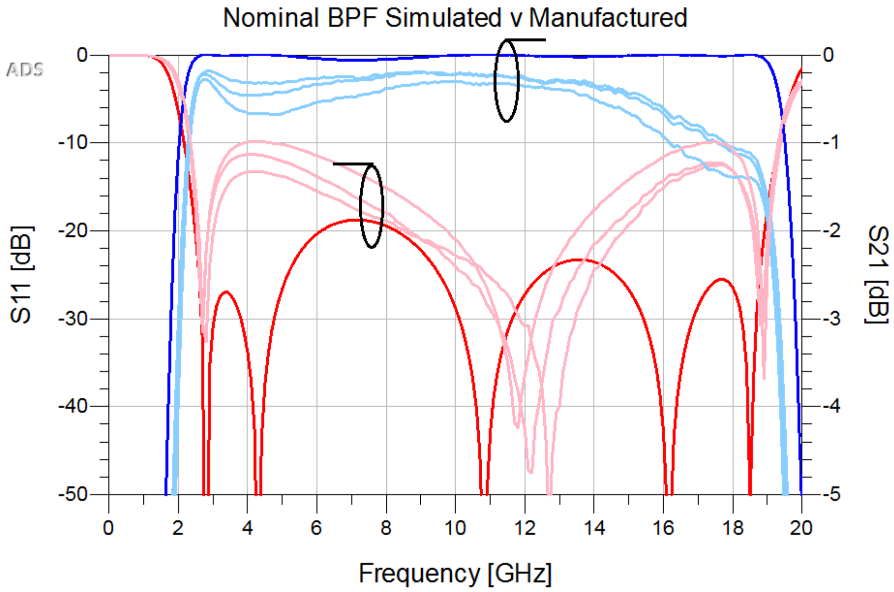

Figure 87: Comparison of simulated (dark) and three manufactured (light) nominal BPFs

Additionally, the manufactured filters lack the passband nulls at 4.25 and 16.2 GHz featured in the simulated response. This is the case with many of the filters when comparing Figure

76 and Figure 83. All simulated responses contain five return loss nulls across the passband, but most of the manufactured filters only contain three apparent nulls. This characteristic was also discovered in the ideal filter schematic, as simulations showed variation from the nominal Z_{0o} and Z_{0e} coupler impedances results in a reduction of passband nulls and reduced input return loss. This sensitivity to ideal coupler impedance variation was considered through the design, aiming for 20-dB return loss across the band such that imperfect coupler characteristics would reduce performance but would meet the 10-dB return loss criterion. However, provided that Figure 81's "AABB" filter does feature five passband nulls indicates that better performance may be possible and predictable.

As discussed in Chapter 4, the increased size of filter elements due to non-zero polygon widths and imperfect routing of the copper can alter the filter response. As such, each filter is believed to retain a bias toward larger element widths and shorter transmission lines than simulated. Examining a filter with longer lengths and reduced widths is a better approximation for the span of designed filter variations, and therefore is likely to feature less deviation from the nominal even- and odd-mode coupler impedances. This explanation would account for the remarkable performance of the "AABB" filter – that is, the filter with nominal lengths but reduced widths for the coupler. Examining the S11 response in Figure 81, there are five nulls in the passband at 3, 7.5, 9.2, 15.5, and 18.5 GHz. The consequence of distinct passband nulls is improved return loss, which is better than 26 dB from 6 GHz to 16 GHz, and a reduced maximum in-band S11 of -19 dB.

To further explain a bias toward wider filter elements due to polygon widths and routing offset, Figure 88 shows a comparison between the measured data (red, blue), the initial EM simulation (light blue, pink) and a compensated layout (green, orange). The compensated layout was created by augmenting the widths of the filter elements by 10 µm and the length of L1 by 5 µm. Examining the upper band S21 response, the compensated layout better approaches the cutoff frequency of the measured filter. The fourth passband null is also shifted from 16.8 GHz to 15.5 GHz, nearly matching the measurement. Additionally, the S11 peak between the 2nd and 3rd null is reduced, and the peak between the 3rd and 4th null shows a much better match to measured data than the original EM simulation.

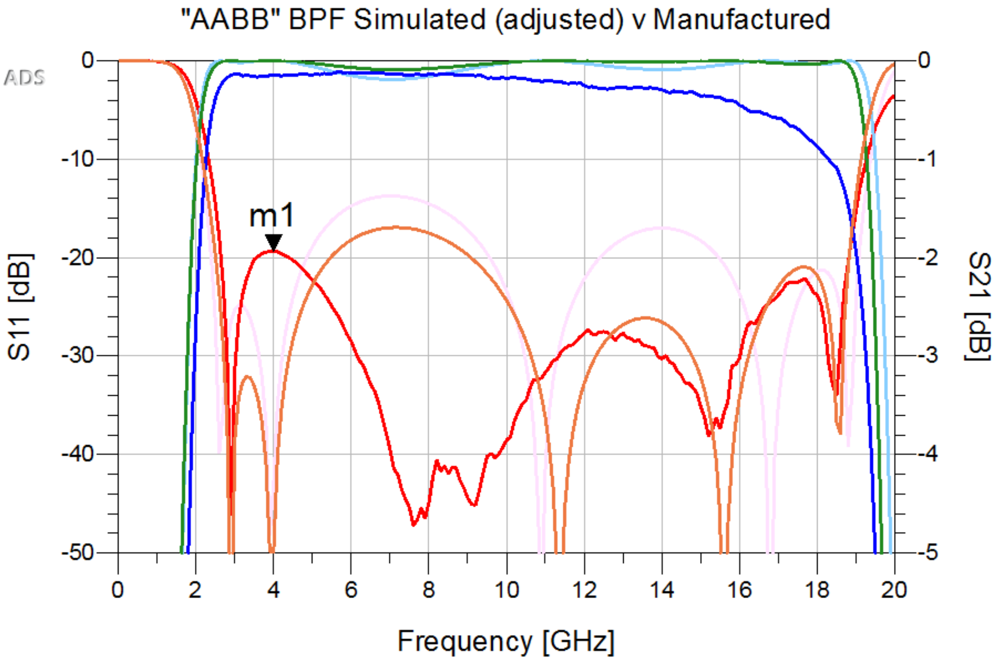

Figure 88: Adjusted simulation response to improve match to measured data

Finally, it is important to consider the cascaded BPF-LPF response, as the BPF has repeated passbands beyond the first and the higher-frequency response may need to be suppressed using the LPF in certain operating scenarios (*e.g.* pre-select filter at the input of the receiver). The cascaded performance of the “AAAA” LPF and the “AABB” BPF is shown in Figure 89. The cascaded response shows a maximum 10 dB return loss in band; the 3-dB bandwidth is 2—18.4 GHz, and the insertion loss is better than 2 dB for 2.1—16 GHz. The out-of-band rejection is 67 dB at 200

MHz, 18 dB at 20 GHz, and better than 40 dB beyond 20.75 GHz. These figures of merit are comparable to the filters currently being used in the existing system, with the added advantage of a significantly reduced area and lower profile.

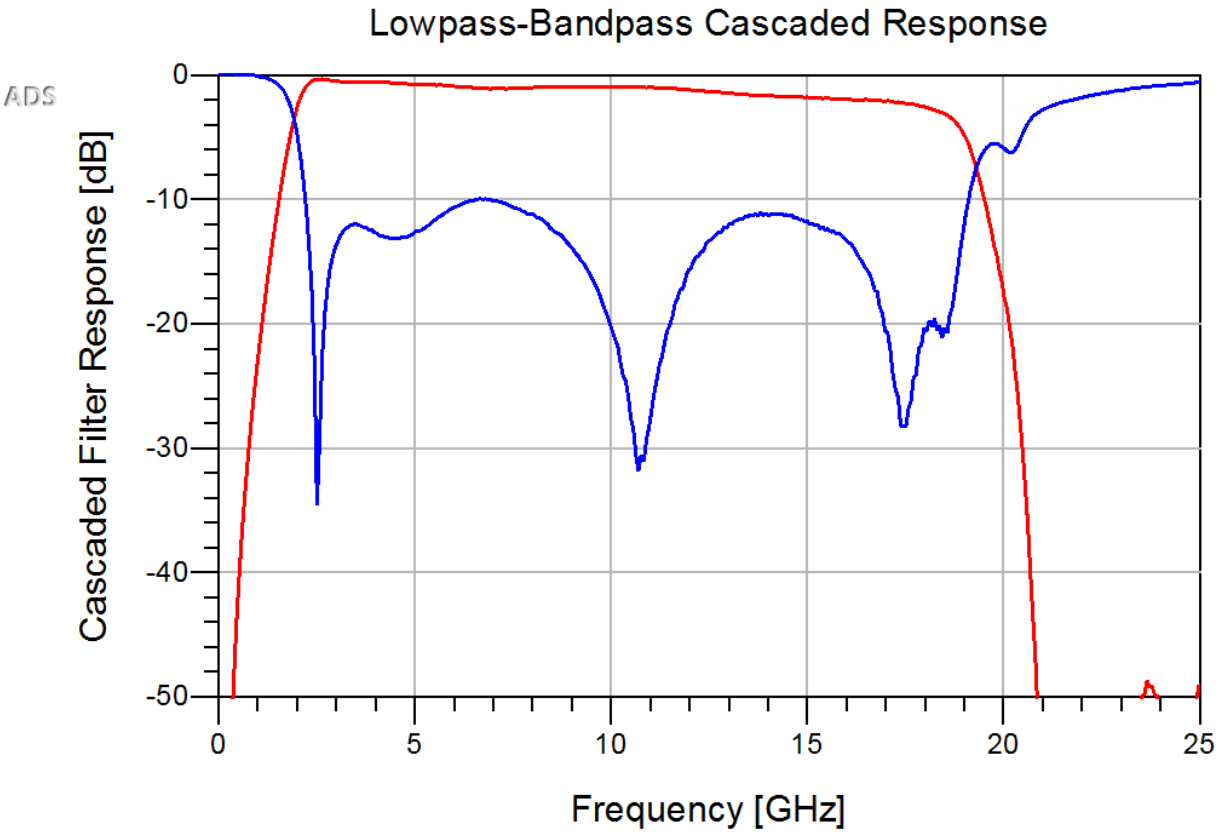

Figure 89: Cascaded response of "AAAA" LPF and "AABB" BPF

6: Conclusions and Future Work

At the Center for Remote Sensing of Ice Sheets at the University of Kansas, iterations upon the UWB FMCW radar have continued to achieve improved range resolution and miniaturization. To the end of reducing the size of the UWB Snow Radar system, the RF front end's move toward MCMs had a major bottleneck in the form of the microwave filter components, which were facilitated by the work presented in this thesis. The radar's latest compact modules were also detailed, and their necessary biasing circuitry designs were presented. The Tx module has a typical power consumption of ~15 W and provides 30-dB gain across the 2—18 GHz passband, an increase of ~10-dB over the reference system. The Rx module has a typical power consumption of ~3.6 W, noise figure of 3.5 dB, and measured ~55 dB conversion gain. The modules reduce the size of the RF front end by 80% compared to the reference system.

Two UWB filters—low pass and band pass—were designed on Liquid Crystal Polymer. The filters were designed using the Advanced Design System (ADS) CAD software, using known design methodologies as a starting point. Many variations on the filter designs were selected and manufactured on a panelized board for testing of discrepancies from the selected design simulated functionality and the manufactured filters for a final selection. As printed circuit board (PCB) design software such as CADSoft Eagle does not allow for creation of variables (such as lengths and widths), a necessary framework for the automated creation of panelized design variations was built, utilizing a Matlab script that translates physical filter design parameters (*eg.* L1, W2, etc.) from a data file into a PCB layout for direct export. While the initial legwork takes some time to set up, this methodology creates precise, repeatable layouts without the margin for error that manual calculation and layout inherits from human design, and reduces small and exact layout changes from hours-long processes to taking only seconds.

The filters were procured in a panel from a professional manufacturer, and measurements were taken using a Vector Network Analyzer for comparison against ADS electromagnetic/circuit co-simulated data. Featuring a wide bandwidth, low insertion loss, and a strong input match across the passband, the filter designs also heavily enable the miniaturization of the 2—18 GHz Snow Radar system, decreasing the footprint of the SSS filters from 4.25 sqcm (highpass) and 3.63 sqcm (lowpass) to only 1 sqcm, bearing a height of only 150 µm and eliminating the need for a custom enclosure. All manufactured LPFs exhibited 10-dB minimum return loss across DC—19.5 GHz, better than 1.4-dB insertion loss at 18 GHz, and more than 30-dB out-of-band rejection at 22.5 GHz. Overall, the BPFs exhibited very close to 10-dB minimum return loss in-band and better than 1-dB insertion loss from 2.2—16.2 GHz, and a 3-dB bandwidth of 2—19.5 GHz. However, high sensitivity to routing biases varied the responses of the manufactured filters slightly, and the best performing among them exhibited a worst-case in-band return loss of 19 dB, and an outstanding 26-dB maximum return loss from 6 GHz to 16 GHz. The cascaded BPF-LPF response for two of the best-performing filters exhibited a 3-dB bandwidth of 2—18.4 GHz, a minimum in-band return loss of 10 dB, and a 200-MHz suppression of over 60 dB, while only retaining a cascaded length of ~2 sqcm and a height of 150 µm. The study of these filter variations permits repeatability in future manufacturing while retaining system performance and reducing cascaded length by 80% and height by 90%.

These filters constitute and important precedent for the continued miniaturization of the radar system, for which the RF subsystems will be fully integrated using MCMs in the near future. Currently, the Tx and Rx biasing and RF are being integrated as fully planar, single-board modules on low cost substrate material. Future work also includes the incorporation of active devices along with the filters developed through this investigation using printed interconnects and other advanced packaging techniques.

Additionally, the collaboration between KU and Honeywell Radar 2021 Consortium members has and will continue to be an important aspect of the system's ongoing development. Members at Michigan State University are currently processing the presented LCP microwave filters concurrent to the writing of this thesis. A sub-set of the best-performing filter design variations was included in a smaller panel with diamond-shaped alignment marks to ensure accurate co-registration between the different material layers (Figure 90). An initial pass at fabricating the filters based on this mask design can be seen in Figure 91. Small features were successfully fabricated (140-µm gaps and 200-µm trace widths). Since the copper thickness is ~17 µm, provision must be made to compensate for fabrication tolerances derived from the etching process. In particular, 25-µm increases to feature widths and lengths, along with larger ground pads for the GSG probe ends, were implemented. Simulations showed that the effects of these changes do not have any adverse effect in filter performance (Figures 92-94). These changes will improve yield of filters using MSU's process, providing KU with additional filters while retaining collaboration within the Consortium.

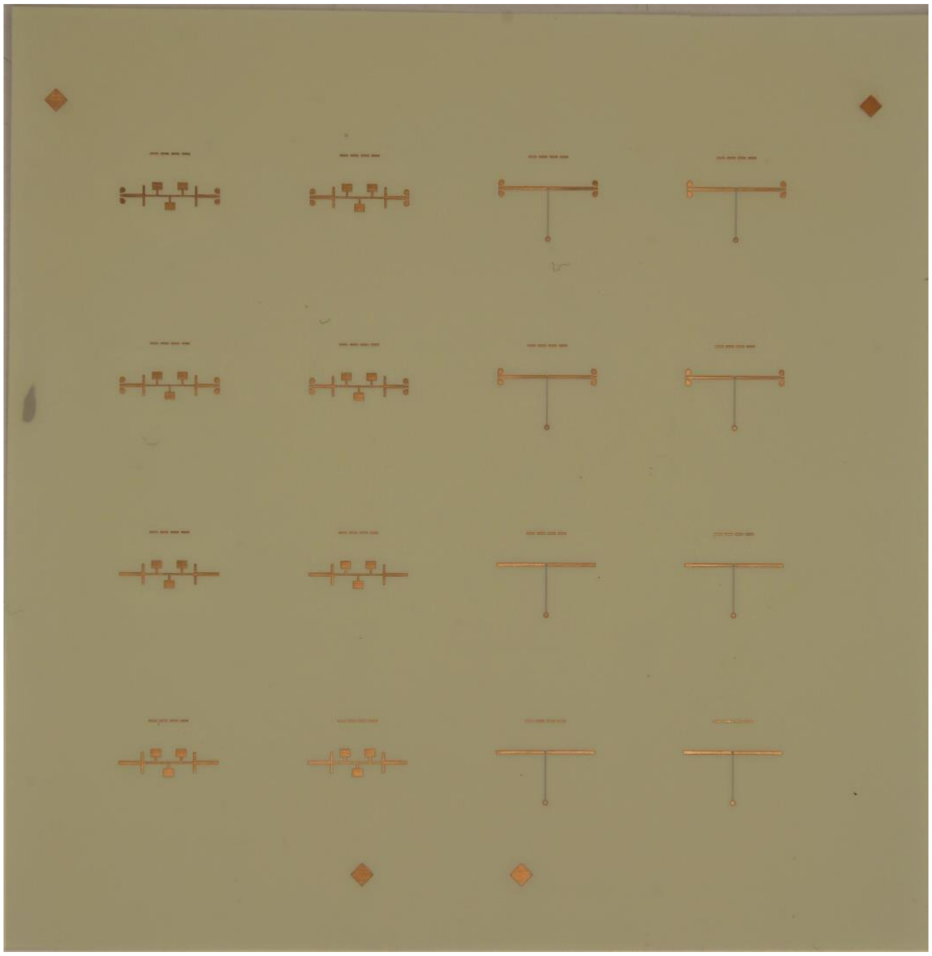

Figure 90: Panel with a subset of filters fabricated by MSU

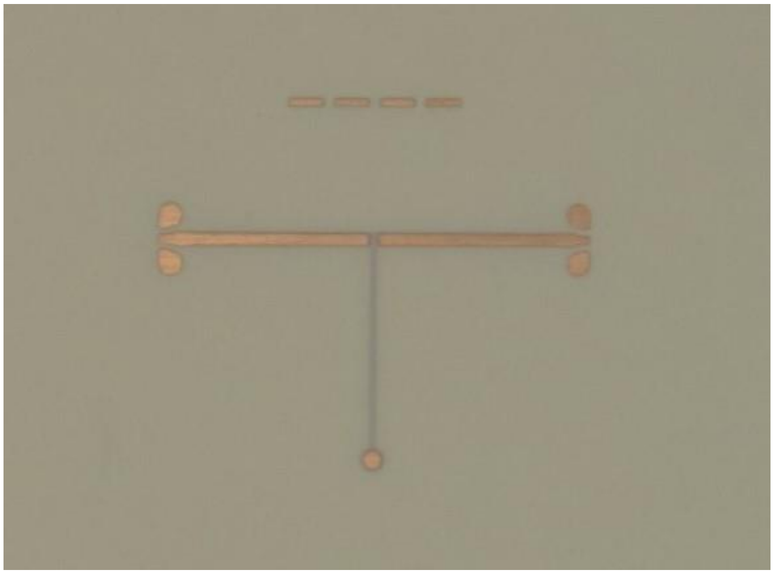

Figure 91: First-pass band-pass filter, fabricated by MSU Consortium members

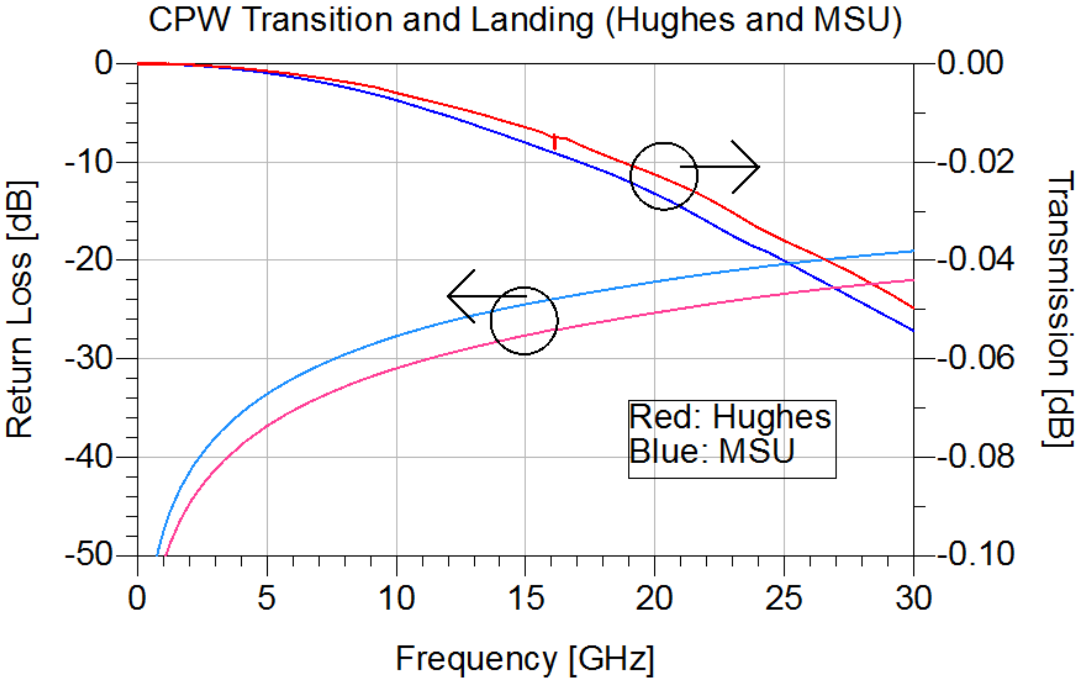

Figure 92: EM-simulated comparison of CPW Transition layout for MSU fabrication

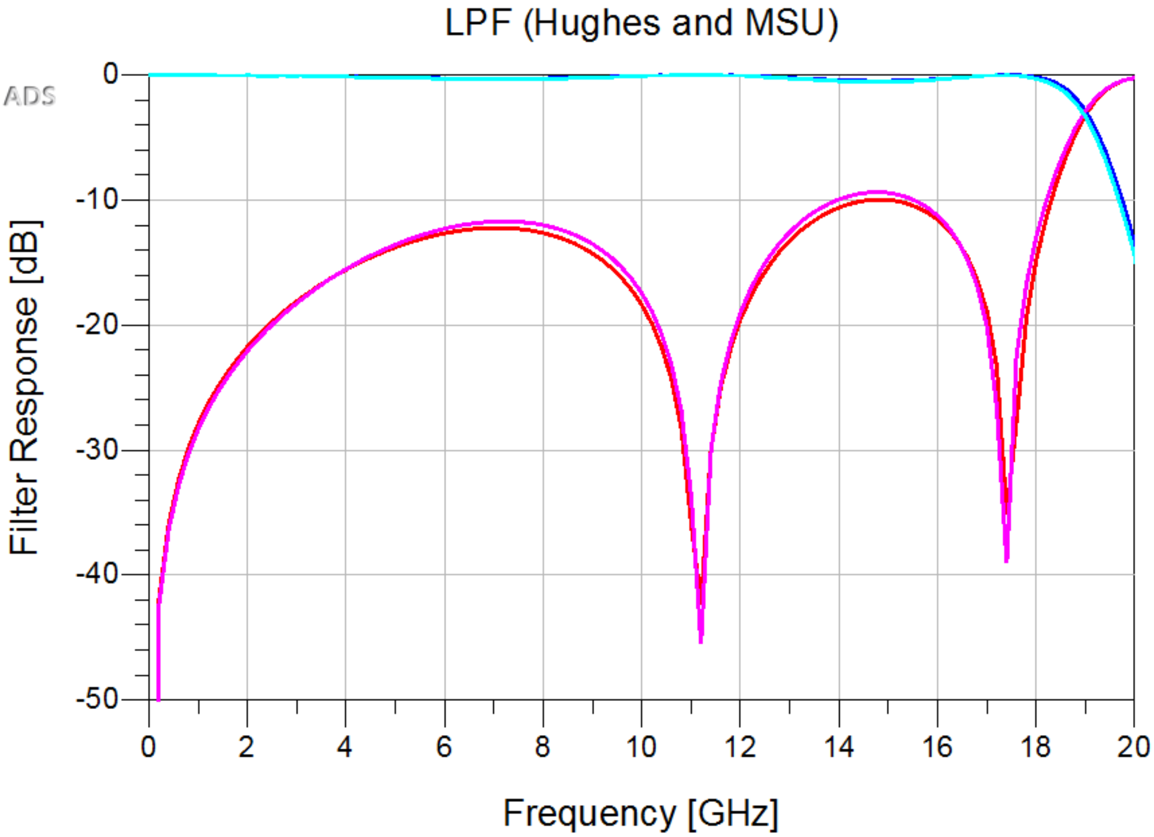

Figure 93: EM-simulated comparison of lowpass filters for MSU fabrication

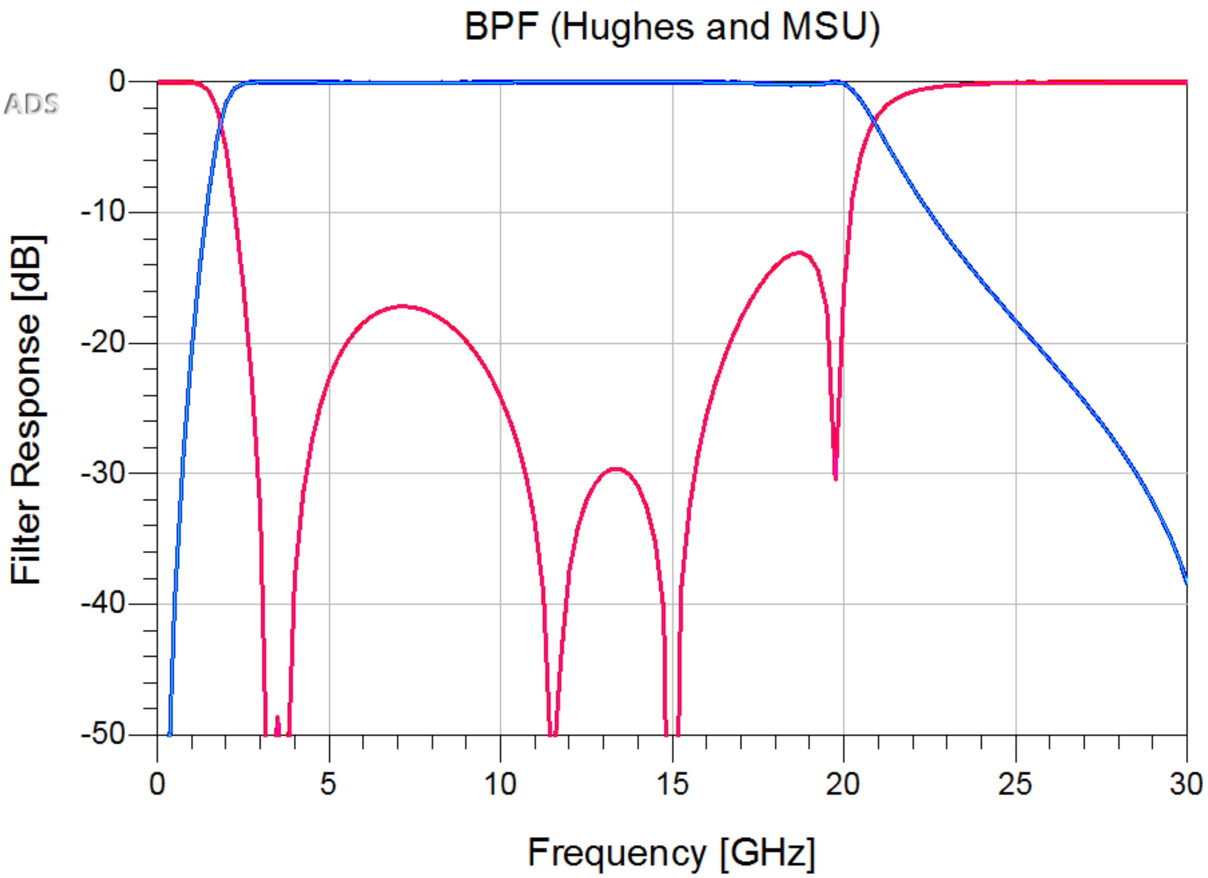

Figure 94: EM-simulated comparison of bandpass filter for MSU fabrication (identical simulation match)

Bibliography

[1] B. Panzer, D. Gomez-Garcia, C. Leuschen, J. Paden, F. Rodriguez-Morales, A. Patel, T. Markus, B. Holt and P. Gogineni, "An ultra-wideband, microwave radar for measuring snow thickness on sea ice and mapping near-surface internal layers in polar firn," *Journal of Glaciology,* vol. 59, no. 214, pp. 244-254, 2013.

[2] B. Medley, S. R. M. LigtenbergI, I. Joughin, M. R. Van den Broeke, S. Gogineni and S. Nowicki, "Antarctic firn compaction rates from repeat-track airborne radar data: I. Methods," *Annals of Glaciology,* vol. 56, no. 70, pp. 155-166, 2015.

[3] R. L. Hawley, E. M. Morris, R. Cullen, U. Nixdorf, A. P. Shepherd and D. J. Wingham, "ASIRAS airborne radar resolves internal annual layers in the dry-snow zone of Greenland," *Geophysical Research Letters,* vol. 33, no. 4, 2006.

[4] G. Koh, N. E. Yankielun and A. I. Baptista, "SNOW COVER CHARACTERIZATION USING MULTIBAND FMCW RADARS," *Hydrological Processes,* vol. 10, no. 12, pp. 1609-1617, 1966.

[5] S. Arcone, N. Yankielun and E. Chacho, "Reflection profiling of Arctic lake ice using microwave FM-CW radar," *IEEE Transactions on Geoscience and Remote Sensing,* vol. 35, no. 2, pp. 436-443, 1997.

[6] M.-K. Olkkonen, "Ku band ground penetrating radar for asphalt layer measurement," *IET Radar, Sonar & Navigation,* vol. 10, no. 1, pp. 76-81, 2016.

[7] D. Gomez-Garcia, F. Rodriguez-Morales, C. Leuschen and S. Welch, "High-Throughput Phenotyping of Wheat Canopy Height using Ultra-Wideband Radar: First Results," *IEEE Transactions on Geoscience and Remote Sensing*, 2019 (in press).

[8] J.-B. Yan, S. Gogineni, F. Rodriguez-Morales, D. Gomez-Garcia, J. Paden, J. Li, C. Leuschen, D. A. Braaten, J. A. Richter-Menge, S. L. Farrell, J. Brozena and R. D. Hale, "Airborne Measurements of Snow Thickness: Using ultrawide-band frequency-modulated-continuous-wave radars," *IEEE Geoscience and Remote Sensing Magazine*, vol. 5, no. 2, pp. 57-76, 2017.

[9] P. G. Smith, "Leakage rejection in Beam-Switched CW Radars," *IRE Transactions on Aerospace and Navigational Electronics,* Vols. ANE-9, no. 4, pp. 241-250, 1962.

[10] H.-P. Marshall and G. Koh, "FMCW radars for snow research," *Cold Regions Science and Technology,* vol. 52, no. 2, pp. 118-131, 2008.

[11] S. Blunt, C. Allen, E. Arnold, R. Hale, R. Hui, S. Keshmiri, C. Leuschen, J. Li, J. Paden, F. Rodriguez-Morales, A. Salandrino and J. Stiles, "Radar Research at the University of Kansas," in *SPIE Radar Sensor Technology XXI Converence*, Anaheim, 2017.

[12] S. Krishann, "Modeling and simulation analysis of an FMCW radar for measuring snow thickness," M.S. Thesis, University of Kansas, Lawrence, 2000.

[13] S. Gogineni, K. Wong, S. Krishnan, P. Kanagaratnam, T. Markus and V. Lytle, "An ultra-wideband radar measurements of snow thickness over sea ice," in *2003 IEEE International*

Geoscience and Remote Sensing Symposium. Proceedings (IEEE Cat. No.03CH37477), Toulouse, 2003.

[14] P. Kanagaratnam, T. Markus, V. Lytle, B. Heavey, P. Jansen, G. Prescott and S. Gogineni, "Ultrawideband Radar Measurements of Thickness of Snow Over Sea Ice," *IEEE Transactions on Geoscience and Remote Sensing*, vol. 45, no. 9, pp. 2715-2724, 2007.

[15] R. Willyard, "Airborne radar for measuring snow thickness over sea ice," M.S. Thesis, University of Kansas, Lawrence, 2007.

[16] N. Galin, A. Worby, T. Markus, C. Leuschen and P. Gogineni, "Validation of Airborne FMCW Radar Measurements of Snow Thickness Over Sea Ice in Antarctica," *IEEE Transactions on Geoscience and Remote Sensing*, vol. 50, no. 1, pp. 3-12, 2011.

[17] A. Patel, "Signal Generation for FMCW Ultra-Wideband Radar," M.S. Thesis, University of Kansas, Lawrence, 2009.

[18] D. Gomez-Garcia, F. Rodriguez-Morales, C. Leuschen and S. Gogineni, "KU-Band radar altimeter for surface elevation measurements in polar regions using a wideband chirp generator with improved linearity," in *2012 IEEE International Geoscience and Remote Sensing Symposium*, Munich, 2012.

[19] D. Gomez-Garcia, C. Leuschen, F. Rodriguez-Morales, J.-B. Yan and P. Gogineni, "Linear chirp generator based on direct digital synthesis and frequency multiplication for airborne FMCW snow probing radar," in *2014 IEEE MTT-S International Microwave Symposium (IMS2014)*, Tampa, 2014.

[20] F. Rodriguez-Morales, "Advanced Multifrequency Radar Instrumentation for Polar Research," *IEEE Transactions on Geoscience and Remote Sensing,* vol. 52, no. 5, pp. 2824-2842, 2014.

[21] R. Kwok and C. Haas, "Effects of radar side-lobes on snow depth retrievals from Operation IceBridge," *Journal of Glaciology,* vol. 61, no. 227, pp. 576-584, 2015.

[22] T. Newman, S. L. Farrell, J. Richter-Menge, L. N. Connor, N. T. Kurtz, B. C. Elder and D. McAdoo, "Assessment of radar-derived snow depth over Arctic sea ice," *JGR Oceans,* vol. 119, no. 12, pp. 8578-8602, 2014.

[23] J. King, S. Howell, C. Derksen, N. Rutter, P. Toose, J. F. Beckers, C. Haas, N. Kurtz and J. Richter-Menge, "Evaluation of Operation IceBridge quick-look snow depth estimates on sea ice," *Geophysical Research Letters,* vol. 42, no. 21, pp. 9302-9310, 2015.

[24] K. A. Giles, S. W. Laxon, D. J. Wingham, D. W. Wallis, W. B. Krabill, C. J. Leuschen, D. McAdoo, S. S. Manizade and R. K. Raney, "Combined airborne laser and radar altimeter measurements over the Fram Strait in May 2002," *Remote Sensing of Environment,* vol. 11, no. 2,3, pp. 182-194, 2007.

[25] J.-B. Yan, D. G.-G. Alvestegui, J. W. McDaniel, Y. Li, S. Gogineni, F. Rodriguez-Morales and C. J. Leuschen, "Ultrawideband FMCW Radar for Airborne Measurements of Snow Over Sea Ice and Land," *IEEE Transactions on Geoscience and Remote Sensing* , vol. 55, no. 2, pp. 834-843, 2016.

[26] J. B. Yan, S. Gogineni, D. Braaten, J. Brozena, F. Rodriguez-Morales and E. Arnold, "Ultra-wideband radars operating over the frequency range of 2-18 GHZ for measurements on terrestrial snow and ice," in *2016 IEEE International Geoscience and Remote Sensing Symposium (IGARSS)*, Beijing, 2016.

[27] J. McDaniel, S. Yan and S. Gogineni, "Design, Integration, and Miniaturization of a Multi-channel Ultrawide-band (UWB) Snow Radar Receiver for Airborne Remote Sensing," *Microwave Journal,* vol. 59, no. 4, pp. 20-28, 2016.

[28] A. Jutila, R. Ricker, S. Hendricks, J. Paden, J. King, C. Polashenski, B. Lange, C. Michel and C. Haas, "Snow depth on Arctic sea ice derived from airborne radar measurements," in *IGS Sea Ice Symposium: Sea Ice at the Interface*, Winnipeg, 2019.

[29] S. Kaundinya, E. Arnold, F. Rodriguez-Morales and A. Patil, "A UAS-based ultra-wideband radar system for soil moisture measurements," in *2018 IEEE Radar Conference (RadarConf18),* Oklahoma City, 2018.

[30] F. Rodriguez-Morales, C. Leuschen, C. Carabajal, J. Paden, J. A. Wolf, S. Garrison and J. McDaniel, "An Improved UWB Microwave Radar for Very Long-Range Measurements of Snow Cover," *IEEE Transactions on Instrumentation and Measurement,* in press.

[31] R. O. R. Jenssen, M. Eckerstorfer and S. Jacobsen, "Drone-Mounted Ultrawideband Radar for Retrieval of Snowpack Properties," *IEEE Transactions on Instrumentation and Measurement*, vol. 69, no. 1, pp. 221-230, 2019.

[32] M. J. Øyan, S.-E. Hamran, L. Damsgård and T. Berger, "Sounder, Compact Airborne C-Band Radar," *IEEE Transactions on Geoscience and Remote Sensing,* vol. 52, no. 10, pp. 6326-6332, 2014.

[33] Y. Kim, T. J. Reck, M. Alfonso-delPino and T. H. Painter, "A Ku-Band CMOS FMCW Radar Transceiver for Snowpack Remote Sensing," *IEEE Transactions on Microwave Theory and Techniques,* vol. PP, no. 99, pp. 1-15, 2018.

[34] C. J. Li and H. Ling, "High-resolution, downward-looking radar imaging using a small consumer drone," in *2016 IEEE International Symposium on Antennas and Propagation (APSURSI)*, Fajardo, 2016.

[35] S. Dill, E. Schreiber, M. Engel, A. Heinzel and M. Peichl, "A drone carried multichannel Synthetic Aperture Radar for advanced buried object detection," in *2019 IEEE Radar Conference (RadarConf)*, Boston, 2019.

[36] F. Rodriguez-Morales, J. McDaniel, C. Carabajal, A. Paden, C. Leuschen, A. Wolf and S. Garrison, "Prototyping an UWB Airborne Radar for Snow Probing Using Modular Building Blocks," *Microwave Journal,* pp. 78-90, Sept, 2019.

[37] K. Carr, "Development of a Multichannel Wideband Radar Demonstrator," M.S. Thesis, University of Kansas, Lawrence, 2019.

[38] J. McDaniel, "Design, Integration, and Miniaturization of a Multichannel Ultra-Wideband Snow Radar Receiver and Passive Microwave Components," M.S. Thesis, University of Kansas, Lawrence, 2015.

[39] J. McDaniel, J. Yan and P. Gogineni, "Super-wideband cascaded bandpass filter using suspended substrate stripline technology," *Microwave and Optical Technology Letters,* vol. 61, no. 6, pp. 1491-1499, 2019.

[40] J. W. McDaniel, S. Saeedi, M. B. Yeary and H. H. Sigmarsson, "A Low-Loss Fully Board-Integrated Low-Pass Filter Using Suspended Integrated Strip-Line Technology," *IEEE Transactions on Components, Packaging and Manufacturing Technology,* vol. 8, no. 11, pp. 1948-1955, 2018.

[41] C. Oakley, J. D. Albrecht, J. Papapolymerou and P. Chahal, "Low-Loss Aerosol-Jet Printed Wideband Interconnects for Embedded Devices," *IEEE Transactions on Components, Packaging and Manufacturing Technology*, vol. 9, no. 11, pp. 2305-2313, 2019.

[42] F. Cai, Y.-H. Chang, K. Wang, C. Zhang, B. Wang and J. Papapolymerou, "Low-Loss 3-D Multilayer Transmission Lines and Interconnects Fabricated by Additive Manufacturing Technologies," *IEEE Transactions on Microwave Theory and Techniques,* vol. 64, no. 10, pp. 3208-3216, 2016.

[43] Z.-C. Hao and J.-S. Hong, "Ultra-Wideband Bandpass Filter Using Multilayer Liquid-Crystal-Polymer Technology," *IEEE Transactions on Microwave Theory and Techniques,* vol. 56, no. 9, pp. 2095-2100, 2008.

[44] Z.-C. Hao and J.-S. Hong, "Ultra Wideband Bandpass Filter Using Embedded Stepped Impedance Resonators on Multilayer Liquid Crystal Polymer Substrate," *IEEE Microwave and Wireless Components Letters,* vol. 18, no. 9, pp. 581-583, 2008.

[45] Z.-C. Hao and J.-S. Hong, "UWB Bandpass Filter Using Cascaded Miniature High-Pass and Low-Pass Filters With Multilayer Liquid Crystal Polymer Technology," *IEEE Transactions on Microwave Theory and Techniques,* vol. 58, no. 4, pp. 941-948, 2010.

[46] Y. Lan, Y. Xu, C. Wang, Z. Wen, Y. Qiu, T. Mei, Y. Wu and R. Xu, "Flexible microwave filters on ultra thin Liquid Crystal Polymer substrate," in *2015 IEEE MTT-S International Microwave Symposium*, Phoenix, 2015.

[47] R. Bairavasubramanian and J. Papapolymerou, "Fully Canonical Pseudo-Elliptic Bandpass Filters on Multilayer Liquid Crystal Polymer Technology," *IEEE Microwave and Wireless Components Letters,* vol. 17, no. 3, pp. 190-192, 2007.

[48] Y. Lan, Y. Xu, C. Wang, Z. Wen, Y. Qiu, T. Mei, Y. Wu and R. Xu, "X-band flexible bandpass filter based on ultra-thin liquid crystal polymer substrate," *Electronics Letters,* vol. 51, no. 4, pp. 345-347, 2015.

[49] Z.-C. Hao, J.-S. Hong and S. K. Alotaibi, "A novel Ultra Wideband Bandpass Filter using Broadside Coupled Structures on Multilayer Organic Liquid Crystal Polymer Substrate," in *2008 38th European Microwave Conference*, Amsterdam, 2008.

[50] S. Almorqi, H. Shaman and A. Alamoudi, "Parallel-coupled stub-loaded resonator bandpass filter with ultra-wideband passband on multilayer liquid crystal polymer substrates," *International Journal of Microwave and Wireless Technologies,* pp. 1-4, July 2015.

[51] H. Shaman, S. Almorqi and A. AlAmoudi, "Ultra-wideband (UWB) Bandpass Filter with Cascaded Lowpass Filter on Multilayer Liquid-Crystal Polymer (LCP) Substrate," *IETE Journal of Research,* vol. 62, no. 1, pp. 63-67, 2016.

[52] H. Shaman, S. Almorqi and A. AlAmoudi, "Composite microstrip lowpass filter with ultrawide stopband and low insertion loss," *Microwave and Optical Technology Letters,* vol. 57, no. 4, pp. 871-874, 2015.

[53] J. O. S. III, "Hann or Hanning or Raised Cosine," CCRMA Stanford, 26 July 2020. [Online]. Available: https://ccrma.stanford.edu/~jos/sasp/Hann_Hanning_Raised_Cosine.html. [Accessed 14 August 2020].

[54] J. McDaniel, F. Morales, C. Leuschen, A. Feathers, J. A. Wolf and S. Garrison, "Packaging and Miniaturization of a 2-18 GHz UWB Radar for Measurements of Snow and Ice: Initial Results," in *International Microelectronics Assembly and Packaging (IMAPS),* Raleigh, 2017.

[55] R. Page and J. Richardson, "Designing with Modular Filters," X-Microwave.

[56] R. Sturdivant, "Microwave and Millimeter-Wave Electronic Packaging," Artech House, 2013.

[57] H. Madhav, "Modular Frequency Multiplier and Filters for the NASA Global Hawk Snow Radar," M.S. Thesis, University of Kansas, Lawrence, 2017.

[58] Qorvo, *TGA2567-SM datasheet,* 2019.

[59] Qorvo, *TGA2214 datasheet*, 2019.

[60] Hittite Microwave Corporation, *HMC980LP4E Active Bias Controller datasheet.*

[61] Analog Devices, *HMC606 GaAs InGaP HBT MMIC Ultra Low Phase Noise, Distributed Amplifier datasheet.*

[62] J.-S. G. Hong and M. J. Lancaster, Microstrip Filters for RF / Microwave Applications, John Wiley & Sons, 2004.

[63] S. A. A. Alseyab, "Design Methods for Microwave Filters and Multiplexers," Ph.D Dissertation, University of Leeds, 1979.

[64] Panasonic Corporation, *lexible circuit board materials LCP(Liquid Crystal Polymer) FELIOS LCP R-F705S datasheet.*

[65] H. A. Wheeler, "Transmission-Line Properties of a Strip on a Dielectric Sheet on a Plane," *IEEE Transactions on Microwave Theory and Techniques*, vol. 25, no. 8, pp. 631-647, 1977.

[66] E. O. Hammerstad, "Equations for Microstrip Circuit Design," in *1975 5th European Microwave Conference*, Hamburg, 1975.

[67] R. O'Rourke, "3D Electromagnetic Simulation vs. Planar MoM," *Microwave Journal*, 2016.

[68] G. A. E. Vandenbosch and A. Vasylchenko, "A Practical Guide to 3D Electromagnetic Software Tools," 2009.

[69] H. M. Talasila, F. R. Morales, J. Paden, N. Orloff, D. Gu, M. Conte, C. Oakley and M. McKeown, "First Pass Design of Ultra-Wideband Microwave and mm-Wave Filters for Multistage Frequency Multiplication," *Microwave Journal*, 2019.

[70] B. C. Wadell, Transmission Line Design Handbook, Artech House, 1991.

[71] E. M. Jones, G. L. Matthaei and L. Young, Microwave Filters, Impedance-Matching Networks, and Coupling Structures, Artech House, 1964.

[72] M. Akra, E. Pistono, H. Issa, A. Jrad and P. Ferrari, "Full Study of the Parallel-Coupled Stub-Loaded Resonator: Synthesis Method in a Narrow Band With an Extended Optimal Rejection Bandwidth," *IEEE Transactions on Microwave Theory and Techniques* , vol. 62, no. 12, pp. 3380-3392, 2014.

[73] D.-S. La, S.-Q. Jia and L. Cheng, "Microstrip parallel-coupled line wideband bandpass filter using e-shape resonator," in *2017 Sixth Asia-Pacific Conference on Antennas and Propagation (APCAP)*, Xi'an, 2017.

[74] K. Srisathit and W. Surakumpontorn, "Wideband microstrip bandpass filter based on modified parallel-coupled line topology," in *2010 10th International Symposium on Communications and Information Technologies*, Tokyo, 2010.

[75] H. Zhu and Q.-X. Chu, "Compact Ultra-Wideband (UWB) Bandpass Filter Using Dual-Stub-Loaded Resonator (DSLR)," *IEEE Microwave and Wireless Components Letters,* vol. 23, no. 10, pp. 527-529, 2013.

[76] Y. Lan, Y. Xu, M. Tengda and Y. Wu, "A 2∼18GHz compact microwave band-pass filter suitable for planar and three-dimension flexible integration," in *2016 46th European Microwave Conference (EuMC)*, London, 2016.

[77] M. Makimoto and S. Yamashita, Microwave Resonators and Filters for Wireless Communication: Theory, Design and Application, Springer Science & Business Media, 2001.

[78] M. Akra, E. Pistono, A. Jrad, H. Issa and P. Ferrari, "Synthesis method for the parallel-coupled stub-loaded resonator filters," in *2014 IEEE MTT-S International Microwave Symposium (IMS2014)*, Tampa, 2014.

[79] M. Akra, H. Issa, E. Pistono, A. Jrad, N. Corrao and P. Ferrari, "Parallel-coupled Stub-loaded Resonator filters with wide spurious suppression," in *2012 42nd European Microwave Conference*, Amsterdam, 2012.

[80] C.-P. Chien, A. Burnett, J. Cech and M. Tanielian, "The signal transmission characteristics of embedded microstrip transmission lines over a meshed ground plane in copper/polyimide multichip module," *IEEE Transactions on Components, Packaging, and Manufacturing Technology: Part B,* vol. 17, no. 4, pp. 578-583, 1994.

[81] Optimum Design Associates, "Embedded Microstrip Transmission Lines in RF PCB Design," Optimum Design Associates.

[82] M. Tran and C. Nguyen, "Modified broadside-coupled microstrip lines suitable for MIC and MMIC applications and a new class of broadside-coupled band-pass filters," *IEEE Transactions on Microwave Theory and Techniques,* vol. 41, no. 8, pp. 1336-1342, 1993.

[83] M. Steer, Microwave and RF Design, a Systems Approach, SciTech Publishing, Incorporated, 2008.

[84] T. Rink, P. Kanagaratnam, D. Braaten, T. Akins and S. Gogineni, "A Wideband Radar for Mapping Near-Surface Layers in Snow," in *2006 IEEE International Symposium on Geoscience and Remote Sensing*, Denver, 2006.

[85] N. Galin, A. Worby, R. Massom, G. Brooker, C. Leuschen, S. Gogineni and P. Jansen, "2 – 8 GHz FMCW radar for estimating snow depth on antarctic sea ice," in *2008 International Conference on Radar*, Adelaide, 2008.

Appendix A: Filter Layout Automation Matlab Script

```
clear, clc;
close all;

w = 0.01; %wire width, mm
wdim = 0.05;
viaw = 0.01;

%Here, change between _lpf and _bpf to read and write to correct files
% Read excel spreadsheet
inData = readtable('filter_variables_bpf.xlsx','Range','A1:R33');
% Specify script file
fileID = fopen('gen_filters_bpf.scr','w');

% Define variables
L1 = inData.L1;
L2 = inData.L2;
W1 = inData.W1;
W2 = inData.W2;
W3 = inData.W3;
L3 = inData.L3;
WS = inData.WS;
LL = inData.LL;
LL1 = inData.LL1;
WL = inData.WL;
WL1 = inData.WL1;
LH = inData.LH;
LH1 = inData.LH1;
WH = inData.WH;
WH1 = inData.WH1;
label = inData.text;

viaEx = 0.560/2;
orig_space = 18;
dimX = 10;
dimY = 10;
c2edge_clear = 0.25;
launchDim = dimX/2 - c2edge_clear;
ustripW = 0.34;
launchW = 0.24;

% Define CPW sides here as array each
cpwStart = [-launchDim, 0.2; launchDim, 0.2; -launchDim, -0.2; launchDim, -
0.2];
cpwSides = zeros(6,2,4); %  6 points. x,y. 4 sections to process
cpwSidesInit = [0 0; 0 .32; .28 .32; .28 .04; .25 .04; .25 0];
cpwSidesInit = cpwSidesInit + [-launchDim*ones(6,1), 0.21*ones(6,1)];
cpwViaLocInit = cpwSidesInit(1,:,1) + [0.28, 0.32];
cpwViaLoc = zeros(2,4);
cpwMulti = ones(6,2,4);
for q = 0:3
    cpwMulti(:,:,q+1) = cpwMulti(:,:,q+1) + [zeros(6,1)-2*mod(q,2),
zeros(6,1)-2*floor(q/2)];
    cpwSides(:,:,q+1) = cpwSidesInit.*cpwMulti(:,:,q+1);
```

```
    cpwViaLoc(:,q+1) = cpwViaLocInit.*cpwMulti(1,:,q+1);
end

% Define label to be shifted
labS = 0.2;
labL = 0.8;
labA = [-labL/2, -labS/2; -labL/2, labS/2; labL/2, labS/2; labL/2, - labS/2];
labB = [-labS/2, -labL/2; -labS/2, labL/2; labS/2, labL/2; labS/2, - labL/2];
% locations relative to center of rectangle

% Draw board outline
fprintf(fileID,'grid inch 1 on\r\n');
fprintf(fileID,'layer 20\r\n');
fprintf(fileID,'wire (-0.25 -0.25) (-0.25 4.75) \r\n');
fprintf(fileID,'wire (-0.25 4.75) (7.75 4.75) \r\n');
fprintf(fileID,'wire (7.75 4.75) (7.75 -0.25) \r\n');
fprintf(fileID,'wire (7.75 -0.25) (-0.25 -0.25) \r\n');

% draw ground plane
fprintf(fileID,'layer 16\r\n');
fprintf(fileID,'polygon gnd (-0.25 -0.25) (-0.25 4.75) (7.75 4.75) (7.75 -
0.25) (-0.25 -0.25)\r\n');

% Define grid
fprintf(fileID,'grid mm 1 on\r\n');

% Giant for loop to generate script
for i = 1:length(L1)
    % Define "origin" point
    orig = orig_space*(i-1);
    % Define filter variables as array
    % mm

    % Determine filter type
    if strcmp(inData.type(i), 'BPF')
        invar = [];
        invar.L1 = L1(i);
        invar.L2 = L2(i);
        invar.W1 = W1(i);
        invar.W2 = W2(i);
        invar.W3 = W3(i);
        invar.viaEx = viaEx;

        % Translate variables into relative points
        % Top layer
        % BPF LAUNCH TYPE ===============
        % BPF USTRIP LAUNCH
        if strcmp(inData.ustrip(i), 'y')
            % Output side
            ary.T1B = [invar.W3/2, invar.W1/2 + orig];
            ary.T2B = [invar.W3/2 + invar.L1, invar.W1/2 + orig];
            ary.T3B = [invar.W3/2 + invar.L1, ustripW/2 + orig];
            ary.T4B = [launchDim, ustripW/2 + orig];
            ary.T5B = [launchDim, -ustripW/2 + orig];
            ary.T6B = [invar.W3/2 + invar.L1, -ustripW/2 + orig];
```

```
            ary.T7B = [invar.W3/2 + invar.L1, -invar.W1/2 + orig];
            ary.T8B = [invar.W3/2 -invar.W1/2 + orig];

            % Input side
            ary.T1A = [-invar.W3/2, invar.W1/2 + orig];
            ary.T2A = [-invar.W3/2 - invar.L1, invar.W1/2 + orig];
            ary.T3A = [-invar.W3/2 - invar.L1, ustripW/2 + orig];
            ary.T4A = [-launchDim, ustripW/2 + orig];
            ary.T5A = [-launchDim, -ustripW/2 + orig];
            ary.T6A = [-invar.W3/2 - invar.L1, -ustripW/2 + orig];
            ary.T7A = [-invar.W3/2 - invar.L1, -invar.W1/2 + orig];
            ary.T8A = [-invar.W3/2 -invar.W1/2 + orig];
        else %BPF CPW LAUNCH
            % Output side
            ary.T1B = [invar.W3/2, invar.W1/2 + orig];
            ary.T2B = [invar.W3/2 + invar.L1, invar.W1/2 + orig];
            ary.T3B = [invar.W3/2 + invar.L1, ustripW/2 + orig];
            ary.T4B = [launchDim - 0.4, ustripW/2 + orig];
            ary.T5B = [launchDim - 0.25, launchW/2 + orig];
            ary.T6B = [launchDim, launchW/2 + orig];
            ary.T7B = [launchDim, -launchW/2 + orig];
            ary.T8B = [launchDim - 0.25, -launchW/2 + orig];
            ary.T9B = [launchDim - 0.4, -ustripW/2 + orig];
            ary.T10B = [invar.W3/2 + invar.L1, -ustripW/2 + orig];
            ary.T11B = [invar.W3/2 + invar.L1, -invar.W1/2 + orig];
            ary.T12B = [invar.W3/2, -invar.W1/2 + orig];

            % Input side
            ary.T1A = [-invar.W3/2, invar.W1/2 + orig];
            ary.T2A = [-invar.W3/2 - invar.L1, invar.W1/2 + orig];
            ary.T3A = [-invar.W3/2 - invar.L1, ustripW/2 + orig];
            ary.T4A = [-launchDim + 0.4, ustripW/2 + orig];
            ary.T5A = [-launchDim + 0.25, launchW/2 + orig];
            ary.T6A = [-launchDim, launchW/2 + orig];
            ary.T7A = [-launchDim, -launchW/2 + orig];
            ary.T8A = [-launchDim + 0.25, -launchW/2 + orig];
            ary.T9A = [-launchDim + 0.4, -ustripW/2 + orig];
            ary.T10A = [-invar.W3/2 - invar.L1, -ustripW/2 + orig];
            ary.T11A = [-invar.W3/2 - invar.L1, -invar.W1/2 + orig];
            ary.T12A = [-invar.W3/2, -invar.W1/2 + orig];
        end

        % Internal Layer
        ary.M1 = [-invar.W3/2 - invar.L1, invar.W2/2 + orig];
        ary.M2 = [invar.W3/2 + invar.L1,  invar.W2/2 + orig];
        ary.M3 = [invar.W3/2 + invar.L1, -invar.W2/2 + orig];
        ary.M4 = [invar.W3/2, - invar.W2/2 + orig];
        ary.M5 = [invar.W3/2, - invar.W2/2 - invar.L2 - invar.viaEx + orig];
        % M6 - M9 removed for change to circular anti-pad

        ary.M10 = [-invar.W3/2, - invar.W2/2 - invar.L2  - invar.viaEx+
orig];
        ary.M11 = [-invar.W3/2, - invar.W2/2 + orig];
        ary.M12 = [-invar.W3/2 - invar.L1, -invar.W2/2 + orig];
        ary.via = [0, -invar.W2/2 - invar.L2 - invar.viaEx + orig];
```

```
        % Generate temporary string equivalent coordinates
        % Convert each of the three above sections into matrices for simple
access
        if strcmp(inData.ustrip(i), 'y')
            A = [ary.T1A; ary.T2A; ary.T3A; ary.T4A; ary.T5A; ary.T6A;
ary.T7A; ary.T8A];
            B = [ary.T1B; ary.T2B; ary.T3B; ary.T4B; ary.T5B; ary.T6B;
ary.T7B; ary.T8B];
        else
            A = [ary.T1A; ary.T2A; ary.T3A; ary.T4A; ary.T5A; ary.T6A;
ary.T7A; ary.T8A; ary.T9A; ary.T10A; ary.T11A; ary.T12A];
            B = [ary.T1B; ary.T2B; ary.T3B; ary.T4B; ary.T5B; ary.T6B;
ary.T7B; ary.T8B; ary.T9B; ary.T10B; ary.T11B; ary.T12B];
        end
        M = [ary.M1; ary.M2; ary.M3; ary.M4; ary.M5; ary.M10; ary.M11;
ary.M12];

        % Script generation
        % Set layer
        fprintf(fileID,'layer 1\r\n');

        % output side
        fprintf(fileID,'polygon %4.3f ',w);
        % coordinates for A array
        if strcmp(inData.ustrip(i), 'y')  %microstrip on output
            formatSpec = '(%4.3f %4.3f) (%4.3f %4.3f) (%4.3f %4.3f) (%4.3f
%4.3f) (%4.3f %4.3f) (%4.3f %4.3f) (%4.3f %4.3f) (%4.3f %4.3f) (%4.3f
%4.3f)\r\n';

fprintf(fileID,formatSpec,A(1,:),A(2,:),A(3,:),A(4,:),A(5,:),A(6,:),A(7,:),A(
8,:),A(1,:));
        else %cpw on output
            formatSpec = ['(%4.3f %4.3f) (%4.3f %4.3f) (%4.3f %4.3f) (%4.3f
%4.3f) (%4.3f %4.3f) (%4.3f %4.3f)' ...
            ' (%4.3f %4.3f) (%4.3f %4.3f) (%4.3f %4.3f) (%4.3f %4.3f) (%4.3f
%4.3f) (%4.3f %4.3f) (%4.3f %4.3f)\r\n'];

fprintf(fileID,formatSpec,A(1,:),A(2,:),A(3,:),A(4,:),A(5,:),A(6,:),A(7,:),A(
8,:),A(9,:),A(10,:),A(11,:),A(12,:),A(1,:));
        end

        % input side
        fprintf(fileID,'polygon %4.3f ',w);
        % coordinates for B array
        if strcmp(inData.ustrip(i), 'y') %microstrip on input
            formatSpec = '(%4.3f %4.3f) (%4.3f %4.3f) (%4.3f %4.3f) (%4.3f
%4.3f) (%4.3f %4.3f) (%4.3f %4.3f) (%4.3f %4.3f) (%4.3f %4.3f) (%4.3f
%4.3f)\r\n';

fprintf(fileID,formatSpec,B(1,:),B(2,:),B(3,:),B(4,:),B(5,:),B(6,:),B(7,:),B(
8,:),B(1,:));
        else %cpw on input
            formatSpec = ['(%4.3f %4.3f) (%4.3f %4.3f) (%4.3f %4.3f) (%4.3f
%4.3f) (%4.3f %4.3f) (%4.3f %4.3f)' ...
            ' (%4.3f %4.3f) (%4.3f %4.3f) (%4.3f %4.3f) (%4.3f %4.3f) (%4.3f
%4.3f) (%4.3f %4.3f) (%4.3f %4.3f)\r\n'];
```

```
fprintf(fileID,formatSpec,B(1,:),B(2,:),B(3,:),B(4,:),B(5,:),B(6,:),B(7,:),B(
8,:),B(9,:),B(10,:),B(11,:),B(12,:),B(1,:));
        end

        % middle layer
        fprintf(fileID,'layer 2\r\n');
        fprintf(fileID,'polygon gnd %4.3f ',w);
        % coordinates for M array
        formatSpec = ['(%4.3f %4.3f) (%4.3f %4.3f) (%4.3f %4.3f) (%4.3f
%4.3f) (%4.3f %4.3f) (%4.3f %4.3f)' ...
        ' (%4.3f %4.3f) (%4.3f %4.3f) (%4.3f %4.3f)\r\n'];

fprintf(fileID,formatSpec,M(1,:),M(2,:),M(3,:),M(4,:),M(5,:),M(6,:),M(7,:),M(
8,:),M(1,:));

        %draw via
        fprintf(fileID,'via ''gnd'' %4.3f round (%4.3f %4.3f)\r\n', viaw,
ary.via);
        %draw antipad
        fprintf(fileID,'change width 0.41\r\n');
        antipadLoc = [0, - invar.W2/2 - invar.L2 - invar.viaEx + orig];
        formatSpec = 'circle (%4.3f %4.3f) (%4.3f %4.3f)\r\n';
        fprintf(fileID,formatSpec, antipadLoc, antipadLoc + [0, 0.08]);


    else % LPFs INSTEAD
=============================================================================
============
        %
=============================================================================
==========================

        invar = [];
        invar.L1 = L1(i);
        invar.L2 = L2(i);
        invar.L3 = L3(i);
        invar.W1 = W1(i);
        invar.WS = WS(i);
        invar.LL = LL(i);
        invar.LL1 = LL1(i);
        invar.WL = WL(i);
        invar.WL1 = WL1(i);
        invar.LH = LH(i);
        invar.LH1 = LH1(i);
        invar.WH = WH(i);
        invar.WH1 = WH1(i);

        %translate variables into coordinates for polygon function
        if strcmp(inData.ustrip(i), 'y')
            ary.p1 = [-invar.WH1/2 - invar.L3 - invar.WH - invar.L2 -
invar.W1, -invar.L1 + orig];

            ary.pA = [-invar.WH1/2 - invar.L3 - invar.WH - invar.L2 -
invar.W1, -ustripW/2 + orig];
```

```
            ary.pB = [-launchDim, -ustripW/2 + orig];
            ary.pC = [-launchDim, ustripW/2 + orig];
            ary.pD = [-invar.WH1/2 - invar.L3 - invar.WH - invar.L2 -
invar.W1, ustripW/2 + orig];

            ary.p2 = [-invar.WH1/2 - invar.L3 - invar.WH - invar.L2 -
invar.W1, invar.L1 + orig];
            ary.p3 = [-invar.WH1/2 - invar.L3 - invar.WH - invar.L2, invar.L1
+ orig];
            ary.p4 = [-invar.WH1/2 - invar.L3 - invar.WH - invar.L2,
invar.WS/2 + orig];
            ary.p5 = [-invar.WH1/2 - invar.L3 - invar.WH, invar.WS/2 + orig];
            ary.p6 = [-invar.WH1/2 - invar.L3 - invar.WH, invar.WS/2 +
invar.LH + orig];
            ary.p7 = [-invar.WH1/2 - invar.L3 - invar.WL/2 - invar.WH/2,
invar.WS/2 + invar.LH + orig];
            ary.p8 = [-invar.WH1/2 - invar.L3 - invar.WL/2- invar.WH/2,
invar.WS/2 + invar.LH + invar.LL + orig];
            ary.p9 = [-invar.WH1/2 - invar.L3 + invar.WL/2- invar.WH/2,
invar.WS/2 + invar.LH + invar.LL + orig];
            ary.p10 = [-invar.WH1/2 - invar.L3 + invar.WL/2- invar.WH/2,
invar.WS/2 + invar.LH + orig];
            ary.p11 = [-invar.WH1/2 - invar.L3, invar.WS/2 + invar.LH +
orig];
            ary.p12 = [-invar.WH1/2 - invar.L3, invar.WS/2 + orig];
            ary.p13 = [invar.WH1/2 + invar.L3, invar.WS/2 + orig];
            ary.p14 = [invar.WH1/2 + invar.L3, invar.WS/2 + invar.LH + orig];
            ary.p15 = [invar.WH1/2 + invar.L3 + invar.WH/2 - invar.WL/2,
invar.WS/2 + invar.LH + orig];
            ary.p16 = [invar.WH1/2 + invar.L3 + invar.WH/2 - invar.WL/2,
invar.WS/2 + invar.LH + invar.LL + orig];
            ary.p17 = [invar.WH1/2 + invar.L3 + invar.WH/2 + invar.WL/2,
invar.WS/2 + invar.LH + invar.LL + orig];
            ary.p18 = [invar.WH1/2 + invar.L3 + invar.WH/2 + invar.WL/2,
invar.WS/2 + invar.LH + orig];
            ary.p19 = [invar.WH1/2 + invar.L3 + invar.WH, invar.WS/2 +
invar.LH + orig];
            ary.p20 = [invar.WH1/2 + invar.L3 + invar.WH, invar.WS/2 + orig];
            ary.p21 = [invar.WH1/2 + invar.L3 + invar.WH + invar.L2,
invar.WS/2 + orig];
            ary.p22 = [invar.WH1/2 + invar.L3 + invar.WH + invar.L2, invar.L1
+ orig];
            ary.p23 = [invar.WH1/2 + invar.L3 + invar.WH + invar.L2 +
invar.W1, invar.L1 + orig];

            ary.pE = [invar.WH1/2 + invar.L3 + invar.WH + invar.L2 +
invar.W1, ustripW/2 + orig];
            ary.pF = [launchDim, ustripW/2 + orig];
            ary.pG = [launchDim, -ustripW/2 + orig];
            ary.pH = [invar.WH1/2 + invar.L3 + invar.WH + invar.L2 +
invar.W1, -ustripW/2 + orig];

            ary.p24 = [invar.WH1/2 + invar.L3 + invar.WH + invar.L2 +
invar.W1, -invar.L1 + orig];
            ary.p25 = [invar.WH1/2 + invar.L3 + invar.WH + invar.L2, -
invar.L1 + orig];
```

```
            ary.p26 = [invar.WH1/2 + invar.L3 + invar.WH + invar.L2, -
invar.WS/2 + orig];
            ary.p27 = [invar.WH1/2, -invar.WS/2 + orig];
            ary.p28 = [invar.WH1/2, -invar.WS/2 - invar.LH1 + orig];
            ary.p29 = [invar.WL1/2, -invar.WS/2 - invar.LH1 + orig];
            ary.p30 = [invar.WL1/2, -invar.WS/2 - invar.LH1 - invar.LL1 +
orig];
            ary.p31 = [-invar.WL1/2, -invar.WS/2 - invar.LH1 - invar.LL1 +
orig];
            ary.p32 = [-invar.WL1/2, -invar.WS/2 - invar.LH1 + orig];
            ary.p33 = [-invar.WH1/2, -invar.WS/2 - invar.LH1 + orig];
            ary.p34 = [-invar.WH1/2, -invar.WS/2 + orig];
            ary.p35 = [-invar.WH1/2 - invar.L3 - invar.WH - invar.L2, -
invar.WS/2 + orig];
            ary.p36 = [-invar.WH1/2 - invar.L3 - invar.WH - invar.L2, -
invar.L1 + orig];

            % --------------- SCRIPT GENERATION ------------------------------
--------%

            % Generate eagle script

            % Set layer
            fprintf(fileID,'layer 1\r\n');

            % First command line
            fprintf(fileID,'polygon %4.3f ',w);
            % coordinates live here...
            formatSpec = ['(%4.3f %4.3f) (%4.3f %4.3f) (%4.3f %4.3f) (%4.3f
%4.3f) (%4.3f %4.3f) ' ...
                '(%4.3f %4.3f) (%4.3f %4.3f) (%4.3f %4.3f) (%4.3f %4.3f)
(%4.3f %4.3f) ' ...
                '(%4.3f %4.3f) (%4.3f %4.3f) (%4.3f %4.3f) (%4.3f %4.3f)
(%4.3f %4.3f) ' ...
                '(%4.3f %4.3f) (%4.3f %4.3f) (%4.3f %4.3f) (%4.3f %4.3f)
(%4.3f %4.3f) ' ...
                '(%4.3f %4.3f) (%4.3f %4.3f) (%4.3f %4.3f) (%4.3f %4.3f)
(%4.3f %4.3f) ' ...
                '(%4.3f %4.3f) (%4.3f %4.3f) (%4.3f %4.3f) (%4.3f %4.3f)
(%4.3f %4.3f) ' ...
                '(%4.3f %4.3f) (%4.3f %4.3f) (%4.3f %4.3f) (%4.3f %4.3f)
(%4.3f %4.3f) ' ...
                '(%4.3f %4.3f) (%4.3f %4.3f) (%4.3f %4.3f) (%4.3f %4.3f)
(%4.3f %4.3f) ' ...
                '(%4.3f %4.3f) (%4.3f %4.3f) (%4.3f %4.3f) ' ...
                '(%4.3f %4.3f) (%4.3f %4.3f)\r\n'];

fprintf(fileID,formatSpec,ary.p1,ary.pA,ary.pB,ary.pC,ary.pD,ary.p2,ary.p3,ar
y.p4,ary.p5,ary.p6,ary.p7,ary.p8,ary.p9,ary.p10, ...

ary.p11,ary.p12,ary.p13,ary.p14,ary.p15,ary.p16,ary.p17,ary.p18,ary.p19,ary.p
20, ...

ary.p21,ary.p22,ary.p23,ary.pE,ary.pF,ary.pG,ary.pH,ary.p24,ary.p25,ary.p26,a
ry.p27,ary.p28,ary.p29,ary.p30, ...
            ary.p31,ary.p32,ary.p33,ary.p34,ary.p35,ary.p36,ary.p1);
```

```
        else % SAME THING BUT WITH CPW
LAUNCHERS=====================================

            ary.p1 = [-invar.WH1/2 - invar.L3 - invar.WH - invar.L2 -
invar.W1, -invar.L1 + orig];

            ary.pA = [-invar.WH1/2 - invar.L3 - invar.WH - invar.L2 -
invar.W1, -ustripW/2 + orig];
            ary.T4A = [-launchDim + 0.4, -ustripW/2 + orig];
            ary.T5A = [-launchDim + 0.25, -launchW/2 + orig];
            ary.T6A = [-launchDim, -launchW/2 + orig];
            ary.T7A = [-launchDim, launchW/2 + orig];
            ary.T8A = [-launchDim + 0.25, launchW/2 + orig];
            ary.T9A = [-launchDim + 0.4, ustripW/2 + orig];
            ary.pD = [-invar.WH1/2 - invar.L3 - invar.WH - invar.L2 -
invar.W1, ustripW/2 + orig];

            ary.p2 = [-invar.WH1/2 - invar.L3 - invar.WH - invar.L2 -
invar.W1, invar.L1 + orig];
            ary.p3 = [-invar.WH1/2 - invar.L3 - invar.WH - invar.L2, invar.L1
+ orig];
            ary.p4 = [-invar.WH1/2 - invar.L3 - invar.WH - invar.L2,
invar.WS/2 + orig];
            ary.p5 = [-invar.WH1/2 - invar.L3 - invar.WH, invar.WS/2 + orig];
            ary.p6 = [-invar.WH1/2 - invar.L3 - invar.WH, invar.WS/2 +
invar.LH + orig];
            ary.p7 = [-invar.WH1/2 - invar.L3 - invar.WL/2 - invar.WH/2,
invar.WS/2 + invar.LH + orig];
            ary.p8 = [-invar.WH1/2 - invar.L3 - invar.WL/2- invar.WH/2,
invar.WS/2 + invar.LH + invar.LL + orig];
            ary.p9 = [-invar.WH1/2 - invar.L3 + invar.WL/2- invar.WH/2,
invar.WS/2 + invar.LH + invar.LL + orig];
            ary.p10 = [-invar.WH1/2 - invar.L3 + invar.WL/2- invar.WH/2,
invar.WS/2 + invar.LH + orig];
            ary.p11 = [-invar.WH1/2 - invar.L3, invar.WS/2 + invar.LH +
orig];
            ary.p12 = [-invar.WH1/2 - invar.L3, invar.WS/2 + orig];
            ary.p13 = [invar.WH1/2 + invar.L3, invar.WS/2 + orig];
            ary.p14 = [invar.WH1/2 + invar.L3, invar.WS/2 + invar.LH + orig];
            ary.p15 = [invar.WH1/2 + invar.L3 + invar.WH/2 - invar.WL/2,
invar.WS/2 + invar.LH + orig];
            ary.p16 = [invar.WH1/2 + invar.L3 + invar.WH/2 - invar.WL/2,
invar.WS/2 + invar.LH + invar.LL + orig];
            ary.p17 = [invar.WH1/2 + invar.L3 + invar.WH/2 + invar.WL/2,
invar.WS/2 + invar.LH + invar.LL + orig];
            ary.p18 = [invar.WH1/2 + invar.L3 + invar.WH/2 + invar.WL/2,
invar.WS/2 + invar.LH + orig];
            ary.p19 = [invar.WH1/2 + invar.L3 + invar.WH, invar.WS/2 +
invar.LH + orig];
            ary.p20 = [invar.WH1/2 + invar.L3 + invar.WH, invar.WS/2 + orig];
            ary.p21 = [invar.WH1/2 + invar.L3 + invar.WH + invar.L2,
invar.WS/2 + orig];
            ary.p22 = [invar.WH1/2 + invar.L3 + invar.WH + invar.L2, invar.L1
+ orig];
```

```
            ary.p23 = [invar.WH1/2 + invar.L3 + invar.WH + invar.L2 +
invar.W1, invar.L1 + orig];

            ary.pE = [invar.WH1/2 + invar.L3 + invar.WH + invar.L2 +
invar.W1, ustripW/2 + orig];
            ary.T4B = [launchDim - 0.4, ustripW/2 + orig];
            ary.T5B = [launchDim - 0.25, launchW/2 + orig];
            ary.T6B = [launchDim, launchW/2 + orig];
            ary.T7B = [launchDim, -launchW/2 + orig];
            ary.T8B = [launchDim - 0.25, -launchW/2 + orig];
            ary.T9B = [launchDim - 0.4, -ustripW/2 + orig];
            ary.pH = [invar.WH1/2 + invar.L3 + invar.WH + invar.L2 +
invar.W1, -ustripW/2 + orig];

            ary.p24 = [invar.WH1/2 + invar.L3 + invar.WH + invar.L2 +
invar.W1, -invar.L1 + orig];
            ary.p25 = [invar.WH1/2 + invar.L3 + invar.WH + invar.L2, -
invar.L1 + orig];
            ary.p26 = [invar.WH1/2 + invar.L3 + invar.WH + invar.L2, -
invar.WS/2 + orig];
            ary.p27 = [invar.WH1/2, -invar.WS/2 + orig];
            ary.p28 = [invar.WH1/2, -invar.WS/2 - invar.LH1 + orig];
            ary.p29 = [invar.WL1/2, -invar.WS/2 - invar.LH1 + orig];
            ary.p30 = [invar.WL1/2, -invar.WS/2 - invar.LH1 - invar.LL1 +
orig];
            ary.p31 = [-invar.WL1/2, -invar.WS/2 - invar.LH1 - invar.LL1 +
orig];
            ary.p32 = [-invar.WL1/2, -invar.WS/2 - invar.LH1 + orig];
            ary.p33 = [-invar.WH1/2, -invar.WS/2 - invar.LH1 + orig];
            ary.p34 = [-invar.WH1/2, -invar.WS/2 + orig];
            ary.p35 = [-invar.WH1/2 - invar.L3 - invar.WH - invar.L2, -
invar.WS/2 + orig];
            ary.p36 = [-invar.WH1/2 - invar.L3 - invar.WH - invar.L2, -
invar.L1 + orig];

            % --------------- SCRIPT GENERATION -----------------------------
---------%

            % Generate eagle script

            % Set layer
            fprintf(fileID,'layer 1\r\n');

            % First command line
            fprintf(fileID,'polygon %4.3f ',w);
            % coordinates live here...
            formatSpec = ['(%4.3f %4.3f) (%4.3f %4.3f) (%4.3f %4.3f) (%4.3f
%4.3f) (%4.3f %4.3f) ' ...
                '(%4.3f %4.3f) (%4.3f %4.3f) (%4.3f %4.3f) (%4.3f %4.3f)
(%4.3f %4.3f) ' ...
                '(%4.3f %4.3f) (%4.3f %4.3f) (%4.3f %4.3f) (%4.3f %4.3f)
(%4.3f %4.3f) ' ...
                '(%4.3f %4.3f) (%4.3f %4.3f) (%4.3f %4.3f) (%4.3f %4.3f)
(%4.3f %4.3f) ' ...
                '(%4.3f %4.3f) (%4.3f %4.3f) (%4.3f %4.3f) (%4.3f %4.3f)
(%4.3f %4.3f) ' ...
```

```
                '(%4.3f %4.3f) (%4.3f %4.3f) (%4.3f %4.3f) (%4.3f %4.3f)
(%4.3f %4.3f) ' ...
                '(%4.3f %4.3f) (%4.3f %4.3f) (%4.3f %4.3f) (%4.3f %4.3f)
(%4.3f %4.3f) ' ...
                '(%4.3f %4.3f) (%4.3f %4.3f) (%4.3f %4.3f) (%4.3f %4.3f)
(%4.3f %4.3f) ' ...
                '(%4.3f %4.3f) (%4.3f %4.3f) (%4.3f %4.3f) (%4.3f %4.3f)
(%4.3f %4.3f) ' ...
                '(%4.3f %4.3f) (%4.3f %4.3f) (%4.3f %4.3f) (%4.3f %4.3f)
(%4.3f %4.3f) ' ...
                '(%4.3f %4.3f) (%4.3f %4.3f) (%4.3f %4.3f)\r\n'];
            fprintf(fileID,formatSpec,ary.p1, ...
            ary.pA, ary.T4A, ary.T5A, ary.T6A, ary.T7A, ary.T8A, ary.T9A,
ary.pD, ...
            ary.p2,ary.p3,ary.p4,ary.p5,ary.p6,ary.p7,ary.p8,ary.p9,ary.p10,
...

ary.p11,ary.p12,ary.p13,ary.p14,ary.p15,ary.p16,ary.p17,ary.p18,ary.p19,ary.p
20, ...
            ary.p21,ary.p22,ary.p23,...
            ary.pE, ary.T4B, ary.T5B, ary.T6B, ary.T7B, ary.T8B, ary.T9B,
ary.pH, ...
            ary.p24,ary.p25,ary.p26,ary.p27,ary.p28,ary.p29,ary.p30, ...
            ary.p31,ary.p32,ary.p33,ary.p34,ary.p35,ary.p36,ary.p1);
        end
    end
    % All filters process these
    %
=============================================================================
======
    % Draw dimensions
    fprintf(fileID,'layer 20\r\n');
    fprintf(fileID,'wire %4.3f (%4.3f %4.3f) (%4.3f %4.3f)\r\n',wdim,-
dimX/2,dimY/2+orig,dimX/2,dimY/2+orig);
    fprintf(fileID,'wire %4.3f (%4.3f %4.3f) (%4.3f %4.3f)\r\n',wdim,-
dimX/2,-dimY/2+orig,dimX/2,-dimY/2+orig);
    fprintf(fileID,'wire %4.3f (%4.3f %4.3f) (%4.3f %4.3f)\r\n',wdim,dimX/2,-
dimY/2+orig,dimX/2,dimY/2+orig);
    fprintf(fileID,'wire %4.3f (%4.3f %4.3f) (%4.3f %4.3f)\r\n',wdim,-
dimX/2,-dimY/2+orig,-dimX/2,dimY/2+orig);
    fprintf(fileID,'layer 1\r\n');

    % CPW launch sides if exist ==============================
    if strcmp(inData.ustrip(i), 'n')
        cpwSideswOrig = cpwSides;
        for m = 1:6
            for n = 1:4
                cpwSideswOrig(m,:,n) = cpwSideswOrig(m,:,n) + [0 orig];
            end
        end
        for qq = 1:4
            fprintf(fileID,'polygon gnd %4.3f ',w);
            formatSpec = '(%4.3f %4.3f) (%4.3f %4.3f) (%4.3f %4.3f) (%4.3f
%4.3f) (%4.3f %4.3f) (%4.3f %4.3f) (%4.3f %4.3f)\r\n';
            %Draw side polygons
```

```
fprintf(fileID,formatSpec,cpwSideswOrig(1,:,qq),cpwSideswOrig(2,:,qq),cpwSide
swOrig(3,:,qq),...

cpwSideswOrig(4,:,qq),cpwSideswOrig(5,:,qq),cpwSideswOrig(6,:,qq),cpwSideswOr
ig(1,:,qq));
            %VIA
            fprintf(fileID,'via ''gnd'' %4.3f round (%4.3f %4.3f)\r\n', viaw,
cpwViaLoc(:,qq) + [0; orig]);
            %Draw antipad
            fprintf(fileID,'change width 0.41\r\n');
            formatSpec = 'circle (%4.3f %4.3f) (%4.3f %4.3f)\r\n';
            fprintf(fileID,formatSpec,cpwViaLoc(:,qq) + [0; orig],
cpwViaLoc(:,qq) + [0; orig] + [0; 0.08]);
        end
    end
    %===========================================================
    % Label each filter
    this_label = char(inData.text(i));
    startLabelLoc = [(-1.5), (orig + dimY/2 - 1)];
    thisChar = startLabelLoc;
    for qq = 0:3
        if(this_label(qq+1) == 'A')
            thisLabelVert = labA;
        else
            thisLabelVert = labB;
        end
        % Locate vertices individually . base vertices + location + sweep
        thisLabelVert = thisLabelVert + [startLabelLoc(1)*ones(4,1),
startLabelLoc(2)*ones(4,1)] + [1*qq*ones(4,1), zeros(4,1)];
        fprintf(fileID,'polygon label %4.3f ',w);
        formatSpec = '(%4.3f %4.3f) (%4.3f %4.3f) (%4.3f %4.3f) (%4.3f %4.3f)
(%4.3f %4.3f)\r\n';
        %Draw each label

fprintf(fileID,formatSpec,thisLabelVert(1,:),thisLabelVert(2,:),thisLabelVert
(3,:),thisLabelVert(4,:),thisLabelVert(1,:));
    end
end
```

Appendix B: Biasing/Sequencing Eagle Schematic and Layout

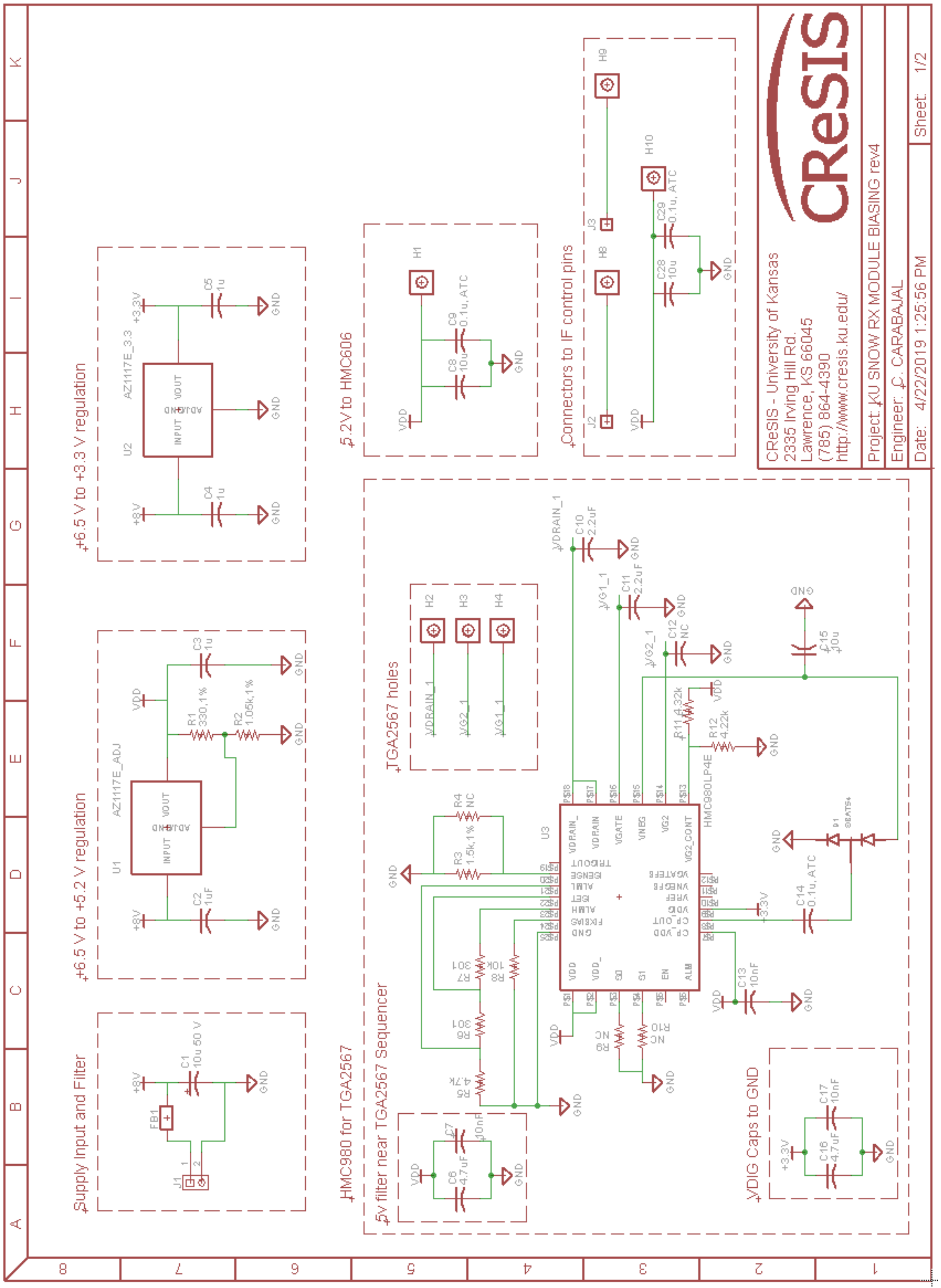

Figure 95: Compact Rx Biasing Schematic (Mod 1) page 1

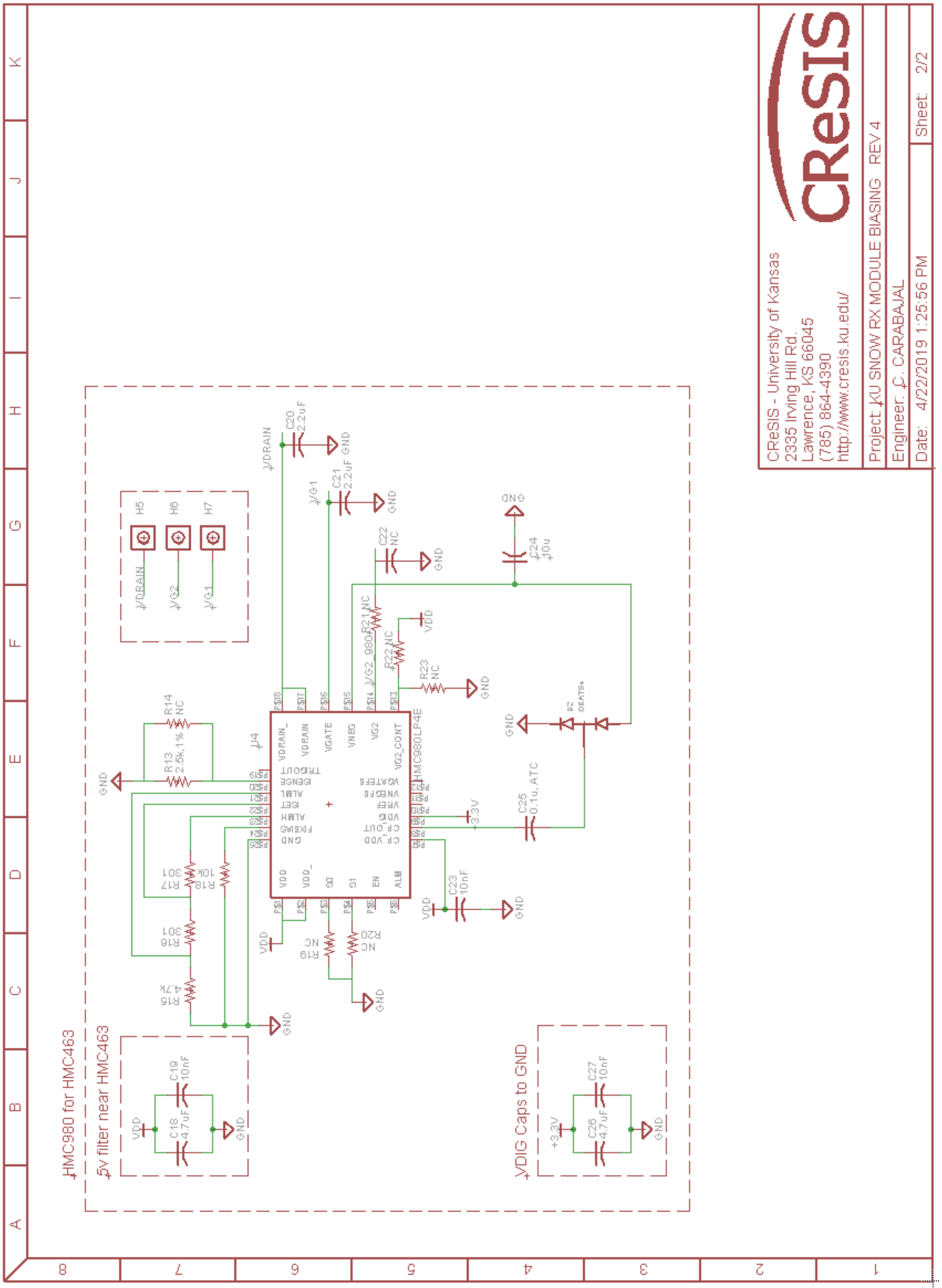

Figure 96: Compact Rx Biasing Schematic (Mod 1) page 2

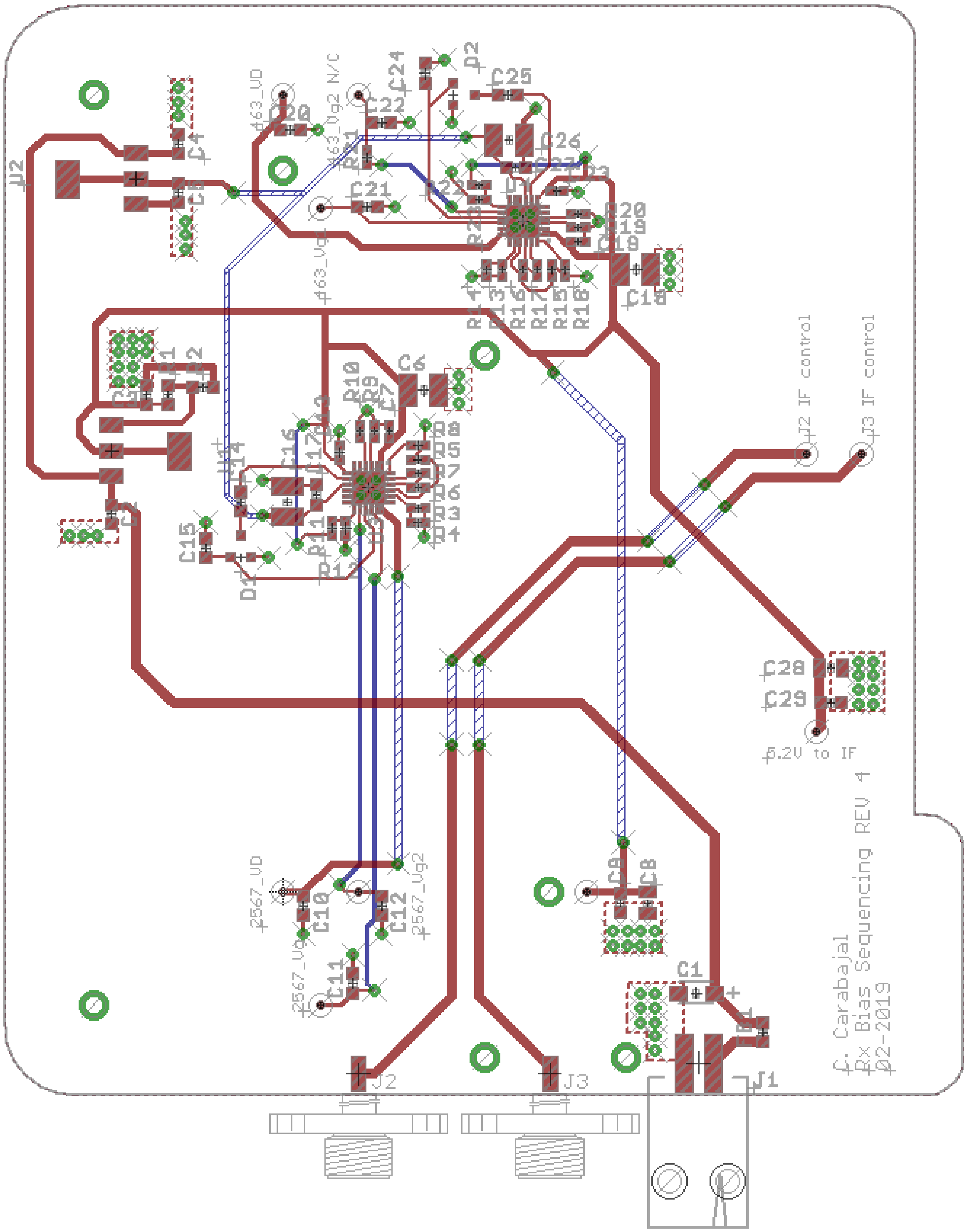

Figure 97: Compact Rx Biasing (Mod 1) Layout

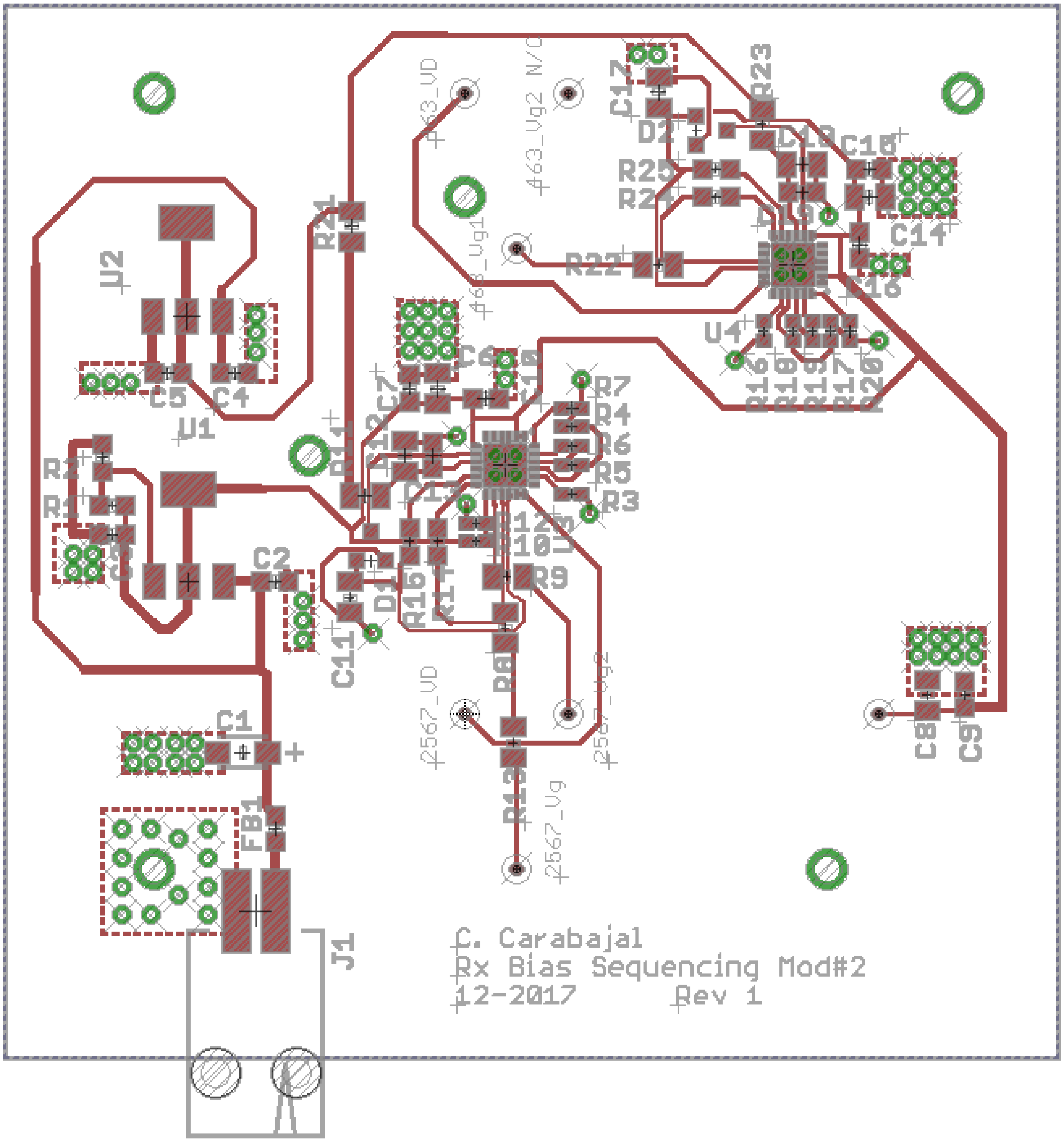

Figure 98: Compact Rx Biasing (Mod 2) Layout (shares schematic with Mod 1)

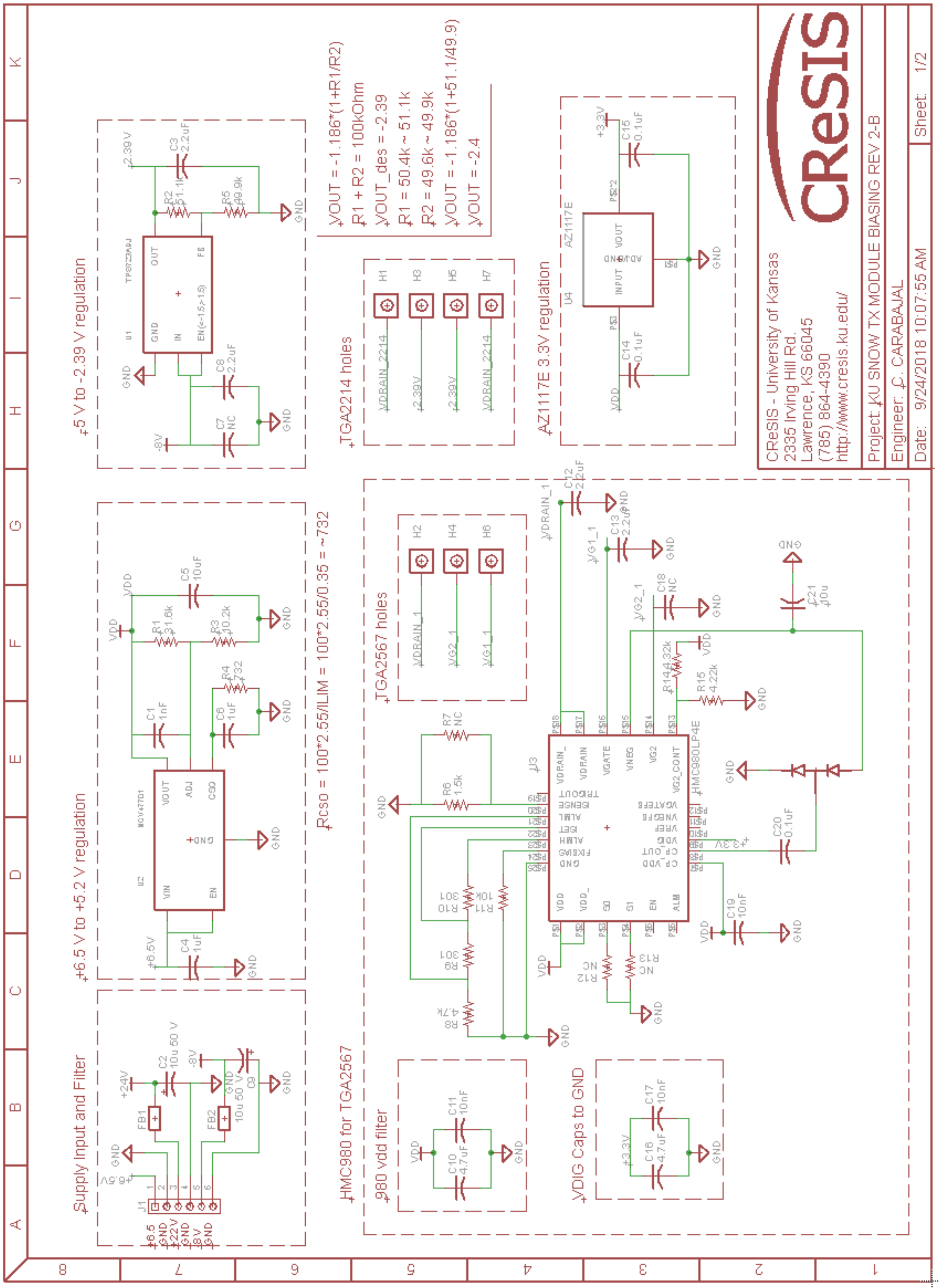

Figure 99: Compact Tx Biasing Schematic page 1

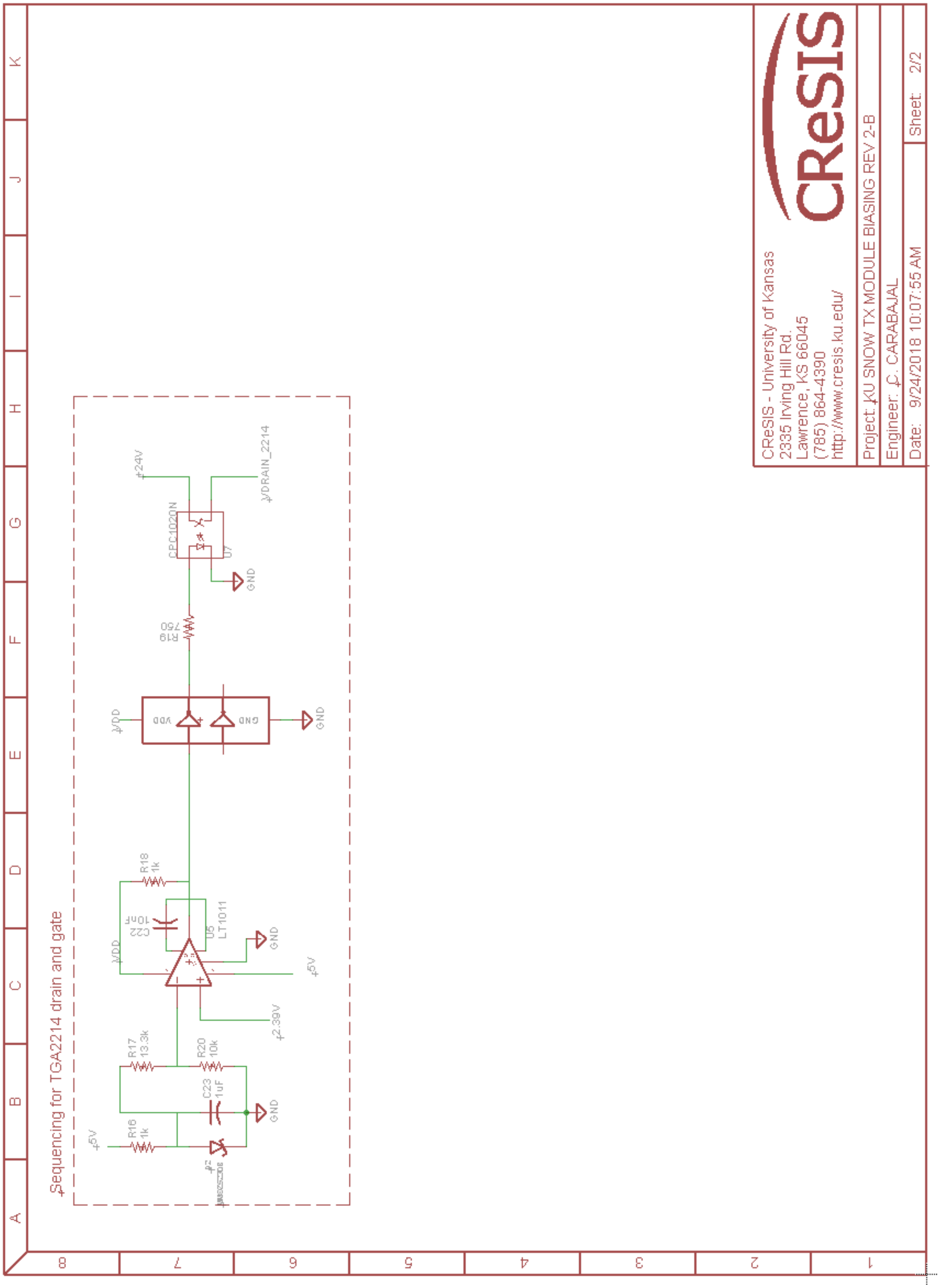

Figure 100: Compact Tx Biasing Schematic page 2

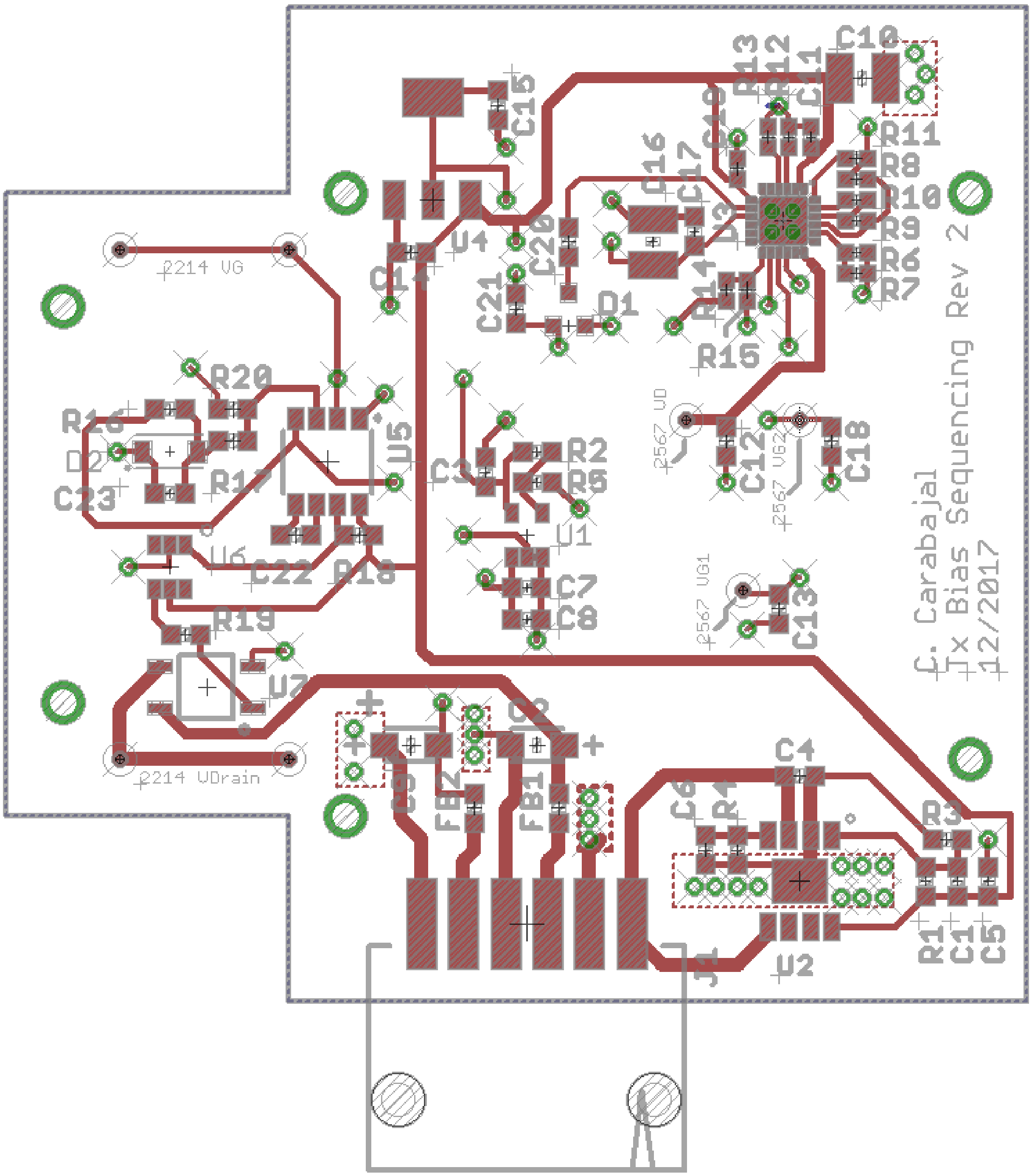

Figure 101: Compact Tx Biasing Layout